

Development of functionally graded tungsten/EUROFER coating systems

zur Erlangung des akademischen Grades eines
Doktors der Ingenieurwissenschaften

von der Fakultät für Maschinenbau
des Karlsruher Instituts für Technologie (KIT)

genehmigte

Dissertation

von

Dandan Qu

aus Heilongjiang, China

Tag der mündlichen Prüfung: 27.10.2016

Hauptreferent: Priv.-Doz. Dr. Jarir Aktaa

Korreferent: Prof. Dr. Anton Möslang



This document is licensed under the Creative Commons Attribution – Share Alike 3.0 DE License (CC BY-SA 3.0 DE): <http://creativecommons.org/licenses/by-sa/3.0/de/>

Abstract

Reduced activation Ferritic/Martensitic (RAFM) steels, e.g. EUROFER are to be used as structural material for the First Wall (FW) of future fusion power plants. The interaction between plasma and FW, especially physical sputtering will limit the FW lifetime under normal operation. Therefore, tungsten (W) coating is selected to protect the FW due to its very low sputtering yield and low activation. However, the mismatch in thermo-physical properties between W and EUROFER can lead to large residual thermal stresses and even failure. To overcome the issue of erosion a protective W coating with a functionally graded (FG) W/EUROFER layer (FG W/EUROFER coating system) on EUROFER substrate is developed and optimized.

Non-linear finite element simulations have been performed to predict optimal parameters of the coating system. Thereby the potential of the FG-layer in reducing residual stress and inelastic strains as well as improving lifetime has been demonstrated, and the investigated thickness of FG-layer has been suggested.

Based on the simulation results five samples have been fabricated by vacuum plasma spraying (VPS) with three different thicknesses and two stepwise linear gradients of FG-layer. The microstructural observations show that the coating system has fine linear gradient and variable thickness as designed, low porosity ($< 4\%$), as well as a sound interface with high interface toughness. Three- and four-point bending tests have been performed to evaluate the interface toughness. The high ductility and vast plastic deformations during bending tests have been observed in FG-layer and at the interface between substrate and FG-layer. The measured mean interface toughness are 225 and 258 J/m^2 for sample 5-T(7) and 3-T(7), respectively. Macro and microhardness of each coating and substrate have been investigated, and global homogeneity and fine gradient of the whole sample have been observed. In addition, comparing to the as-received substrate grain growth and reduction of the substrate hardness at the interface have been observed and assumed to be owing to the high heat from the spraying process, which needs to be optimized in the future.

For FW application, the thermal-mechanical properties of the FG W/EUROFER coating system have been assessed and analyzed including ELMs-like thermal shock and thermal fatigue test. The thermal shock crack threshold at RT and $550 \text{ }^\circ\text{C}$ is between 0.19 and 0.38 GW/m^2 , which is comparable with bulk pure W at the same test condition. Considering the thermal fatigue, no macro or micro-crack are observed in the coating system after 500 thermal cycles test.

Kurzfassung

Reduziert aktivierte ferritisch-martensitische (RAFM) Stähle, wie z.B. EUROFER sind unter anderem für die erste Wand (FW) der zukünftigen Fusionskraftwerke als Strukturmaterial vorgesehen. Die Wechselwirkung zwischen dem Plasma und der FW, im speziellen das physikalische Sputtern, wird die Lebensdauer der ersten Wand bei Normalbetrieb begrenzen. Daher wird wegen seiner sehr geringen Sputterneigung und der niedrigen Aktivierung eine Beschichtung aus Wolfram (W) gewählt, um die FW zu schützen. Jedoch führen die unterschiedlichen thermo-physikalischen Eigenschaften zwischen W und EUROFER zu großen thermischen Spannungen oder gar zum Versagen. Um dem Problem von Erosion entgegenzuwirken wird eine schützende Wolframbeschichtung mit Hilfe einer gradierten Schicht (FG) aus W/EUROFER (FG W/EUROFER Beschichtungssystem) auf einem EUROFER Substrat entwickelt und optimiert.

Es wurden nichtlineare Finite-Elemente-Simulationen durchgeführt, um die optimalen Parameter des Beschichtungssystems vorhersagen zu können. In diesem Zusammenhang konnten die positiven Eigenschaften der gradierten Schicht wie die Reduktion von Eigenspannungen und die verbesserte Lebensdauer gezeigt werden. Außerdem wurde eine optimale Dicke der gradierten Schicht vorgeschlagen.

Basierend auf den Ergebnissen der Simulationen sind fünf Proben durch Vakuumplasmaspritzen (VPS) mit drei unterschiedlichen Dicken und zwei schrittweisen linearen Gradierungen der Schicht hergestellt worden. Die mikrostrukturellen Beobachtungen haben gezeigt, dass die Beschichtungssysteme, wie gewünscht, eine feine lineare Gradierung, unterschiedliche Schichtdicken, geringe Porosität (<4%) sowie eine gute Zwischenschicht mit hoher Zähigkeit aufweisen. Drei und Vier-Punkt-Biegeversuche wurden durchgeführt, um die Zähigkeit der Zwischenschicht zu bewerten. Die hohe Duktilität und die großen plastischen Verformungen konnten während der Biegeversuche in der gradierten Schicht und an der Grenzfläche zwischen Substrat und der gradierten Schicht beobachtet werden. Die gemessene mittlere Zwischenschicht-Zähigkeit beträgt 225 und 258 J/m² für Probe 5-T (7) und 3-T (7). Makro- und Mikrohärtemessungen sind von jeder Beschichtung und dem entsprechendem Substrat durchgeführt worden und es konnten eine homogene Verteilung und eine feine Abstufung über der gesamten Probe beobachtet werden. Darüber hinaus konnte im Vergleich mit dem Substrat im Anlieferungszustand ein Kornwachstum und eine reduzierte Härte in der Zwischenschicht beobachtet werden. Dies ist der hohen Wärme aus dem Sprühvorgang zuzuschreiben und muss in Zukunft optimiert werden.

Für die Erste-Wand Anwendung wurden die thermisch-mechanischen Eigenschaften des W /EUROFER Beschichtungssystems bewertet und analysiert - einschließlich so ge-

nanter Edge Localized Modes (ELMs) artigen Thermoschock und thermischen Ermüdungstest. Der Grenzwert für Thermoschock Risse bei RT und 550 °C liegt zwischen 0,19 und 0,38 GW / m² und ist vergleichbar mit reinem W bei gleichen Testbedingungen. In Bezug auf die thermischen Ermüdungsversuche konnten keine Makro- oder Mikrorisse in dem Beschichtungssystem, auch nicht nach 500 Zyklen, beobachtet werden.

Statement of original work

I hereby declare that I have produced this work independently and this dissertation represents my original work, except where I have cited the specified sources and literatures. I have identified the verbatim and content as acquired and complied with the statute of the KIT to ensure good scientific work.

Signature

Date:

Contents

Abstract	i
Kurzfassung	iii
Statement of original work	v
Contents	vii
List of figures	ix
List of tables	xiii
List of abbreviations	xv
List of symbols	xvii
1 Introduction	1
1.1. Background	1
1.2. Objective	4
2 State of the Research	7
2.1. First wall materials and tungsten coating	7
2.1.1 Reduced activation ferritic/martensite steel	7
2.1.2 Tungsten coating	9
2.1.3 Functionally Graded Material (FGM)	13
2.1.4 Fabrication method comparison of FGM	15
2.2. Vacuum plasma spraying	17
2.2.1 The principle of vacuum plasma spraying	17
2.2.2 Characteristics and representation of VPS coating	19
2.2.3 VPS tungsten coatings on RAFM steel substrates	21
3 Approach and Methods	23
3.1. Approach	23
3.1.1 Determination of FG-layer thickness by Finite element simulations	23
3.1.2 Fabrication of the coating system	25
3.1.3 Qualification of the FG W/EUROFER coating system	30
3.2. Microstructural analysis	30
3.2.1 Optical microscope	30
3.2.2 Scanning electron microscopy	31
3.2.3 Auger electron spectroscopy	31
3.2.4 Electron backscatter diffraction	32
3.3. Mechanical investigation	33
3.3.1 Hardness.....	33
3.3.2 Thermal load tests	37

3.3.3	Interface toughness.....	39
4	Results and discussion.....	47
4.1.	FE simulation	47
4.1.1	Simulation of the cooling down phase	47
4.1.2	Simulation of the operation phase	48
4.1.3	Creep lifetime evaluation of EUROFER.....	49
4.1.4	Discussion and conclusion	52
4.2.	VPS samples.....	53
4.2.1	Investigation on as-received surfaces.....	54
4.2.2	Comparison of the samples	56
4.2.3	Discussion and conclusion	59
4.3.	Microstructure	60
4.3.1	Pure W coating.....	60
4.3.2	FG W/EUROFER coating with three layers	65
4.3.3	FG W/EUROFER coating with five layers	69
4.3.4	Interface between the coating system and substrate.....	70
4.3.5	Discussion and conclusion	71
4.4.	Mechanical Analysis	73
4.4.1	Nanohardness and Young’s modulus	73
4.4.2	Microhardness	75
4.4.3	Interface toughness.....	79
4.4.4	Thermal load resistance analysis	89
4.4.5	Discussion and conclusion	97
5	Summary and outlook.....	101
5.1.	Summary	101
5.2.	Outlook.....	102
6	Reference.....	103
	Appendix.....	111
	Acknowledgments.....	114
	List of publications.....	116
	Curriculum Vitae	117

List of figures

Figure 1.1: World energy demand and supply in the future [1].	1
Figure 1.2: Conceptual view of fusion DEMO reactor [6].	2
Figure 1.3: Schematic view of the first wall loading by plasma particles, electromagnetic radiation and neutrons, and induced radiation-damage effects [8].	3
Figure 2.1: Thermal shock induced surface modifications in different tungsten grades after 100 pulse and 1ms duration [42].	12
Figure 2.2: (a) CVD tungsten coating exposed to ELMs-like thermal shock at power densities of 0.16–1.0 GW/m ² for 1 ms, 100 pulse [45]; (b) Cross section after heat loading of experimental condition 40 MW/m ² , 7 s, 30 cycles [19].	13
Figure 2.3: (a) Dependence of the maximum equivalent inelastic strain after 100 cycles on layer thickness for various gradient functions [52]; (b) Variation of stored elastic strain energy with graded layer number [20].	15
Figure 2.4: Classification of thermal spray technologies [70].	17
Figure 2.5: Schematic of the plasma spraying process.	18
Figure 2.6: Different spray parameters [70].	19
Figure 2.7: Definition of the splat (YSZ) mean diameter: (a) Disk-shaped splat and (b) splash-shaped splat [70].	21
Figure 3.1: The sketch and mesh of the FE model.	24
Figure 3.2: The schematic of measurement direction on original EUROFER substrate plate.	26
Figure 3.3: The particle size distribution of tungsten powder.	27
Figure 3.4: The particle size distribution of EUROFER powder.	27
Figure 3.5: The sketch of plasma gun movement.	28
Figure 3.6: The photograph of a profilometer.	29
Figure 3.7: Forming stages of the Auger electron [82].	32
Figure 3.8: Schematic diagram of a typical EBSD installation [84].	33
Figure 3.9: A cross section of an indentation (a) and load-displacement curve (b) [86].	35
Figure 3.10: Left: the schematic view of the electron beam facility JUDITH 1 with diagnostic systems. A thermal shock sample is mounted on a XYZ-table and scanned by the electron beam. Right: photograph of JUDITH 1 located in the hot cells [88].	37
Figure 3.11: Thermal fatigue test. Left: vacuum furnace facility; Right; temperature curve over time.	39
Figure 3.12: Set-ups: (a) three-point bending and (b) four-point bending.	41
Figure 3.13: Schematic view of load and moment for three-point (a) and four-point (b) bending.	41
Figure 3.14: (a) Three-point and (b) four-point bending specimen.	42
Figure 3.15: Schematic view of the beam for three- and four-point bending test.	43
Figure 3.16: The steady-state energy release rate as a function of the thickness ratio and material parameter λ calculated for FG W/EUROFER coating system according to [93].	46
Figure 4.1: (a) von Mises stress distribution and (b) distribution of principal stress σ_{11} of the FE-model with 0.5 mm thick FG-layer.	47

Figure 4.2: Maximum von Mises stress and maximum equivalent plastic strain versus thickness of FG-layer.	48
Figure 4.3: (a) The dependence of max. equivalent creep strain after 365 cycles on thickness of FG-layer, and (b) Max. equivalent creep strain versus the number of cycles for all investigated thicknesses.	49
Figure 4.4: Creep damage per cycle versus number of cycles for all investigated thicknesses of FG-layer.	51
Figure 4.5: Allowable number of cycles for EUROFER versus the FG-layer thickness.	51
Figure 4.6: Sample 3-T(7) with a ruler.	53
Figure 4.7: Schematic of sample layout and geometry.	54
Figure 4.8: 2D and 3D topography of sample 5-T(7) from the top view (convex downward).	55
Figure 4.9: AES-Analysis of element concentration on the as-received surface of sample 3-T(5).	55
Figure 4.10: Roughness of as-received samples.	56
Figure 4.11: Distribution of tungsten and iron in cross-section of samples with 3 and 5 layers as FG-layer.	57
Figure 4.12: Gradient of FG-layer.	57
Figure 4.13: Nominal and true thickness of FG-layer.	58
Figure 4.14: Nominal and true thickness of the coating system (thickness of tungsten + FG-layer).	58
Figure 4.15: The characteristics of as-received pure tungsten coating surfaces: (a-d) unpolished surfaces; (e, f) polished surfaces.	61
Figure 4.16: Diameter of the pancake-like structure.	62
Figure 4.17: Cross-section microstructure of pure tungsten coating.	62
Figure 4.18: The grain characteristics of pure tungsten coating: (a) SEM image; (b) pattern quality; (c) grain orientation map and (d) grain distribution map.	63
Figure 4.19: Grain size of pure tungsten coating.	64
Figure 4.20: (a, b): an example of porosity calculation (pure tungsten coating of sample 3-T(7)); (c): the porosity versus the nominal concentration of W of sample 3-T(5); (d): comparison on porosity of the five samples' tungsten coating.	65
Figure 4.21: (a) The cross-section microstructure of sample 3-T(7) and its FG-layer with the nominal concentration of W: (b) 75; (c) 50 and (d) 25 in Vol.-%.	66
Figure 4.22: (a) Magnification of FG-layer (W50% layer) and columnar tungsten grains in FG-layer with (b) W50%, (c) W25%, and (d) W75% of sample 3-T(7).	67
Figure 4.23: EBSD shows grain characteristics of W75%-W100%: (a) SEM image; (b) pattern quality; (c) phase map; (d) grain orientation map and (e) grain distribution map.	68
Figure 4.24: (a) The cross-section microstructure of sample 5-T(7) and its FG-layer with the nominal concentration of W: (b) 75; (c) 63; (d) 50; (e) 37 and (f) 25 in Vol.-%.	69
Figure 4.25: Substrate interface morphology of sample 3-T(7).	70
Figure 4.26: Nanohardness versus the nominal concentration of W.	74
Figure 4.27: Young's modulus versus the nominal concentration of W.	75
Figure 4.28: Vickers hardness versus the nominal concentration of W of sample 3-T(7).	76
Figure 4.29: Micrographs of microhardness's indentations (a) pure W from the top view; (b) FG-layer (W75% layer) from the cross-section view.	76
Figure 4.30: Microhardness at different positions of sample 3-T(7).	77
Figure 4.31: Microhardness versus the distance from the interface of sample: (a) 3-T(5); (b) 5-T(7); (c) 3-T(3) and (d) 5-T(5).	78

Figure 4.32: Optical microstructure of the sample 3-T(7)' substrate after etching: (a, c) distance from the interface ≥ 4 mm; (b, d) near the interface.	79
Figure 4.33: Load vs. deflection curve of pre-cracked specimens during three-point (a) and four-point (b) bending tests.	80
Figure 4.34: Optical microstructure of pre-cracked specimens after three-point bending.	81
Figure 4.35: The crack propagation within FG-layer (a, c) and along the substrate interface (b) of sample 5-T(7) after three-point bending.	82
Figure 4.36: Fracture microstructure within the FG-layer with the nominal concentration of W(Vol.-%): (a) 25%; (b) 50%; (c) 75%.	83
Figure 4.37: Fracture microstructure at the interface: (a) and (b) coating-side; (c) and (d) substrate-side interface.	84
Figure 4.38: Comparison on interface toughness of two coating systems.	87
Figure 4.39: Comparison on interface toughness among FG W/EUROFER coating system and the others systems.	88
Figure 4.40: The surface exposed to the power density of 0.19 GW/m ² at RT and 550 °C [113].	89
Figure 4.41: The surface damages exposed to the power density of 0.38 GW/m ² at RT: (a, b) crack network of sample 3-T(3); (c-f) magnification of cracks of sample 3-T(3), 3-T(5), 3-T(7) and 5-T(7) , respectively [113].	90
Figure 4.42: The surface damages exposed to the power density of 0.38 GW/m ² at 550°C: (a) crack network of sample 3-T(3); (b) melted edges of sample 5-T(5); (c, d) grew grains of 3-T(5) and sample 5-T(5), respectively; (e, f) cracks under the surface of sample 3-T(5) [113].	91
Figure 4.43: Crack density exposed to the power density of 0.38 GW/m ² at the base temperature of RT and 550 °C, respectively.	92
Figure 4.44: Roughness comparison before and after exposing to the power density of 0.19 and 0.38 GW/m ² at the base temperature of RT and 550°C.	93
Figure 4.45: Thermal shock response of the coating system after 100 thermal shock events at different power densities and base temperatures.	93
Figure 4.46: Microstructures of sample 3-T(3) after: (a) 100 cycles; (b) 200 cycles; (c) 300 cycles; (d) 400 cycles; (e) 500 cycles.	95
Figure 4.47: Comparison on microhardnesses of the samples after thermal fatigue tests with the as-received sample.	96
Figure 4.48: Small cracks around indentations on samples after (a) 400; (b) 500 thermal cycles.	96

List of tables

Table 1.1 Operation conditions for the plasma facing components of ITER and a DEMO-like reactor [9]	4
Table 2.1 Specified chemical compositions of EUROFER and F82H steel	8
Table 2.2 Comparison of the fabrication methods, -/+ stands for un-/appropriate and • for unknown	16
Table 3.1: The basic properties of materials	25
Table 3.2: The creep properties of EUROFER	25
Table 3.3: Roughness of original EUROFER substrate	26
Table 3.4: Chemical composition of tungsten and EUROFER powder used in this work	28
Table 3.5: Parameters of grinding and polishing for W/EUROFER coating system	31
Table 4.1: The nominal variations of five coating systems	53
Table 4.2 (a): Interface toughness of sample 3-T(7) calculated based on three-point bending tests	85
Table 4.3: Interface toughness of sample 3-T(7) calculated based on four-point bending tests	86

List of abbreviations

AES	Auger electron spectroscopy
APS	Air Plasma Spraying
BSE	Backscatter Electron
CCD	Charge-Coupled Devices
CFC	Carbon-Fiber Composite
CSM	Continuous Stiffness Mode
CTE	Coefficient of Thermal Expansion
CTOD	Crack-Tip-Opening Displacement
CVD	Chemical Vapor Deposition
CZ	Contact-Zone
dpa	displacements per atom
DBTT	Ductile-Brittle Transition Temperature
DEMO	Demonstration Fusion Reactor
EAST	Experimental Advanced Superconducting Tokamak
EBSD	Electron Backscattered Diffraction
EDM	Electrical Discharge Machining
EDX	Energy Dispersive X-ray Analysis
FEA	Finite Element Analysis
FGM	Functionally Graded Material
FIB	Focused Ion Beam
ELM	Edge Localized Mode
FW	First Wall
FZJ	Forschungszentrum Jülich
HCPB-TBM	Helium Cooled Pebble Bed-Test Blanket Module
HIP	Hot Isostatic Pressing
IEA	International Energy Agency
ITER	International Thermonuclear Experimental Reactor
IPF	Inverse Pole Figure
JET	Joint European Torus

JT-60	Japan Torus 60
JUDITH 1	Jülich Divertor Test Facility1 in Hot Cells
JUDITH 2	Jülich Divertor Test Facility2 in Hot Cells
KIT	Karlsruhe of institute of technology
KLST	Kleinst
LPPS	Low Pressure Plasma Spraying
MS	Magnetron Sputtering
OM	Optical Microscopy
ODS	Oxide-Dispersion-Strengthened
PFM	Lasma-facing Material
PFC	Plasma Facing Components
QSPA	Quasi-Stationary Plasma Accelerator
RSUHP	Resistance Sintering under Ultra-High Pressure
RAF/M	Reduced Activation Ferritic/Martensitic Steel
SEM	Scanning Electron Microscopy
SSHLs	Steady-State Heat Loads
T15	Tokamak 15
TFTR	Tokamak Fusion Test Reactor
VPS	Vacuum Plasma Spraying
W-UHP	Ultra-High Purity Tungsten
WTa1, WTa5	Tungsten with 1, 5 wt% Tantalum
WVMW	Potassium Doped Grade

List of symbols

$\dot{\epsilon}_{Cr}$	Creep strain rate
f	Gradient factor
C	Norton creep parameter
n	Norton creep parameter
R_a	Arithmetic mean deviation of the roughness
R_q	Root mean square deviation of the roughness
$R_z(\text{DIN})$	Average maximum height of the roughness
E	Young's modulus
ν	Poisson's ratio
h	Thickness of specimen
h_{max}	Maximum depth of the indenter penetrated in sample
h_s	Sink-in depth of sample during nanoindentation
g	Gravitational acceleration
B	Width of specimen
Σ_{sub}	Stiffness of substrate
Σ_c	Stiffness of the composite specimen
I_c	Moment of inertia for the composite specimen
λ	Composite material parameter
C_b	Compliance of beam
P_c	Load for the propagation of the interfacial crack
G_c	Critical energy release rate
G_{ss}	Steady-state energy release rate
S_r	Minimum stress yields to rupture
θ	Temperature
T_d	Design time
S_d	Allowable stress
σ_e	Equivalent stress
$\sigma_{1,2,3}$	Principal stresses

D_{Cr}	Creep damage
N_{Cr}	Allowable number of cycles

1 Introduction

1.1. Background

The energy shortage is a global problem, and the energy demand in the future will increase as shown in Figure 1.1. Figure 1.1 also predicts possible future scenarios of energy supply, and the main energy supply is currently fossil fuel. However, traditional fossil fuel is the major source of the greenhouse gas emission. In addition, the nature of renewable energy is finite and the security of nuclear fission is still one of the international challenges. Hence, choosing the proper future energy sources and strategies is a significant task.

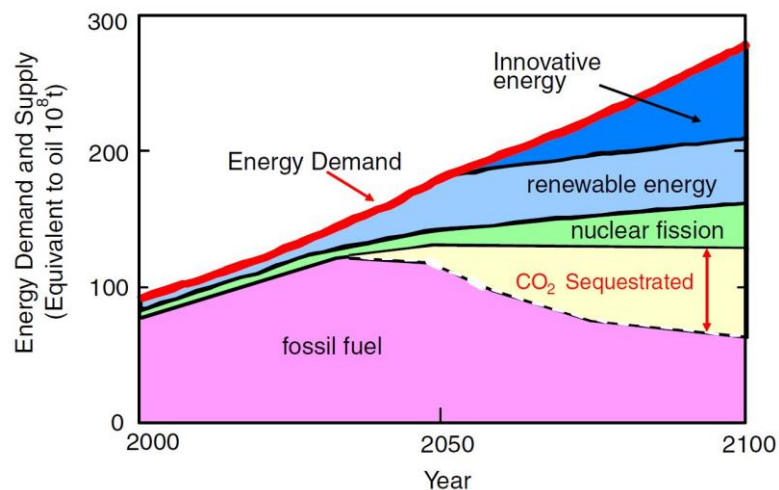


Figure 1.1: World energy demand and supply in the future [1].

Nuclear fusion is a potentially clean and sustainable energy, in which two light atomic nuclei collide to form a new heavy nucleus, and internal energy from nuclei is released during this process. Specifically, a fusion reaction yields about four million times more energy than a chemical reaction such as the burning of coal, oil or gas. While a 1,000 MW coal-fired power plant requires 2.7 million tons of coal per year, a fusion power plant of the kind envisioned for the second half of this century will only require 250 kilos of fuel per year, half of it deuterium, half of it tritium. In addition, fusion emits no pollution or greenhouse gasses. Its major by-product is helium: an inert, non-toxic gas [2]. Among many possible fusion reactions, the reactions between hydrogen isotopes deuterium and tritium (see formula (1.1)) are favored due to its high efficiency and the good feasibility of the plasma temperature of 100 million degrees Kelvin. Approx. 30 million kWh of electrical powers can be obtained from the reaction of 1 kg D-T.



Since the early 1950s, controlled fusion has been carried out internationally. Several tokamak devices based on magnetic confinement concepts are developed one after another, from joint European torus (JET) in Europe, Tokamak Fusion Test Reactor (TFTR) in US, Japan Torus 60 (JT-60, later modified into JT60-U), T15 (Tokamak 15) in the USSR [3] to Experimental Advanced Superconducting Tokamak (EAST) in China [4]. The main progress in fusion research so far has been directly connected to physics-oriented experimental facilities built-in many countries with varying missions and scopes. No country has yet offered a firm commitment to build the next machine after the International Thermonuclear Experimental Reactor (ITER, aiming at demonstrating the scientific and technological feasibility). The future demonstration fusion reactor (DEMO) is viewed as the last step necessary to reduce the technical and programmatic risk associated with the first commercial fusion power plant [5]. The conceptual view of fusion DEMO reactor is shown in Figure 1.2. First wall (FW) is the plasma facing component (PFC) of the blanket in which fusion power converts to energy and tritium is provided from lithium.

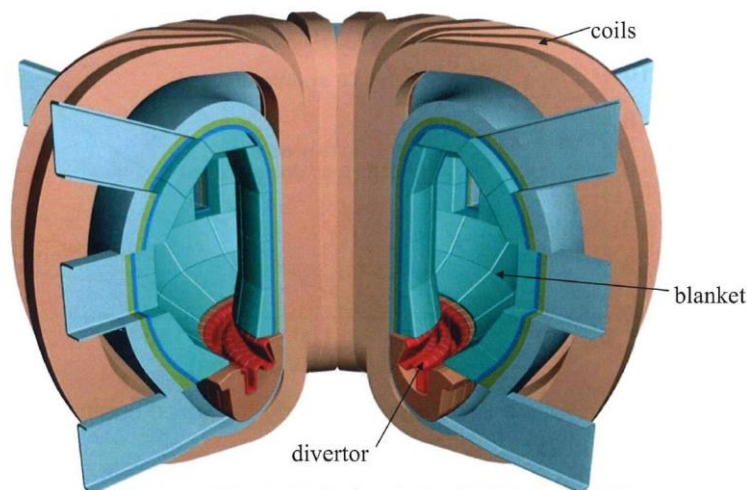


Figure 1.2: Conceptual view of fusion DEMO reactor [6].

Materials for the FW, limiters, divertor and breeding-blanket components are the most severely exposed parts of future fusion reactors and pose key problems for the successful implementation of fusion reactors as an efficient source of electric power. Demanding requirements are imposed on materials used in such environments, including low activation, adequate strength and toughness, and high swelling and creep resistance. Several low activations materials including ferritic/martensitic steels, Vanadium alloys and SiC/SiC composite materials can fulfill the severe requirements. Among them, ferritic/martensitic steels are considered to the most advanced and mature materials for FW application [7]. The operational conditions of structural materials are essentially dependent on the interaction with the high energy 14 MeV neutrons, low energy plasma particles and electromagnetic radiation. As shown in Figure 1.3, the interaction between impinging particles or electromagnetic radiation with the first wall could lead to a series

irradiation effects, especially physical and chemical sputtering will limit the FW lifetime under normal operation.

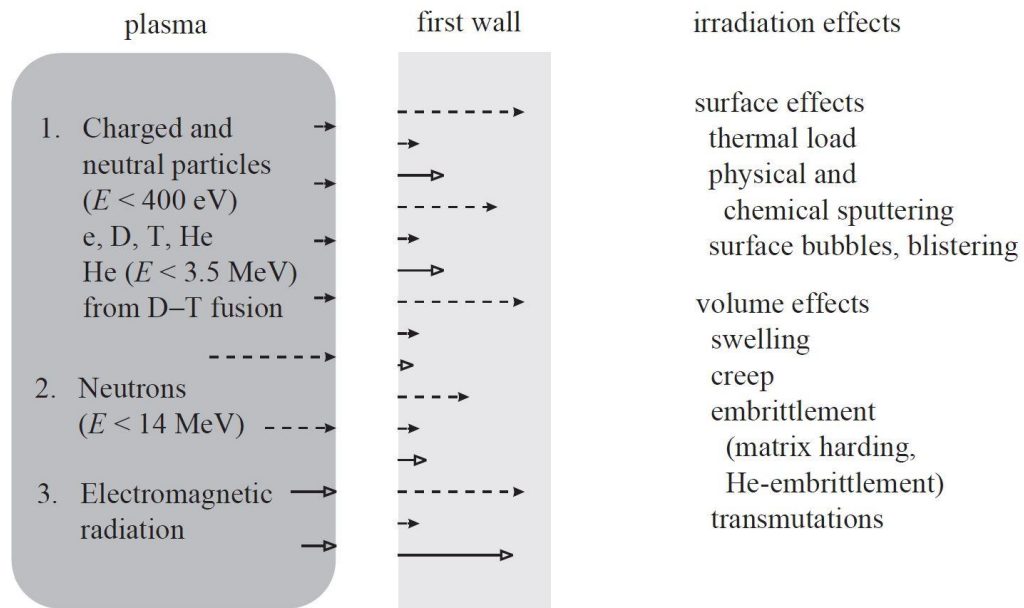


Figure 1.3: Schematic view of the first wall loading by plasma particles, electromagnetic radiation and neutrons, and induced radiation-damage effects [8].

Except the impinging particles, the surface of plasma-facing material (PFM) is also subjected to a heat flux from the plasma. Table 1.1 list the main operation conditions for the PFC in ITER as well as anticipated operational conditions for a DEMO-like reactor after ITER [9]. Under the normal operation phase, surface heat fluxes are ~ 1 and 10 MW/m² for the FW and the divertor of the reactor, respectively. In addition, the high transient heat loads during strong edge localized mode (ELM) of activity of the plasma or off-normal events like disruptions can cause ablation from the first wall surface. Tritium is absorbed by the PFMs or it can be chemically bonded to redeposition material. Therefore, an armor tungsten coating is expected to protect the FW due to its very low sputtering yield, low activation and high strength.

Table 1.1 Operation conditions for the plasma facing components of ITER and a DEMO-like reactor [9]

	ITER		Reactor	
	First wall	Divertor target	First wall	Divertor target
Component replacements	None	Up to 3	5 year cycle	5 year cycle
<i>Av. neutron fluence (MWa/m²)</i>	0.3	Max. 0.15 ^a	10	5
Displacement damage/ transmut. production (dpa/appm (He)) (dpa/%Re for W)	Be 1/1000 Cu 3/30 SS 3/30	CFC 0.7/230 W 0.7/0.15% Re Cu 1.7/16 SS 1.6/16	W 30/6% Re RAFM steel 120/1200	W 15/3% Re Cu 60/600 RAFM steel 60/600
<i>Normal operation</i>				
No. of cycles	30 000	10 000?	<1000	<1000
Peak particle flux (10 ²³ /m ² s)	0.01	~10	0.02	~10
Surface heat flux (MW/m ²)	<0.5	~10 ^b /3	<1	...10...
PFM operational temp. (°C)	Be: 200–300	W: 200–1000 CFC: 200–1500	W: 550–700	W: 350–500
ELM energy density (MJ/m ²)	–	<1	–	Reduced
ELM duration (ms)/{Frequency}	–	0.2/ {few Hz}	–	‘Grassy’?
<i>Off-normal operation</i>				
Peak energy density (MJ/m ²)	60 (VDEs)	30 (Disr.)	–	?
Duration (ms)/{Frequency (%)}	300 {1%} (VDEs)	1–10 {<10%} (Disr.)	–	1–10, max. 10 events

^a Without replacement.^b Slow transients 20 MW/m² lasting 10 s (10% frequency).

1.2. Objective

Reduced-activation ferritic/martensitic (RAFM) steels have been studied as FW material since the 1990s, while the significant challenge is the physical and chemical sputtering from the interaction between plasma and FW. For protecting FW from sputtering, tungsten has to be connected with FW made of RAFM steels. However, the method for realizing such kind of connection is restricted by many difficulties related to the large differences in the physical properties of both materials, particularly the large mismatch of their coefficient of thermal expansion (CTE). The large mismatch causes high thermally induced residual stresses at interfaces, particularly when the component is cooled down from the elevated process temperature to RT. The thermally induced residual stresses result in a reduction of the mechanical properties such as strength, ductility and toughness at the interface, especially during the thermal cyclic loading.

For reducing the residual stresses, an interlayer (Ti, V, Ni or Nb) with CTEs between those of W and EUROFER is used in many experiments that leads to tungsten/steel joints [10–15], either by brazing, hot isostatic pressing (HIP) or diffusion bonding successfully. In some cases, the bonding strength is even increased by Ti or Ni layers. Nevertheless, high macroscopic internal stresses still prevent the maximum possible of joint performance. In addition, to enable neutron irradiated material to be recycling-friendly, high activation elements such as Nb, Mo, Ni, Cu, Al, Si and Co should be avoided.

Another promising method to reduce the residual stresses is the application of functionally graded materials (FGMs) since it can reduce the thermally residual stress as much as designed by changing the composition of the materials gradually without bringing in the other metals. FG EUROFER97/tungsten coating is fabricated successfully and proved to be suitable as an interlayer for joining EUROFER97 and tungsten bulk material by diffusion bonding at 800 °C [16]. The joints with FGM are thermally cycled 10 times between 20 °C and 650 °C and are proved in their basic capability to withstand the operating conditions in a future fusion Tokamak reactor. The direct joints, by contrast, all samples diffusion bonded at 1050 °C fall apart in the post-bonding heat treatment in [14, 17]. The same problem happens to the direct vacuum plasma sprayed (VPS) tungsten coating, that the coated tungsten layer delaminates completely from the substrate [18]. Moreover, the high thermal stresses induced by the direct joints causes an exfoliation area during cyclic heat loads for VPS tungsten coating on F82H steel [19]. By the same method of VPS, tungsten coating with FG tungsten/Diamalloy is fabricated on Diamalloy steel successfully. Though further assessments on thermal cyclic loads and thermal shock response of FGM are lacking, the redistribution and relief of the residual stress are proved by finite element (FE) simulations [20].

A protective tungsten armor coating with a FG tungsten/EUROFER layer is investigated as FW application in the work. The parameters of FGM, particular the thickness and gradient and their effects on the reduction of the residual stress are analyzed. Considering the large area of FW (about 2 m²), an appropriate fabrication method is required to realize tungsten/EUROFER FGM. The assessments of the coating as FW application are performed in the work.

2 State of the Research

This chapter reviews the development of FW material and tungsten armor coating. The concept of FGM and its application in fusion, as well as the possible fabrication methods of FGM are concluded. The principle, characteristic and representation of VPS and the state of tungsten coating fabricated by this method are reviewed.

2.1. First wall materials and tungsten coating

2.1.1 Reduced activation ferritic/martensite steel

The early attempts to harness fusion power, the availability of structural components materials were the steels that performed well in fission reactors, for example, the austenitic steels and the low activation variant. Nevertheless, their disadvantages including swelling, inferior thermal properties, helium embrittlement and microstructural instabilities limit their further application as PFM [21]. RAFM steels are recognized as the primary structural material candidates for fusion blanket systems, on the basis of their high resistance to irradiation-induced swelling and the extensive industrial experience gained with the use of high-chromium heat-resistant martensitic steels (such as modified 9Cr–1Mo) [22].

F. W. Wiffen and R. T. Santoro have analyzed the effects of impurities routinely contained in steels. These impurities will in some cases dominate the long-term radioactivity characteristics of the steel. To reduce activation, the chemical compositions of steels are modified by replacing Mo and Nb with W and Ta, respectively [22]. The low activation ferrite steel working group of the International Energy Agency (IEA) reviews potential materials including the Japanese F82H and JLF-1, the US 9Cr-2WVTa steel, and the European steels LA12TaLC, CeTa, BATMAN and EUROFER. Main conclusions are that 7-10 Cr steel shows promising phase stability, resistance to temperature embrittlement, the best irradiation resistance and well qualified with established industrial processes [7]. Two references F82H and EUROFER have been selected in Japan and Europe, respectively, and their chemical compositions are shown in Table 2.1 [23]. The main compositional differences between them are the higher level of Cr content and lower W content of EUROFER, which bring EUROFER an improved corrosion resistance and an improved tritium breed capacity, respectively. The microstructure of EUROFER has been studied extensively [24-27]. The key characteristics of EUROFER, compared with F82H [23, 26] are: (a) A finer prior austenite grain size due to the increased concentration of the grain refining Ta, (b) A higher number of Ta and V rich secondary precipitate phases because of the increased concentration of carbide formers,

(c) Normalized EUROFER is fully martensitic and free of δ -ferrite, (d) Two types of carbide are present, the Cr-rich $M_{23}C_6$ type and the Ta/V-rich (Ta, V) C type. A comprehensive mechanical characterization has been studied on EUROFER. Charpy impact tests on EUROFER using ISO-V specimens show a DBTT of -70 °C [28]. The creep-rupture experiments between 450 °C and 650 °C up to 30000 h show satisfactory results, indicating long-term stabilities and predictability. Aging between 500 °C and 600 °C up to 10000 h does not significantly influence the tensile and impact properties, which reflecting high microstructural stability [28, 29].

Table 2.1 Specified chemical compositions of EUROFER and F82H steel

Steel	Cr	C	Mn	W	Ta	V	S	P	N ₂
F82H (wt.%)	7.7	0.09	0.16	1.94	0.02	0.16	0.002	0.002	0.006
EUROFER (wt.%)	9.0	0.11	0.40	1.10	0.06-0.09	0.15-0.25	<0.005	<0.005	0.03

The irradiation resistance of EUROFER has been performed at 300 °C from 0.2 to 10 displacements per atom (dpa). The yield stress increase observed from the tensile test is used to assess the irradiation hardening, which shows a continuous logarithmic hardening trend between 0.2 and 10 dpa with 280 MPa per decade dpa. Impact tests on KLST (Kleinst) specimens prove the superiority of Eurofer97 over F82H-mod [30]. Gaganidze & Aktaa [31] has reviewed the European irradiation programmes on assessment of neutron irradiation effects on mechanical properties and microstructure of EUROFER97 and other RAFM steels up to the year of 2013. The irradiation temperature ranges from the temperature ≤ 335 °C (including 60 °C, 250 °C, 300 °C and 325 ± 5 °C, and so on) up to the temperature of 400 °C, 450 °C and 550 °C. Low temperature ($T_{irr} \leq 335$ °C) neutron irradiation leads to strong hardening and embrittlement of EUROFER97, but there is nearly no impact on the mechanical properties at $T_{irr} \geq 400$ °C. In addition, the effect at low temperature can be completely recovered by post irradiation annealing at 550 °C for 3 h. A clear reduction of the hardening per dose increment is observed at achieved damage doses of 70 - 80 dpa. For EUROFER97 the saturation of hardening occurs at 70 dpa. Recently the irradiation behavior of oxide-dispersion-strengthened (ODS) EUROFER steel has been irradiated with neutrons to nominal dose levels of 1 and 3 dpa at 300 - 550 °C [32, 33] and up to 16.3 dpa between 250 and 450 °C [34]. Except that encouraging results on good irradiation resistance of EUROFER, the interactions between EUROFER with solid or liquid breeder have been investigated, and a good chemical compatibility with Li_4SiO_4 , Li_2TiO_3 and Be at least up to 550 °C at the reference gas composition of the purge flow has been observed. Besides, corrosion rates of EUROFER observed in PbLi are the lowest compared to all other investigated

RAFM [35]. For breeding tritium, a permeability of the hydrogen isotopes through the FW and structural components are important. Hydrogen/deuterium permeation experiments on EUROFER in the temperature range 473-723 K show a non-negligible decrease in permeability compared to F82H steel, and it remains about one order of magnitude higher compared with hydrogen/deuterium permeability of austenitic AISI316L steel [36].

2.1.2 Tungsten coating

As mentioned in the former section, an erosion protective coating for the FW of blankets is expected to reduce the physical and chemical erosion. Tungsten is considered as a promising material for fusion application owing to its low sputtering rate, low activity, high thermal strength and good thermal conductivity. There are actually two applications of tungsten and tungsten alloys in fusion: One is for plasma-facing armor. The other is for the structural component. M. Rieth et al. have given a comprehensive review including fabrication process development, a data base of structural tungsten materials as well as the production and thermal load resistance of armor tungsten materials [37, 38]. As introduced in section 1.1, the interaction and compatibility with the plasma particles and the extreme thermal operation condition of the FW will be also the main challenge for an armor tungsten material.

Thermal exposure experiments in Quasi-Stationary Plasma Accelerator (QSPA) facility in Russia are performed on ITER reference tungsten grades (deformed ones followed by heat treatment), in which the energy densities are ~ 0.3 to 2.0 MJ/m² with a plasma stream diameter of ~ 5 cm and a pulse duration of 500 μ s. The tungsten surface shows a thermal shock induced crack at an energy density of about 0.2 MJ/m² after 100 pulses, and primary and secondary cracks developed in the vertical direction are identified. A molten and re-solidified surface occurs at an energy density of 1 MJ/m² [39]. The influences of microstructure and mechanical properties on thermal shock response of tungsten are investigated in Forschungszentrum Jülich (FZJ) by using the Jülich Divertor Test Facility in Hot Cells (JUDITH 1) [40]. A combined thermal shock and steady-state heat loads (SSHLS) on actively cooled double-forged pure tungsten tiles has been performed in the electron beam facility JUDITH 2 at the surface temperature of 200 °C and 700 °C, respectively. The results show a damage threshold between 0.14 and 0.27 GWm⁻² up to 2.5×10^5 pulses. It seems that there is no significant difference for both surface temperatures [41]. In addition to standard grades with a purity of 99.97 wt%, ultra-high purity tungsten (W-UHP, 99.9999 wt%), tungsten alloys including tungsten with 1, 5 wt% tantalum (WTa1, WTa5) and a potassium-doped grade (WVMW, 15–40 ppm K), as well as tungsten coating deposited on two-directional carbon-fiber composite (CFC) substrate have been investigated at different base temperatures (from RT to 600 °C) and various power densities in FZJ [42]. As shown in Figure 2.1, J. Linke et al. have extracted a database of the threshold heat flux for no damage, surface modification

and crack network of 100 pulses. Pure tungsten grades and three kinds of tungsten alloys do not show any damage for power densities of 0.16 GWm^{-2} at $\Delta t = 1 \text{ ms}$ pulse duration for 100 pulses. The threshold heat flux for roughening of pure tungsten and tungsten alloys with relatively low concentrations of the alloying elements such as WTa1 or WVMW is below 0.3 GWm^{-2} . Their threshold heat flux for cracking is determined by the DBTT which is in the range of $100\text{-}200 \text{ }^\circ\text{C}$ for pure tungsten and $200\text{-}400 \text{ }^\circ\text{C}$ for tungsten alloy. Meanwhile, the tungsten alloy WTa5 has a significant improvement against thermal loads. High repetition rates ($10^3\text{-}10^6$ pulses) are performed on actively cooled tungsten tiles brazed to a water-cooled copper holder. The results show that no surface modifications at the power density of 0.2 GWm^{-2} for 10^3 cycles and only roughening after 10^4 cycles have been observed. Clear roughening and crack formation have been observed at the power density of 0.27 GWm^{-2} for 10^6 cycles [42].

Tungsten coatings on the CFC substrates with the parallel, perpendicular and felt directions to the surface of carbon fibers have been exposed to the similar ELM-simulation tests [42]. Tungsten coating ($25 \text{ }\mu\text{m}$) has a lower threshold (0.16 GWm^{-2}) for first cracks or delamination, and severely cracking even melting have been observed at 0.24 GWm^{-2} for 100 pulses. Different regions of CFC substrate have a significant impact on the response to the high heat flux. The region with perpendicularly aligned fibers shows the best CTE match, and the region with fibers oriented parallel to the surface shows the worst CTE mismatch. The heat removal is mainly due to the relatively high thermal conductivity of the fibers [42]. Tungsten coatings with three powder sizes ($63\text{-}80 \text{ }\mu\text{m}$, $80\text{-}100 \text{ }\mu\text{m}$ and $100\text{-}125 \text{ }\mu\text{m}$) are sprayed with a WSP[®] water stabilized plasma torch on copper and stainless steel substrates, respectively. Then 0.3 mm thick tungsten coatings are exposed to $0.2\text{-}1.1 \text{ GWm}^{-2}$ for $5\text{-}10 \text{ ms}$ in FZJ. A thin oxide layer on the surface is removed firstly at low thermal loads, and then surface melting at medium loads and deep melting at high loads are observed obviously. With the increasing of the loads, the whole coating is removed, the substrate is exposed, lateral cracks and local interfacial delamination occur due to the lamellar structure of the coating. No macrocrack is observed because of the lower thermal diffusivity and higher strain tolerance of plasma sprayed coatings. A threshold of roughly 0.5 GWm^{-2} for a macroscopic erosion of the tungsten coating is reported [43].

The thermal response to $0\text{-}8 \text{ MW/m}^2$ of VPS-W coatings on actively water-cooled Cu-CrZr substrates with a W/Cu interlayer and a W/Cu FGM are investigated, respectively. The surface temperature rises to $706 \text{ }^\circ\text{C}$ immediately at 8 MW/m^2 . After exposing at 6 MW/m^2 heat flux for 150 cycles, cracks are observed on the surface even the temperature of the surface do not increase significantly. After plasma irradiation, tungsten carbide and tungsten oxide are observed, and brittle cracks originated from sprayed droplets boundaries of the VPS-W coatings are formed at the surface. While cracks cross through the surface and propagate to the heat sink for W/Cu FGM with powder metallurgical technology. In addition, bubbles are observed on the surface of W/Cu FGM [44].

Comparing to hot-rolled commercially pure tungsten, thick CVD tungsten coating on a copper substrate has a higher cracking threshold under single shot disruption-like and repetitive ELM-like thermal shock loads mainly due to their columnar structure. The columnar structure is obviously helpful to avoid the reduction of thermal transfer and subsequent delamination. Specifically, crack threshold of CVD tungsten coating is located between 0.16 and 0.22 GW/m² at RT and the crack threshold temperature lies between 200 and 400 °C under 100 cycles ELM-like loading conditions, as shown in Figure 2.2 (a), and that for disruption-like loading conditions is between 0.28 and 0.33 GW/m² at RT [45].

The extreme thermal operation condition especially ELMs-like of all tungsten grades has been investigated well. Tungsten coating shows a comparable threshold as pure tungsten and tungsten alloy. Tungsten coatings on variable substrates, e.g. copper, CuCrZr alloy and stainless steel, have been exposed to high heat flux. For FW application of future DEMO thermal response of tungsten coating on RAFM steels has been investigated and reported in [19, 46, 47] since the microstructure and mechanical properties of the coating and substrate play an important role as indicated above.

The APS-W and VPS-W coatings [46] start to melt above 0.38 and 0.56 GW/m² respectively. They start to show cracking at even lower power density, 0.19 and 0.38 GW/m². A 0.6 mm thick tungsten coating with density 89% of the theoretical value is vacuum plasma sprayed on F82H substrate, and is exposed under three heat load conditions: (1) heat flux of 7.5 MW/m², duration of 180 s, (2) cyclic irradiations of 60 s on and 140 s off with a heat flux of 12 MW/m² with total 30 cycles and (3) cyclic irradiations of 7 s on and 230 s off with a heat flux of 40 MW/m² with total 30 cycles. In addition, quantitative temperature profiles and thermal stresses from those heat loads are analyzed by Finite Element Analysis (FEA). The delamination occurs near the interface between VPS-W coating and RAFM at 1300 °C of surface temperature which is induced by the thermal stresses, as shown in Figure 2.2 (b) [19].

Irradiation experiments show that the high deuterium (D) retention at 50°C is due to D₂ molecule accumulation in the cavities and pores and chemisorption of D atoms on the sample surface and on the inner surfaces of closed pores. The molecular D₂ fraction can leave from the pores at 280 °C, which corresponds to the dissociation energy of 1.4 eV. D atoms adsorbed on inner surfaces can be desorbed at 480 °C, which corresponds to the binding energy of 2.1 eV [47]. It seems that tungsten coating is appropriate to be considered as a plasma facing armor, and thermal response to heat loads as well as plasma particle compatibility of tungsten coating are in progress. Nevertheless, the large mismatch in CTE between tungsten and EUROFER could induce not only thermal stresses under cyclic heat loads [19], but also the failure during the fabrication process [18]. The concept of functionally graded materials (FGMs) for reducing the residual

thermal stress and realizing the joints of tungsten coating and EUROFER substrate has been developed in the recent years.

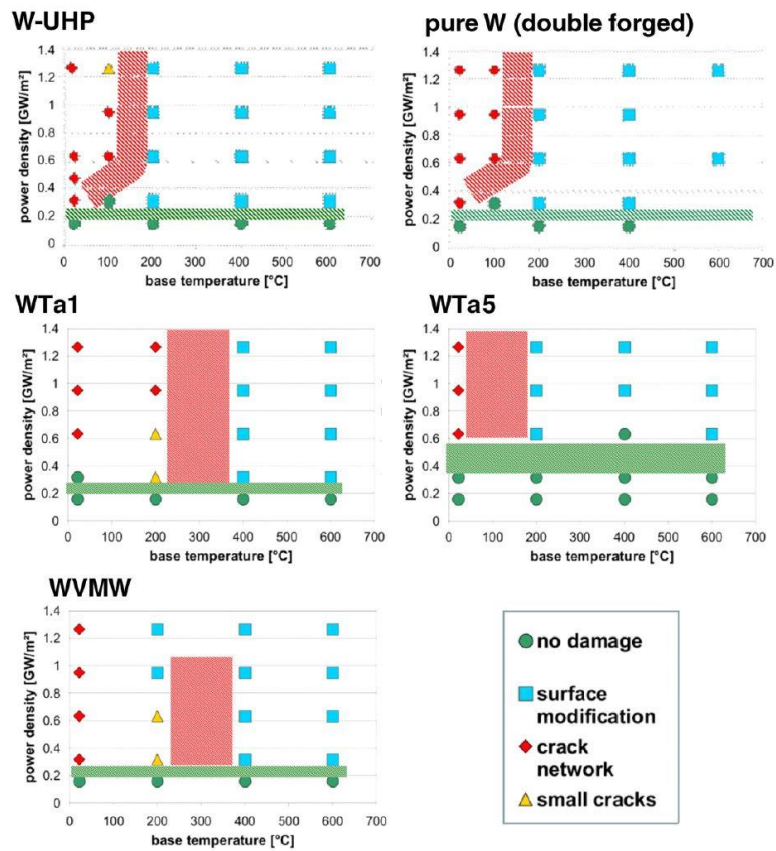


Figure 2.1: Thermal shock induced surface modifications in different tungsten grades after 100 pulse and 1ms duration [42].

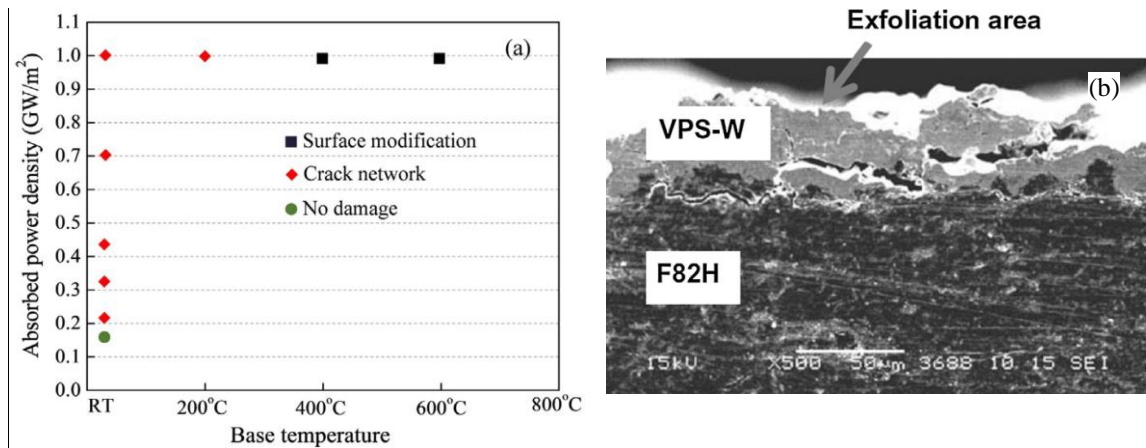


Figure 2.2: (a) CVD tungsten coating exposed to ELMs-like thermal shock at power densities of 0.16–1.0 GW/m² for 1 ms, 100 pulse [45]; (b) Cross section after heat loading of experimental condition 40 MW/m², 7 s, 30 cycles [19].

2.1.3 Functionally Graded Material (FGM)

The concept of FGMs was proposed in 1984 by materials scientists in Japan as a mean of preparing thermal barrier material. FGMs are essentially two-phase composites in which the volume fractions of the constituents vary continuously and gradually in the thickness direction resulting in a corresponding change in the microstructure and properties of the material [48]. FGMs are discussed and applied in many fields widely after the proposing of its concept. S. Uemura [49] concluded the new applications of FGMs including optical transmission application, graded index plastic optical fiber, cutting tools and application of FGM on the reduction of thermal stress, et al. in the first 20 years since 1984. In the recent years, the concept of FGM is introduced as an application of PFC in fusion. As introduced above, tungsten is considered to be a promising armor material to protect FW, therefore, the studies on W/Cu FGMs and W/EUROFER FGMs have been proceeding theoretically and experimentally for years. The main difficulty for joining W to Cu or steel directly is the large mismatch of CTE ($\alpha_{Cu} \approx 4\alpha_W$ and $\alpha_{EUROFER} \approx 3\alpha_W$) which could lead to the large thermal residual stress. The application of FGM could bring gradient properties, especially a gradient CTE.

The earliest study on W/Cu FGM was performed by M.M. Gasik in the 1990s for the application of upper divertor plates of ITER [50]. The micromechanical model and the theoretical analysis of the W/Cu FGM divertor have been shown in [51] by considering temperature-dependent properties and elasto-plastic behavior of the material. The effects of the gradient parameter p on the temperature distributions and on the thermal stress distributions have been investigated which is quite useful in the initial stage. Where $p=1.0$ corresponds to the linear variation of properties of FGM; for $0 < p < 1$ the FGM layer is Cu-rich and for FGM $1 < p < \infty$ it is W-rich. Both the temperature distributions and the plastic deformations in the x -direction near the surface increase with the increasing parameter p . In addition, the plastic deformation affects predominantly the

stress distributions of the W phase near the surface and the Cu phase of the FGM. The effect of plastic deformation on the thermal stress distribution in the x and z-direction in different region for $p = 1.0$ has been also concluded.

The idea of W/steel FGM is proved firstly by finite element (FE) simulation. Two and four stepwise linear layers, linear and quadratic gradient [52] have been simulated for the helium-cooled divertor design developed at KIT [53]. Elasto-plastic and elasto-viscoplastic simulations have been performed under the variation of the layer thickness, layer orientation and gradient function. The resulting stresses and strains are used as the basis for the subsequent lifetime estimation. Cycling of temperature comes along with the design of a Tokamak reactor and yields failure of the joint due to fatigue and creep. For the determination of the number of allowable cycles, fatigue as well as creep damage are considered in the evaluation of the EUROFER part. For the tungsten part creep is neglected. The lifetime of the joining layer could not be assessed due to the lack of experimental data. However, the improvement in the lifetimes of the joined parts could be observed at least qualitatively. The performed FE-simulations show that a functionally graded joint between tungsten and EUROFER can drastically decrease the thermal mismatch stresses and strains occurring in the divertor component and thus improve its failure behavior during thermal cycling. Specifically, as shown in Figure 2.3 (a), the maximum equivalent inelastic strain of all the FE-models decrease obviously with the increasing of the thickness, and that of two and four layers lay between the brazed and the linearly graded joint, while the joint with the quadratic gradient function provides a gain of about a factor of two [52, 54]. Similar work simulating bi-layer (no interlayer), an interlayer (one layer), 5-layer, 11-layer with linear gradient and 11-layer with parabolic gradient ($n=2$) between tungsten coating and Diamalloy steel has been performed [20]. The main conclusion as shown in Figure 2.3 (b) include that a reduction of stress at the interface with increasing compositional graduation, and a reduction of stored strain energy, especially for the FE-model with a linear compositional gradient. The stress and stored strain energy are the driving force of the delamination, within the coating and particularly at the interface.

As expected, the application of FGM has been proved not only to combine the advantages of W and EUROFER, but also to release the residual stress and reduce the stored strain energy as well as the inelastic strain. The linear gradient of FGM behaves well in both simulations, while stepwise layers with a linear variation of the compositional ratio are introduced as representatives of linear gradient in actual fabrication processes since it is not possible to realize the desirable smooth gradient of chemical composition.

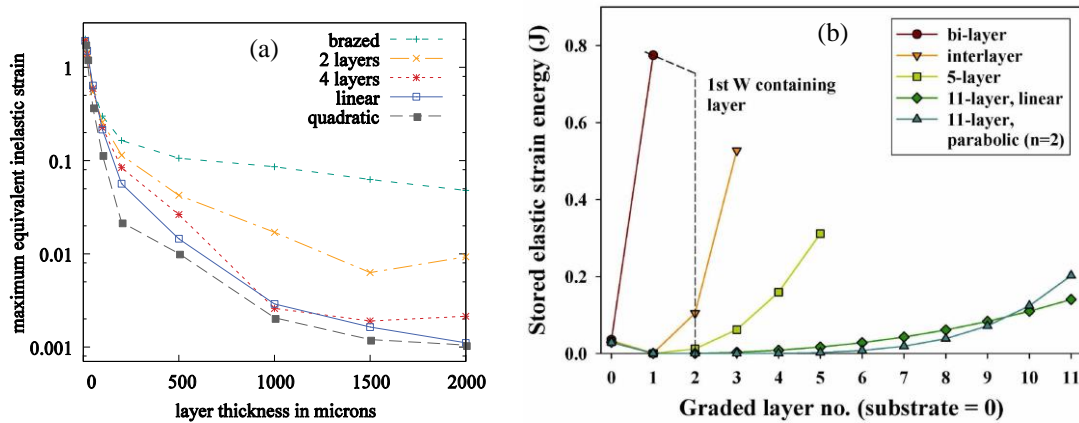


Figure 2.3: (a) Dependence of the maximum equivalent inelastic strain after 100 cycles on layer thickness for various gradient functions [52]; (b) Variation of stored elastic strain energy with graded layer number [20].

2.1.4 Fabrication method comparison of FGM

Considering the analysis of section 2.1.3 and economical and technical reasons in practice fabrication process, stepwise linear gradient is mostly considered for fabricating FGM. Due to the differences of both materials' melting and sintering temperatures, traditional sintering method is not suitable for the fabrication of FGM. A sintering and infiltration technique was approved by Y. Itoh in 1996. The main fabrication process is to make sintered tungsten with graded pores, then molten copper is infiltrated into the graded pores [55, 56] or make a gradient tungsten skeleton by electrochemically processing, then following is the infiltration of molten copper [57]. The infiltration method usually consists of two steps: the formation of a gradient tungsten skeleton and infiltration of molten copper. The fine gradient range, the dense material at moderate cost and several millimeters thickness of FGM could be realized, but the feasibility for large scale is limited by the first step. Another novel sintering method combined resistance sintering and ultra-high pressure (RSUHP) is also used successfully in the preparation process of W/Cu FGM [58-61] and W/steel (Fe) FGM [16, 62]. The advantages of RSUHP are the full graded level of FGM, low cost and efficient fabrication, while the drawback of no vacuum could not be ignored, a large-scale sample is also not feasible.

Explosive compaction is the method that explosive energy is used for compacting and consolidating metal powders. The W/EUROFER FGM within a range of 0 and 60 vol. % of the tungsten concentration is achieved, but several defects including inhomogeneous microstructure with pores and the formation of intermetallic phase need be avoided by a further great effort [54]. In addition, due to the complexity of instrumentations to pre-heat all the materials the reliability to manufacture thick W/EUROFER FGM on a large area of the substrate is dubious. Electrodeposition is utilized for producing W-Fe alloys with various tungsten compositions [63, 64]. The deposition of FGM is possible by varying the potential and current density if the deposition potentials of components are

fairly different. However, an intensive work need be done in order to obtain a fully graded W/EUROFER FGM.

Magnetron sputtering is one of coating techniques based on the physical vapor deposition method, which facilitates the fabrication of a dense and fully graded W/EUROFER FGM at a relatively low process temperature. Dense W–Cu–W multilayer with a limit thickness deposited on Fe substrate [65], and a dense W/EUROFER FG coating within a range of 33 and 87 at.% of the tungsten concentration [16] are obtained by magnetron sputtering. However, the low deposition rate makes this method unfeasible for depositing thick layers.

Laser sintering is introduced for fabrication of W/Cu FGM. Laser sintering, also called “laser casting”, “3D cladding” or “laser cladding” “laser metal deposition”, it uses a laser to form a melting pool on the substrate in which the powder is injected and melted. The main drawback is that an assembly of a graded structure is only possible when the starting point is at the Cu side [66]. For W/EUROFER FGM fabricated by this method, the formation of intermetallic phase can hardly be avoided due to the very high temperature. Therefore, despite all the benefits of the method showed in Table 2.2, the formation of brittle phase restricts the application of the method for W/EUROFER FGM.

Plasma spraying is another widely introduced method, which includes air plasma spraying (APS) [67] and vacuum plasma spraying (VPS) [16, 68]. APS is replaced increasingly by VPS owing to its oxidation problem, in which the oxygen content of the whole coating is higher than 1 wt% [67]. As shown in the Table 2.2, VPS seems to be a very promising process which fulfilling all criteria. The criteria of fabrication methods for FGM should have a sufficient thickness, fine gradient range and vacuum condition, in addition, the feasibility for a large scale should be also taken into account in the selection of fabrication methods because of the large scale of FW ($> 2 \text{ m}^2$).

Table 2.2 Comparison of the fabrication methods, -/+ stands for un-/appropriate and • for unknown

Fabrication method	FGM	Gradient range	Thickness	Vacuum	Large scale	No. of Reference
Infiltration	W/Cu	+	+	+	-	[55-57]
RSUHP	W/Cu W/EUROFER (Fe)	+	+	-	-	[16, 58-62]
Explosive compaction	W/EUROFER	+	+	+	-	[54]
Electrodeposition	W-Fe alloy	•	+	+	•	[63, 64]
Magnetron sputtering	W/Cu W/EUROFER	+	-	+	+	[16, 65]
Laser sintering	W/Cu	+	+	+	+	[66]
Vacuum plasma spraying	W/Cu W/EUROFER	+	+	+	+	[16, 67, 68]

2.2. Vacuum plasma spraying

2.2.1 The principle of vacuum plasma spraying

The definition of thermal spray technology is given in the Thermal Spray Terminology compendium [69] as: “thermal spraying comprises a group of coating processes in which finely divided metallic or nonmetallic materials are deposited in a molten or semi-molten condition to form a coating. The coating material may be in the form of powder, ceramic rod, wire, or molten materials.” According to the way of providing energy or heat to melt the material, thermal spray is divided into two main parts as shown in the Figure 2.4. Plasma spraying is the most versatile among all thermal spray processes since there are few limitations on the sprayed materials and substrate materials, size and shape. In addition, the coating quality is in general higher than that obtained with flame spraying. The coating quality, i.e., density, uniformity, and reproducibility of spraying in a controlled environment, i.e., a controlled atmosphere chamber or in a low pressure environment (low pressure plasma spraying or vacuum plasma spraying, LPPS or VPS) can be enhanced comparing to that of spraying in an open air environment [70].

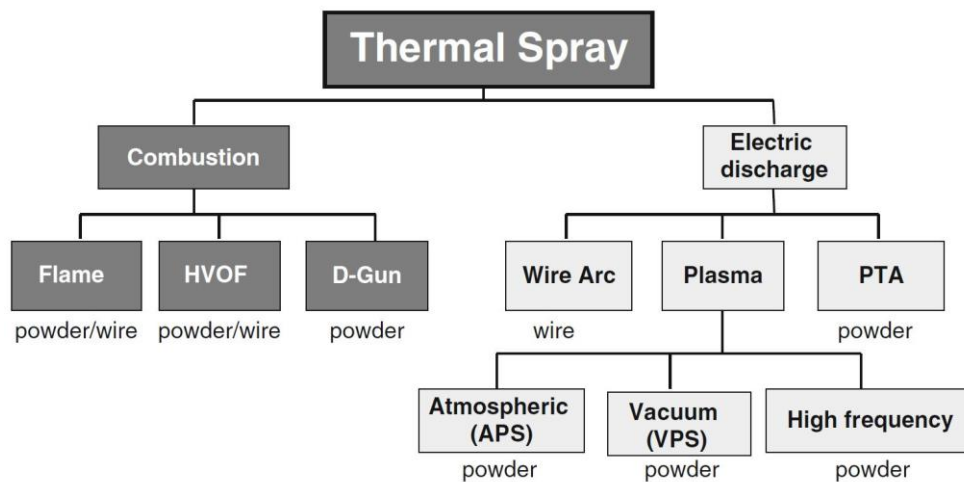


Figure 2.4: Classification of thermal spray technologies [70].

In VPS process, an electric arc generates plasma within a plasma torch in the vacuum chamber. The arc is struck between a cathode and an anode nozzle, and then the plasma gas is injected at the base of the cathode and heated by the arc, and the plasma exits the nozzle as a high temperature, high-velocity stream as shown in the Figure 2.5. Peak temperatures at the nozzle can be 12,000-15,000 K, and peak velocities range from 500 to 2,500 m/s [70]. The spraying powders are melted and accelerated by the plasma and transported to the substrate where they form splats and eventually the coating. A

movement of the torch relative to the substrate and/or a movement of the substrate relative to the torch form uniform coatings on a substrate.

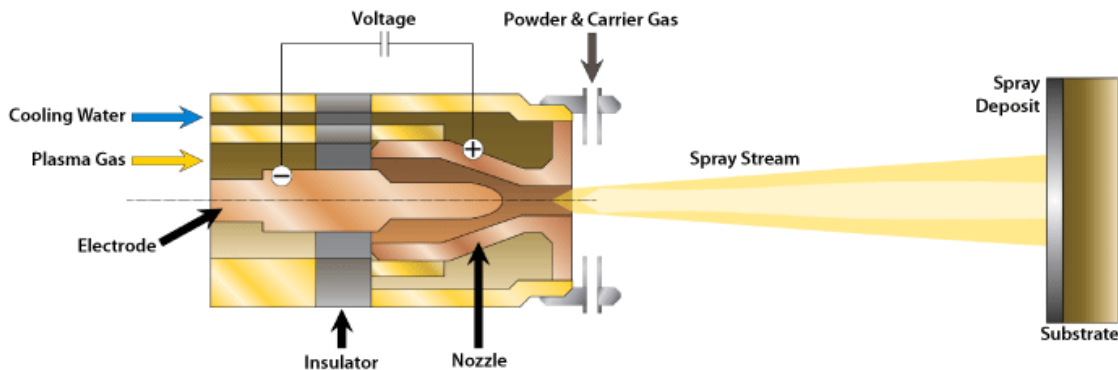


Figure 2.5: Schematic of the plasma spraying process.

The summarized spray parameters are shown in the Figure 2.6. The coating properties mainly depend on the substrate morphology, condition and temperature, as well as the powder size, temperature and velocity of the sprayed particles. Specifically, the preheated temperature and roughness of the substrate play an important role in the coating quality. In general, a higher substrate temperature is advantageous for the formation of a well-defined columnar microstructure [70]. The higher substrate temperature could bring metallurgical bonding instead of mechanical interlocking for in-situ repair of damaged beryllium surfaces [71]. The preheating temperature of the substrate before spraying, coating generation during spraying and cooling process after spraying, also affect the residual stress distribution [70].

Except that the substrate temperature, one of the most critical steps for improving the bonding and adhesion of the coating is the preparation of the substrate prior to spraying, and this preparation comprises generally three steps: cleaning, roughening and a second cleaning of the surface. The purpose of roughening the surface is to provide asperities or irregularities to enhance coating adhesion and provide a larger effective surface. In most cases, roughening is achieved by grit blasting, sandblasting or electrochemical machining which also induces compressive stress on the substrate.

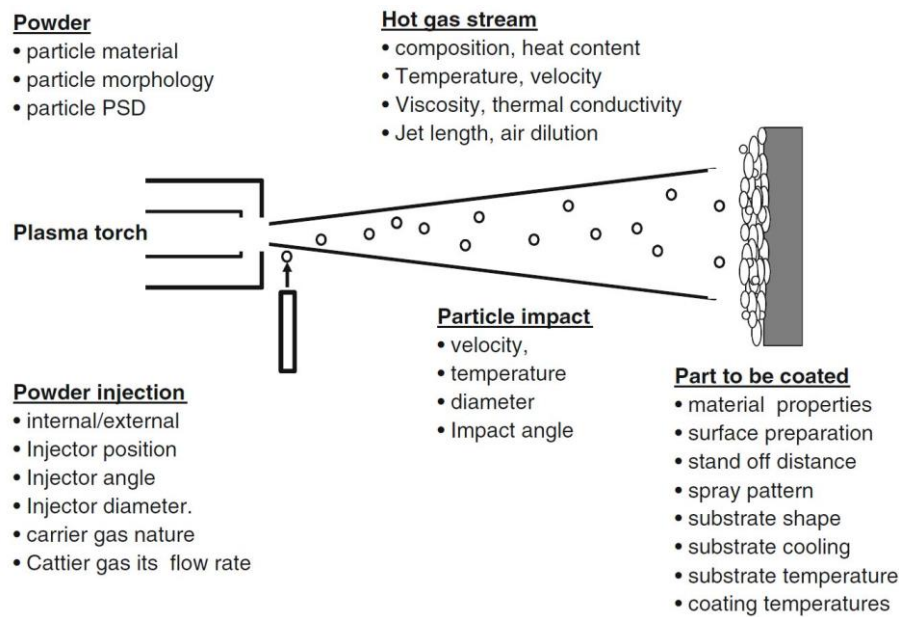


Figure 2.6: Different spray parameters [70].

Several aspects of powder quality can affect coating performance, including the powder feedstock morphology and the distribution of the particles size, the transport properties of the powders and the injection technique which can have a major impact on the particle velocities, temperatures, and indexes of melting. P. Fauchais et al. [72] have summarized the effects of the sprayed powder characteristics on coating qualities. In general, poor flow ability results in fluctuations of the powder feed rate and thus results in inhomogeneous coating structures. Powder morphology, resulting from their manufacturing process, is also a key parameter for particle behavior upon penetration within the plasma jet, elongation ratio and dense/porous macrostructure. The particle size of the powder is around 10-100 μm for making sure that the powder is heated up homogenously and melted well, as well as for decreasing the influence of the electrostatic charge of the particles.

2.2.2 Characteristics and representation of VPS coating

Thermal spray coatings result from stochastic processes, where particles are accelerated and then melted, in the end, they are flatted and formed the coating [73]. Particles melting occur in rather short times (a few milliseconds) and their solidification in even shorter times (a few microseconds) with strong temperature gradients and cooling rates in the range of 10^6 - 10^9 K s^{-1} . That results sometimes in metastable or amorphous phases [74]. According to the melting temperatures of the particle, the state of the particle may be molten, semi-molten, or solid when it impacts on the substrate or pre-coated surface. The state of the particle affects the final microstructure of the coating [75]. The particle after flattening is called splat and is characterized by the flattening particle diameter D . There are two kinds of splats' morphology, as shown in Figure 2.7. One is disk-shaped

splat with less and short “fingers” and the other is splash-shaped splat with extensively “fingers”. When modelling the flattening of a nickel droplets on a smooth stainless steel substrate preheated to 563 K, after a relatively symmetrical flattening stage (up to 1.4 ms) digitations start to appear resulting in an extensively fingered splat [76]. The reason for the different morphology of splat is very complex, however, the preheating temperature of the substrate and the wettability between the particle and substrate play a key role in the splat morphology. Fukumoto et al. confirm a transition temperature of the preheated substrate above that the disk-shaped splats are obtained. The transition temperature for mild steel and AISI304 steel is around 300 °C, and it will be higher when the thermal conductivity of the substrate is greater [74, 77]. The transition temperature of 400 °C is estimated for a stainless steel in Ref. [76]. Splash-shaped splats tend to occur more readily for the poor wetting that leads to an initial rapid solidified layer and poor flowing of the liquid metal. Splash-shaped splats are normally accompanied by pores and weak interface bending strength.

Due to the insufficient heating power of plasma, few un-melted particles exist among flattened lamellae. In addition, the well melted flattened lamellae could not flow adequately during the short time of solidification, which leads to the pores among lamellae. In a word, characteristics of VPS coating are splat, un-melted particles and pores.

The evaluation of the VPS coating quality consists of microstructure and mechanical aspects. Speaking of microstructure, porosity is one of the most important characteristics for assessments of coating, and porosity is decided by spraying atmosphere and spray parameters. Normally, APS coating shows a higher porosity comparing to VPS coating due to the oxidation of pre-coated layer during the time interval of spraying. Once the remarkable oxidation occurs, strong sticking of the melted droplets on the surface will become difficult and as a result large pores will be formed. For instance, Y. Yahiro et al. [46] produce two kinds of tungsten coatings with the thickness of 1 mm on ferritic/martensitic steel F82H substrates by VPS and APS respectively. The porosity of the VPS-W coating is 0.6% while that of the APS-W coating is 6%, and most pores of the VPS-W coating are smaller than 1-2 μm in size comparing to $>10 \mu\text{m}$ of the APS-W coating.

Mechanical representations consist of mechanically induced stresses (stresses due to grit blasting and peening effect et al.), residual stress, coating adhesion and toughness.

Considering the representation of FGM, volume fraction is the most important microstructural parameter of interest for FGM. The volume fraction of phase b, expressed as $V_v(\beta)$, is given by:

$$V_v(\beta) = \frac{V_\beta}{V_0} \quad (2.1)$$

where V_β is the volume of the phase b within the test region and V_0 is the volume of the test region.

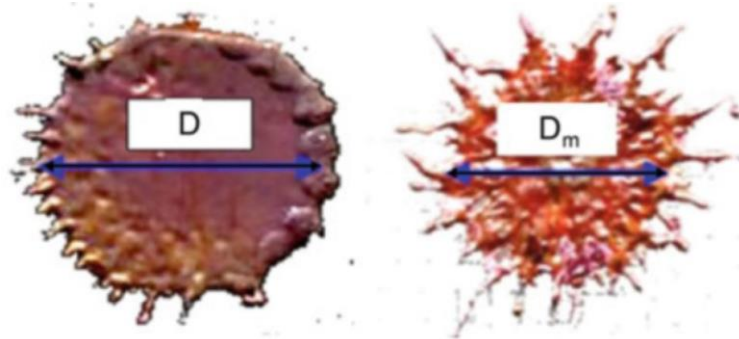


Figure 2.7: Definition of the splat (YSZ) mean diameter: (a) Disk-shaped splat and (b) splash-shaped splat [70].

2.2.3 VPS tungsten coatings on RAFM steel substrates

VPS has been applied to produce tungsten coatings on steel substrates for several years, and the thermal load responses of several kinds of VPS W coatings have been introduced in Section 2.1.2. The microstructure characteristics and the development of VPS W coatings on RAFM steel substrates are summarized in this section.

The microstructures of both tungsten coatings produced by Y. Yahiro et al. [46] have a columnar structure inside re-solidified pancake-like depositions, but large round-shaped un-melted W powders are observed. T. Tokunaga et al. [78] summarize three kind grains of tungsten coating, their formation reason and the effect on properties, respectively. Grains of tungsten coating include large round grains of about 15 μm in size, fine randomly oriented grains less than 1 μm and columnar grains with the aspect ratio more than 2.5. Specifically, well-melted powders pile up as compressed particles in which columnar grains are developed. Few large pores are formed and the contact area between the compressed particles looks very good. Large grains are formed owing to the re-solidification or non-melted completely particles. And there are many pores and very fine grains around the un-melted and re-solidified particles, respectively. The temperatures of the substrate vary from 841 K to 1429 K. With increasing the substrate temperature, the fraction of columnar grains increases while the fraction of un-melted grains and the number of pores decreases. The fraction of columnar grains in the W layer formed with powders having an average size of 37 μm is about 20% higher than that of 18 μm -powders over the whole temperature range. It is likely that large melted powders can stay longer in a liquid state after deposition on a substrate due to their higher heat capacity. The effects of substrate temperature on coating quality including splat morphology, grain size and inter-splat sintering are investigated in another publication [79], and the main conclusion is that substrate temperature above 400 $^{\circ}\text{C}$ is beneficial for forming of dense coating with good thermos-mechanical properties.

A systematic roughening or sculpturing of the substrate surface is beneficial for improving the adhesion of VPS coatings on the substrate [20]. To release residual stress and to improve the adhesion between tungsten coating and the steel substrate, already in early experiments an interlayer W/steel composite has been produced by VPS [47]. Typical results of microscopy are many parallel layers of overlapping and not completely molten W particles, as well as very high porosity which is up to 20%. However, no crack propagation or delamination is observed. It seems that the porous structure constrains the propagation of fissures or cracks. The coatings with a W/steel interlayer survive long pulse and cyclic heat load test up to 2.5MW/m^2 without any damages.

However, macroscopic porous and the crack-like defects contribute to the high porosity, their effects on the reduction of thermal diffusivity are simulated in [80]. The reduction of thermal diffusivity reaches a value close to 90% in the saturation zone due to defects and globular pores, although the total volume fraction of the porous is just 25% [80]. Therefore, tungsten coatings with few pores and defects and accordingly a high thermal conductivity, as well as less residual stresses are essential when used as FW in fusion.

3 Approach and Methods

In the chapter the approach including three main strands was described for developing FG W/EUROFER coating system. For assessing the quality of the coating system, the microstructural and mechanical investigation methods were introduced.

3.1. Approach

3.1.1 Determination of FG-layer thickness by Finite element simulations

To determine the thicknesses of FGM, the simulations have been performed using the finite element (FE) code ABAQUS. FE-simulation considering elastic-viscoplastic material behavior is performed to simulate both fabrication and operation process of FW. Comparing the reduction of residual stress and inelastic strain as well as improvement of the lifetime the appropriate thicknesses of FG W/EUROFER coating are specific for fabrication.

3.1.1.1 Model and boundary conditions

The 2D sketch and mesh of the FE-model are shown in Figure 3.1. The upper and bottom sections consist of W coating and EUROFER substrate with the thickness of 0.5 mm and 18 mm, respectively. W/EUROFER FG-layer between them has variable thicknesses. For simulating the thick cross-section with a constant strain in the thickness direction generalized plane strain elements are used.

The FG-layer is varied in thickness from 0.1 mm to 4 mm. A field variable f ranging from 0 to 1 is used to indicate the gradient level. It has the value 0 for the W side and 1 for the EUROFER side. For f values between 0 and 1, the material properties of FG-layers are interpolated linearly. It is necessary to use adequate meshes for each thickness since the FG-layer thickness is in a range over two orders of magnitude. Mesh with varying element size is used as shown in Figure 3.1, and it is designed in such a way that the highest strain and stress, as well as their gradients, always lie inside its densest element region. The minimum element is with a size of $50 \mu\text{m} \times 50 \mu\text{m}$. This minimum element size is kept to be constant along all FE-models to obtain comparable results.

The x- and z-axis are perpendicular to the symmetry axis, which coincides with the y-axis. The two bottom corner nodes are fixed in the y direction so that the FE-model cannot drift away. On the right edge, slider constraint as a multi-points-constraint of user subroutine is applied as one boundary condition which can simulate the large scale

of the whole coating in the XZ plane since the edge effect is well known and is not considered here.

The FE-model is loaded by a homogeneous temperature field varying with time assuming a cooling down from the hot manufacturing process temperature. The manufacturing temperature is the initial stress-free temperature of the whole FE-model and is set to 750 °C. Thereafter the FE-model is loaded by varying the temperature homogeneously with time starting with a linear cooling down to 20 °C within 100 s. After this phase the temperature alternates between 20 °C and 600 °C with a dwell time of 24 h at 600 °C what corresponds to an operation cycle of the fusion reactor. Since the creep, particularly of EUROFER, becomes significant at least during the long dwell time period at 600 °C, the operation cycles has been conducted by performing nonlinear elastic-viscoplastic analyzes. The ramping up and down of the temperatures occurs linearly during the operation cycle.

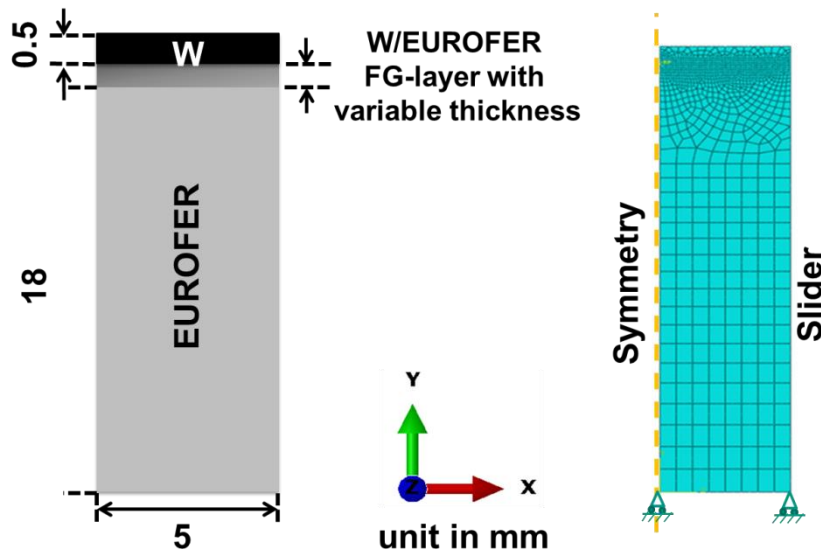


Figure 3.1: The sketch and mesh of the FE model.

3.1.1.2 Material behavior and properties

In the simulations of the first cooling down phase, all the materials are considered to behave isotropic, linear elastic and perfectly plastic. The CTE, Poisson's ratio, Young's modulus and yield strength are assumed to be temperature dependent. Table 3.1 lists all basic material properties required and used in the simulations. In addition, the properties of the FG-layer are interpolated by the properties of W and EUROFER. For the simulations of the operation phase Norton power law of creep is taken into account in addition, and the formula (3.1) is used, being a likely assumption based on a multiplication of the gradient factor f with Norton creep parameters C and n [52]:

$$\dot{\epsilon}_{Cr} = f \cdot C \cdot \sigma^{f \cdot n} \quad (3.1)$$

C and n are temperature dependent properties determined for EUROFER and given in Table 3.2 [81]. f is equal to 0 for tungsten since its creep is accordingly neglected at 600 °C.

The temperature dependence of the material properties is usually given by their values at certain temperatures whereas the values at temperatures in between are determined by linear interpolation. This linear interpolation is only supported by ABAQUS, what is sufficient for the parameter n , but not adequate for the parameter C , which ranges over more than 60 orders of magnitude. Therefore a so-called ‘user subroutine’ has been programmed to realize for the parameter C a logarithmic interpolation instead [52].

Table 3.1: The basic properties of materials

Temp. °C	EUROFER			W		
	E- module MPa	Yield stress MPa	CTE k ⁻¹	E- module MPa	Yield stress MPa	CTE k ⁻¹
20	217260	545.57	12×10 ⁻⁶	397938	1360.46	4.4×10 ⁻⁶
200	207327	483.62		397270	1154.17	
400	197123	446.99		394480	947.86	
600	177589	298.32		389508	764.79	

Table 3.2: The creep properties of EUROFER

Temp. °C	n	C 10 ⁻⁶ h ⁻¹ MPa ⁻ⁿ
20	23	1.000E-80
450	22.718	8.352E-57
500	21.190	1.3758E-50
550	17.769	4.5660E-40
600	9.5095	2.4898E-19

3.1.2 Fabrication of the coating system

As indicated in Section 2.1.4, VPS is the most promising method to deposit FG W/EUROFER coating system mainly owing to its several advantages. On one hand, the designed parameters of FGM including full range of gradient and sufficient thickness can be well realized by VPS. On the other hand, the method can be utilized to manufacture large-scale samples. VPS was performed in Forschungszentrum Jülich (FZJ) in this work.

3.1.2.1 Raw materials

(1) EUROFER substrate

EUROFER97 plate with the thickness of 25 mm was ordered from German manufacturer Saarschmiede, and the heat number is 993402. EUROFER substrates with the thickness of 18 mm were achieved after a milling processing. The roughness of the steel plate was measured, and the directions of the measurement were parallel and perpendicular to the rolling direction, respectively, as shown in Figure 3.2. Table 3.3 shows that the roughness at different directions and positions are quite uniform, and the uniform roughness shows a homogenous smooth substrate surface. For a better bonding strength, substrates were sandblasted to get a rough surface with $3.96 \mu\text{m}$ of R_a and $27.9 \mu\text{m}$ of R_q before spraying processes. The deposition of the sprayed coatings was performed on EUROFER substrates with the dimension of $100 \times 100 \times 18 \text{ mm}^3$.

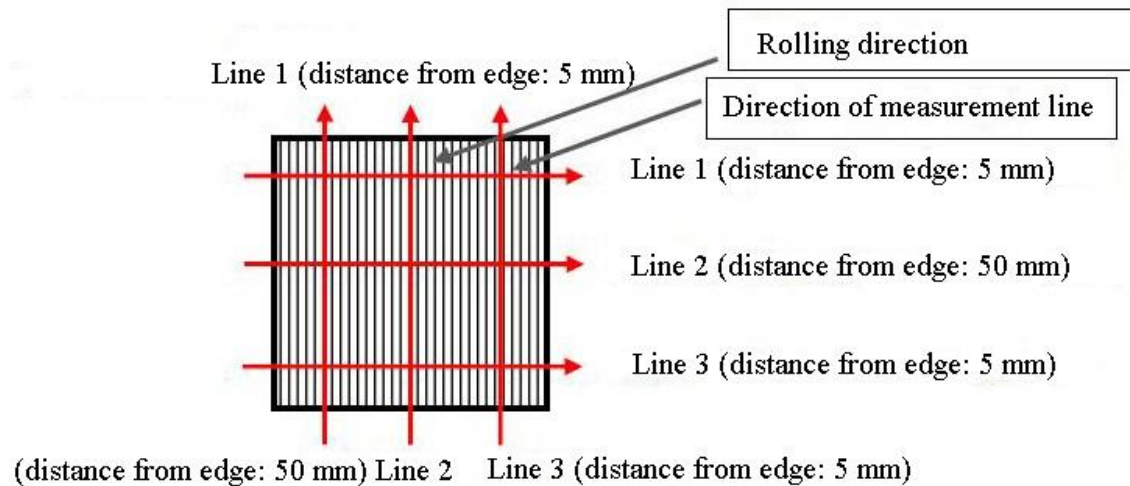


Figure 3.2: The schematic of measurement direction on original EUROFER substrate plate.

Table 3.3: Roughness of original EUROFER substrate

Roughness	Parallel to the rolling direction			Perpendicular to the rolling direction		
	Line 1	Line 2	Line 3	Line 1	Line 2	Line 3
R_a (μm)	0.497	0.481	0.482	0.500	0.487	0.517
R_q (μm)	0.673	0.605	0.612	0.645	0.628	0.676
$R_z(\text{DIN})$ (μm)	5.388	4.026	4.729	5.709	5.480	7.612

(2) Tungsten and EUROFER powders

Tungsten powder used in this work was delivered from PLANSEE, Austria and has the trade name AW3105A25. The typical purity and mean particle size are 99.95% and 12 μm , respectively. Figure 3.3 shows the particle size distribution, which is measured by laser diffraction. The particle size distribution of spheroidized EUROFER powder is shown in Figure 3.4. The d_{50} particle size is equal to 53.2 μm . The chemical compositions of both powders are summarized in Table 3.4.

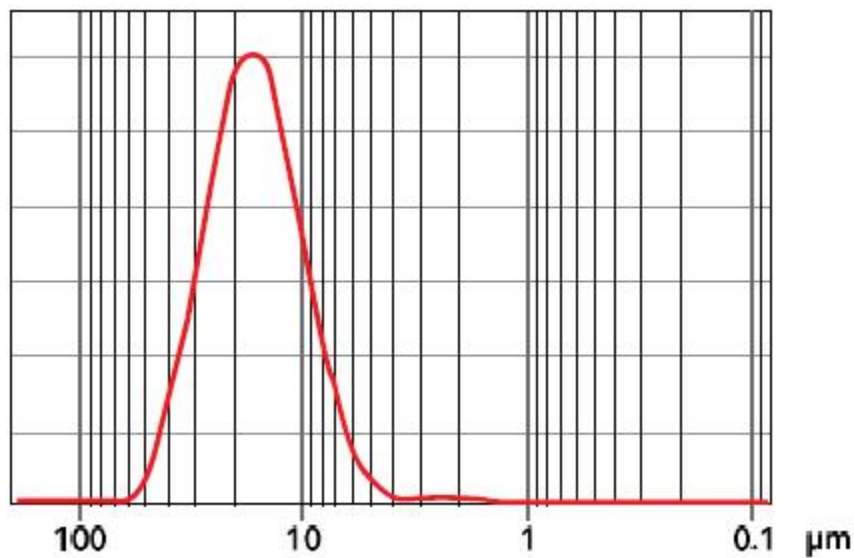


Figure 3.3: The particle size distribution of tungsten powder.

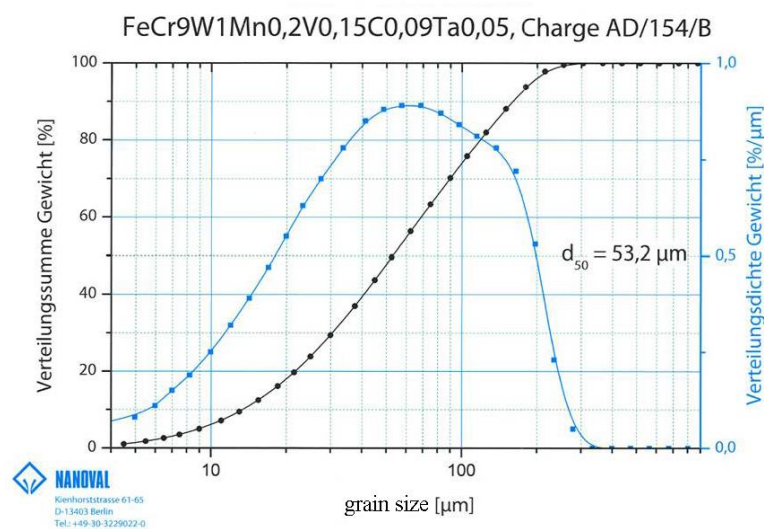


Figure 3.4: The particle size distribution of EUROFER powder.

Table 3.4: Chemical composition of tungsten and EUROFER powder used in this work

Tungsten (wt%)	W	O	Al (ppm)	Ca (ppm)	Cr (ppm)	Fe (ppm)	K (ppm)	Mo (ppm)	Na (ppm)	Ni (ppm)	Si (ppm)
	99.95	0.02	<5	5	150	150	<5	10	<5	100	10
EUROFER (wt%)	Fe	Cr	C	Mn	V	W	Ta	N	O	P	S
	balance	0.097	0.097	0.38	0.186	1.096	0.037	0.048	0.023	<0.008	0.0073
		Ni	Cu	Si	Co						
		0.0143	0.0067	0.023	0.0035						

3.1.2.2 Vacuum plasma spraying

(1) Facility and parameters

A F4 plasma gun from Sulzer-Metco (Wohlen, Switzerland) was applied to spray tungsten coating and FG W/EUROFER layer on EUROFER substrate. With the power of 50 kW, the temperature within plasma can be higher than 10,000 K. Powders were injected into plasma with a velocity of several 100 m/s, melted by the heat of plasma during spraying process within a spray distance of 30 cm, and re-solidified on the sandblasted EUROFER substrate. The substrate was preheated to the temperature of ~ 750 °C before spraying. Both powders were injected simultaneously into the plasma plume from two nozzles separately with optimized velocities of feeding gas, plasma gun and particles. Graded compositions in volume ratios of the FG tungsten/EUROFER layer were realized layer by layer by controlling those velocities. The deposition rate was up to 0.5 kg/min. The sketch of plasma gun movement is shown in Figure 3.5.

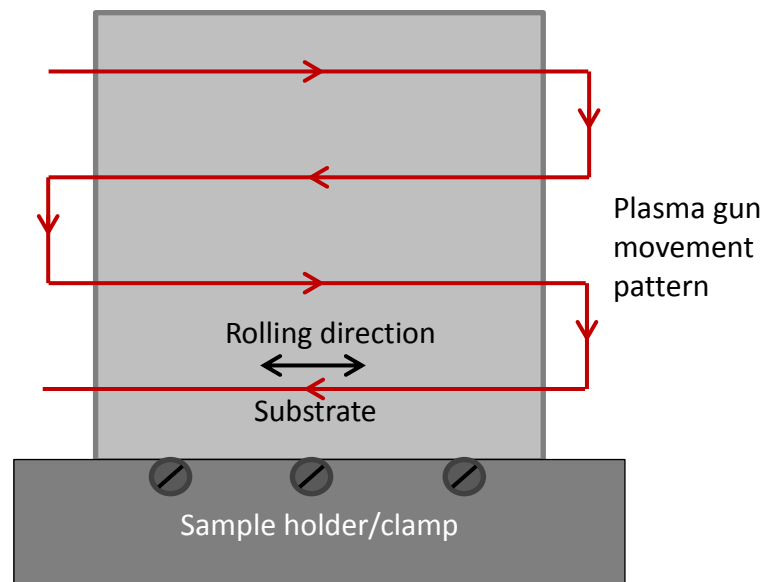


Figure 3.5: The sketch of plasma gun movement.

(2) Roughness and topography

A contact profilometer was used to measure the surface's profile and to quantify its roughness. The contact profilometer is used widely due to its advantages of surface independence and high resolution. A diamond or carbon tip moved vertically in contact with the surface of a sample and then moved laterally across the sample for a specified distance and specified contact force. A typical contact profilometer can measure small vertical features ranging in height from 10 nanometers to 1 millimeter. The HOMMELWERKE TKLT 300/17 profilometer shown in Figure 3.6 is used for measuring the roughness of as-received samples' surface. Thereby a carbon tip with a radius of 5 μm was applied.

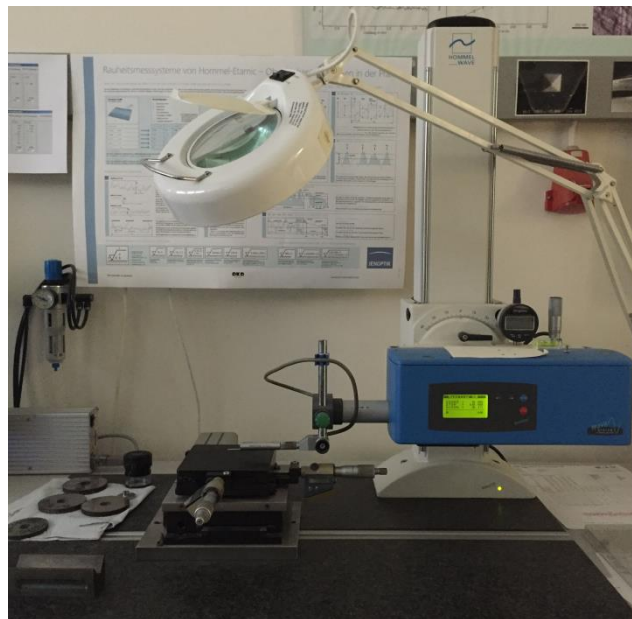


Figure 3.6: The photograph of a profilometer.

To measure the topography of the as-received samples an optical device by the company Fries Research & Technology was used. A broadband “white light” source is used to illuminate the test and reference surfaces. A condenser lens collimates the light from the broadband light source. A beam splitter separates the light into reference and measurement beams. The reference beam is reflected by the reference mirror, while the measurement beam is reflected or scattered from the test surface. The returning beams are relayed by the beam splitter to the charge-coupled devices (CCD) image sensor, and form an interference pattern of the test surface topography that is spatially sampled by the individual CCD pixels.

The short coherence length of the light source results in spatially restricted interference patterns where the magnitude decreases from the center to the left and right. The big advantage of this specific pattern is that its center of gravity can be directly and precisely assigned to a z-height within the object. Hence, exact topography measurements are

possible. A detailed analysis of the interference pattern enables resolutions of a few nanometers. The height information is obtained by vertical scanning, i.e., stepwise moving of the sensor head and taking an image at each step. The images are combined to the final image of the object.

3.1.3 Qualification of the FG W/EUROFER coating system

The microstructure and thermo-mechanical properties of FG W/EUROFER coating system were characterized and assessed for FW application in fusion reactor. The assessments included ELMs-like transient thermal shock and thermal fatigue loadings. Systematic experimental investigations were carried out to characterize VPS FG W/EUROFER coating system.

The microstructural investigations were performed on the as-received surface, polished surface and polished cross-section by several methods including optical microscopy (OM), scanning electron microscopy (SEM), Auger electron spectroscopy (AES) and electron backscattered diffraction (EBSD). Microstructural characterizations including grain size and porosity, gradient and thickness of FG-layer, et al. were investigated.

Nano and Vickers hardness, three and four-point bending test were carried out to evaluate mechanical properties and interface toughness. ELMs-like transient thermal shock and thermal fatigue test were performed to investigate high thermal load resistance of FG W/EUROFER coating system.

3.2. Microstructural analysis

3.2.1 Optical microscope

The optical microscope (OM), often referred to as "light microscope", is a type of microscope which uses visible light and a system of lenses to magnify images of samples. In this work, the OM NIKON ECLIPSE LV150N serves for: (a) determining the thicknesses of tungsten coating and each visible layer of the FG-layer; (b) measuring the dimensions of indentations and cracks; (c) assessing the surface quality after grinding and polishing.

The cross-section of the specimen has the characteristic of the thin coating with a high hardness and the thick EUROFER substrate with a relatively low hardness. Due to this characteristic, it is difficult to prepare a metallographic specimen. Except proper grinding and polishing the embedding material Durocit by Struers company was used for mounting instead of epoxy due to its high hardness and pore-free during solidification. The sample preparation process is summarized in the Table 3.5.

Table 3.5: Parameters of grinding and polishing for W/EUROFER coating system

Method	Grind/Polishing materials	Abrasive size (μm)	Rotation speed/min	Process time
Grinding	SiC paper	25 (600 grit)	150	1 min
		15 (1200 grit)	150	1 min
		10 (2500 grit)	150	1 min
		5 (4000 grit)	150	1 min
Polishing	Diamond	3	80	20 s
	suspension	1	80	20 s
	SiO	0.06	20	2 h

3.2.2 Scanning electron microscopy

Scanning electron microscope (SEM) was used to observe the areas of interest with high magnification by interacting of a focused beam of electrons with samples. In this work, a Philips XL30 field emission SEM was employed. It provides secondary electron and backscattered electron imaging, as well as an energy dispersive X-ray analysis (EDX) system. Surface morphology and phase composite can be analyzed from the secondary electron and backscattered electron images. In addition, the chemical composition of a certain area can be obtained by conducting EDX. An electron beam voltage of 20 kV and working distance of 10 mm were chosen for SEM and EDX observation. Sample preparation for SEM was the same as that for the OM.

3.2.3 Auger electron spectroscopy

Auger electron spectroscopy (AES) is a common surface analytical technique in material science. AES is used to determine the elemental composition and, in many cases, the chemical state of the atoms on the surface of a solid. The method is based on the Auger effect, and the forming states of the Auger electron are showed in Figure 3.7. When an atom is probed by a photon or a beam of electrons with energies in the range of several eV to 50 keV, a core state electron can be removed leaving behind a hole. The core hole can be filled by an outer shell electron, whereby the electron moving to the inner shell loses an amount of energy equal to the difference in orbital energies. The transition energy can be coupled to a second outer shell electron, which will be emitted from the atom and is called Auger electron [82]. Even the energy can also be emitted by x-ray emission, the Auger emission is more likely than x-ray emission for lighter elements.

Because of the relatively low kinetic energy of the Auger electrons they can only escape from the uppermost few monolayers of a surface [83].

In this work, a PHI 680 Xi Field Emission Scanning Auger Nanoprobe was applied. The electron beam with an accelerating voltage of 10 keV and beam size of 40 nm was used to probe the investigated surface. Ar ion beam with accelerating voltage of 26 eV and the etch area of $2 \times 2 \text{ mm}^2$ was used for sputter etching.

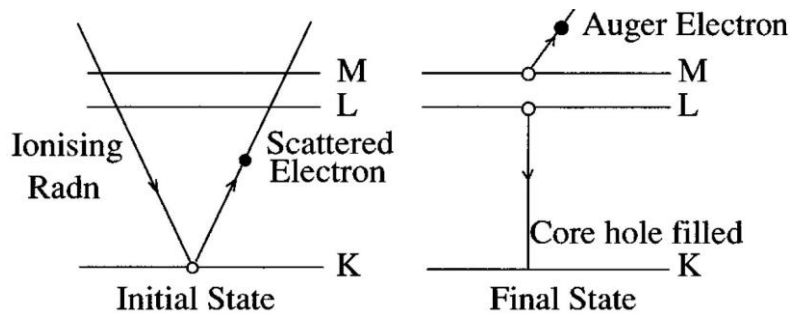


Figure 3.7: Forming stages of the Auger electron [82].

3.2.4 Electron backscatter diffraction

Electron backscattered diffraction (EBSD) is based on the acquisition of diffraction patterns from bulk samples in the scanning electron microscope. EBSD provides versatility in mapping orientation, crystal type, and perfection over a wide range of step sizes, which make it a powerful microstructural characterization tool. Figure 3.8 shows the basic requirement: a scanning electron microscope and an EBSD system. EBSD acquisition hardware generally comprises a sensitive CCD camera, and an image processing system for pattern averaging and background subtraction. The EBSD acquisition software will control the data acquisition, solve the diffraction patterns and store the data. Further software is required to analyze, manipulate and display the data. The basic principle is as the following: an electron beam is focused on a 70° tilted sample, then, electron backscatter diffraction patterns consisted of a set of Kikuchi bands are formed on a phosphor screen. Patterns are transferred from the camera to the computer for indexing and determination of crystal orientation, briefly, the crystal orientation can be determined by acknowledging the position and width of a certain number of Kikuchi bands.

Experimental settings for EBSD were as following: The control and process software was CHANNEL 5 by HKL Technology. The step size varied from 70 nm to $1 \mu\text{m}$ was set to be ~ 10 times smaller than predicted grain diameter of the investigated sample. The sample preparation process was the same as in Table 3.5.

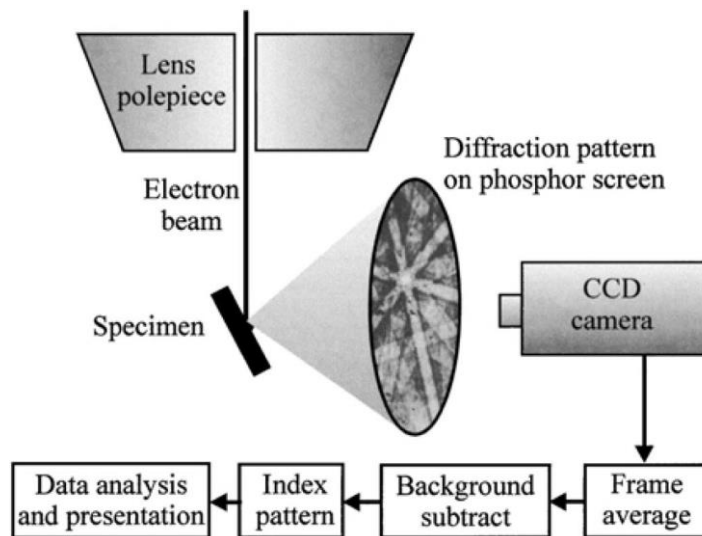


Figure 3.8: Schematic diagram of a typical EBSD installation [84].

3.3. Mechanical investigation

3.3.1 Hardness

3.3.1.1 Nanoindentation

(1) Basic principle

The method was introduced in 1992 for measuring hardness and elastic modulus by instrumented indentation techniques, and has been widely adopted and used in the characterization of small-scale mechanical behavior [85-87]. Comparing to macro- and micro-indentation tests, nanoindentation improves upon indenting on the nanoscale with a very precise tip shape and high spatial resolutions, as well as upon providing real-time load-displacement (into the surface) data when the indentation is in progress. A record of the load and penetration depth can be plotted on a graph to create a load-displacement curve, as showed in Figure 3.9 (b). The parameter P and h shown in Figure 3.9 (a) designate the load and the displacement, respectively. Deformation during loading is assumed to be both elastic and plastic in nature as the permanent hardness impression forms, and it is assumed that only the elastic displacements are recovered during unloading.

There are three important quantities that can be determined from the P - h curves: The maximum load, P_{max} , the maximum displacement, h_{max} , and the elastic unloading stiffness, $S = dP/dh$. S denotes the contact stiffness and is defined as the slope of the upper portion of the unloading curve during the initial stages of unloading.

The exact procedure used to measure hardness and modulus is based on the unloading process shown schematically in Figure 3.9 (a). It is assumed that the behavior of the Berkovich indenter can be modeled by a conical indenter with a half-included angle, Φ , that gives the same depth-to-area relationship, $\Phi=70.3^\circ$. Assuming that pile-up is negligible, the elastic models show that the amount of sink-in, h_s is given by equation (3.2),

$$h_s = \epsilon \frac{F_{max}}{S} \quad (3.2)$$

$$h_c = h_{max} - h_s = h_{max} - \epsilon \frac{F_{max}}{S} \quad (3.3)$$

Where ϵ is a constant value that depends on the geometry of the indenter. h_c is the vertical distance along which the contact is made (hereafter called the contact depth) and h_s is the displacement of the surface at the perimeter of the contact. At the peak load, the load and displacement are F_{max} and h_{max} respectively, and the radius of the contact circle is a . Upon unloading, the elastic displacements are recovered, and the final depth of the residual hardness impression is h_f when the indenter is fully withdrawn.

An ‘‘area function’’ A describes the projected area of the indenter at a distance d back from its tip, and it is a function of h_c . The area function must be calibrated carefully to consider non-ideal indenter geometry. After the contact area is determined, hardness can be calculated from equation (3.4),

$$H_{Berk} = \frac{F_{max}}{A} \quad (3.4)$$

where F_{max} refers to the maximum load. A means projected contact area between indenter and sample, and it can be described by the area function as shown in equation (3.5).

$$A = \sum_{i=0}^8 C_i h_c^{2^{1-i}} = C_0 h_c^2 + C_1 h_c + C_2 h_c^{1/2} + \dots + C_8 h_c^{1/128} \quad (3.5)$$

where C_0 to C_8 are constants without physical significance determined by curve fitting procedures over a given range of depths. Their values are dependent on the tip condition. A perfect Berkovich tip has only one constant, which is $C_0 = 24.5$. h_c is determined according to equation (3.3).

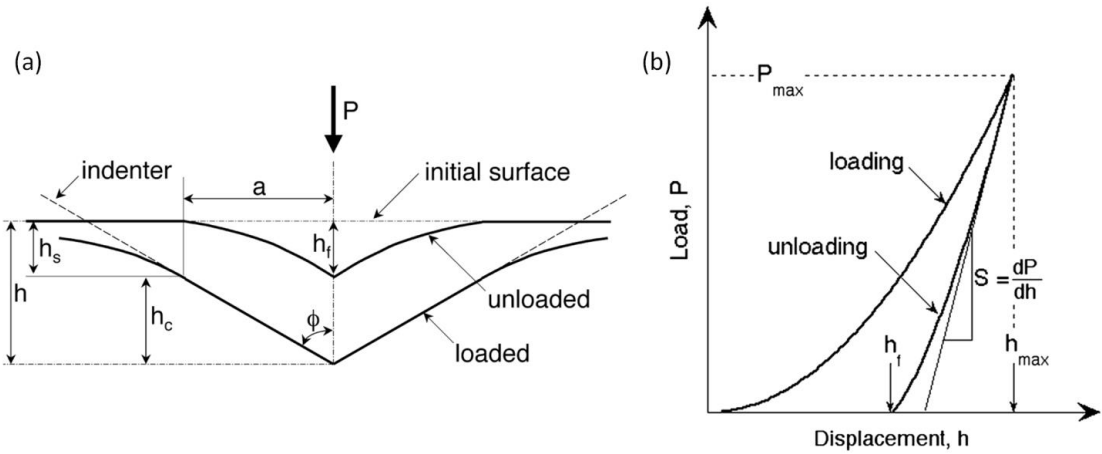


Figure 3.9: A cross section of an indentation (a) and load-displacement curve (b) [86].

Measurement of the elastic modulus follows from the relationship between the contact area and the measured unloading stiffness,

$$S = \beta \frac{2}{\sqrt{\pi}} E_{eff} \sqrt{A} \quad (3.6)$$

where β is a constant that refers to deviation in S and accounts for any physical processes. E_{eff} is the effective elastic modulus defined by

$$\frac{1}{E_{eff}} = \frac{1-\vartheta^2}{E} + \frac{1-\vartheta_i^2}{E_i} \quad (3.7)$$

The effective elastic modulus takes into account the fact that elastic displacements occur in both the specimen, with Young's modulus E and Poisson's ratio ϑ , and the indenter, with the elastic constants E_i and ϑ_i .

(2) Technique parameters and sample fabrication

In this work, G200 (Agilent Technologies) was employed to perform nanoindentation. Berkovich tip was used as indenter, which is a triangle-based pyramid made of diamond. Fused quartz was employed as the reference sample to calibrate the area function of the Berkovich tip. All measurements were conducted under continuous stiffness mode (CSM). The homologous temperature was kept at 26 °C during the measurement. Specimens grinding and polishing steps are described in Table 3.5. Mounting material was removed by heating to 125 °C for 20 min to avoid the effect on the stiffness. Afterwards the specimen was glued on an alumina sample holder for testing.

CSM is one of the most popular methods, and was applied in the work. It has the following advantages: (a) it has a clear advantage of providing continuous results as a function of depth; (b) the time required for calibration and testing procedures is dramatically reduced because there is no need for multiple indentations or unloading; (c) at

high frequencies, CSM allows one to avoid some of the complicating effects of time-dependent plasticity and thermal drift, which cause so much consternation in the original calibration method; (d) the CSM technique allows one to measure the effects of stiffness changes as well as damping changes at the point of initial contact.

Using CSM technique to acquire hardness and elastic modulus as a continuous function of penetration into the test surface, a constant strain rate target equal to 0.15 1/s was used, and frequency target, harmonic displacement target, and maximum penetration depth were specified to be 45 Hz, 2 nm and 2000 nm, respectively. Specifically, 5 or 10 indentations should be made on quartz for tip calibration. Then the calibrated tip was used to analyze the indentation data. The hardness and modulus in the depth range of 1800 -2000 nm were calculated and summarized in the work.

3.3.1.2 Vickers hardness

The Vickers hardness test method, also referred to as a microhardness test method, is widely used in materials mechanical characterization. Vickers hardness specifies a range of light loads using a square base pyramid-shaped diamond indenter with an apical angle of 136° to make an indentation, and then the indentation is measured and converted to a hardness value.

Vickers hardness tests were conducted on a Zwick machine. Several load HV0.2 (1.96 N), HV0.5 (4.9 N), HV1 (9.8 N), HV2 (19.6 N) and HV5 (49 N) were applied on each layer of the coating system for determining the suitable load. The suitable load was evaluated by the dimension of the indentations introduced by this load. The indentation should cover as large area as possible but not exceed the investigated layer. HV₁ (9.8 N) was chosen as the investigated load since the diameter of indentations introduced by the load was in a range of ≈ 65 μm (pure tungsten coating) to ≈ 88 μm (W25% coating of FG-layer), and it was less than the thinnest FG-layer with the thickness of ≈ 120 μm. All investigated surfaces were polished to 0.06 μm prior to the indentation testing, and 10 indentations were done for each layer. To avoid the influence from work-hardening induced by other indentations, the distance between each two indentations was kept 3 times of the indentation diagonal dimension. The determination of Vickers hardness is given by equation 3.8:

$$HV = \frac{1}{g} \frac{F_{max}}{A} = \frac{1}{g} \frac{F_{max}}{4S} = \frac{1}{g} \frac{2F_{max} \sin \frac{\alpha}{2}}{d^2} = 0.1891 \frac{F_{max}}{d^2} \quad (3.8)$$

where A refers to the whole area of indentation, S is the area from one of the four cones, F_{max} is the maximum force in N , and g is the gravitational acceleration (equal to 9.8).

3.3.2 Thermal load tests

3.3.2.1 ELMs-like thermal shock tests

The electron beam facility JUDITH 1 from FZJ was used to perform thermal shock tests on the FG W/EUROFER coating systems in the work. It is capable of simulating fusion relevant steady-state heat loads as well as transient events such as ELMs, VDEs and plasma disruptions. A schematic overview and a photograph of JUDITH 1 are shown in Figure 3.10. JUDITH 1 consists of a modified electron beam gun with a power of 60 kW, a vacuum chamber with the dimensions of $800 \times 600 \times 900 \text{ mm}^3$ and several diagnostic devices, such as an infrared pyrometer, two color pyrometers, fast pyrometers, thermocouples, as well as infrared and visual cameras. The electron beam is generated with a tungsten cathode that emits free electrons [88].

In JUDITH 1 a homogeneous heat load distribution with the $4 \times 4 \text{ mm}^2$ beam spot is achieved by a triangular scanning of the Gaussian shaped 1mm wide electron beam (31/40 kHz). All five samples were cut into $50 \text{ mm} \times 10 \text{ mm}$ of the length and the width, and then top surfaces are grinded to a mirror finish to create an undamaged well-defined starting state. The samples were loaded at ELMs-like relevant power densities of 0.19 and 0.38 GW m^{-2} . The power densities were calculated by taking an electron absorption coefficient of 0.46 into account. The exposed area was scanned with a focused electron beam (diameter of ca. 1 mm) at very high scanning frequencies (47 kHz in the x-direction and 43 kHz in the y-direction), single pulse duration of 1 ms and a total number of 100 pulses were kept constant for all samples. The loading frequency was ca. 0.5 Hz to allow a complete cooling down after each individual pulse. In addition to tests performed at room temperature (RT), a graphite holder with a tubular heating cartridge was used to achieve base temperatures up to $550 \text{ }^\circ\text{C}$ [40].

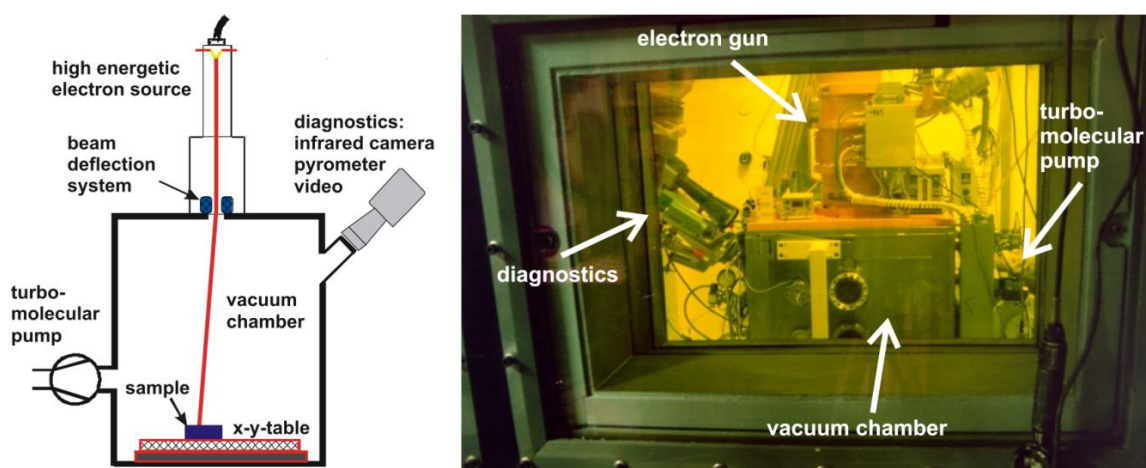


Figure 3.10: Left: the schematic view of the electron beam facility JUDITH 1 with diagnostic systems. A thermal shock sample is mounted on a XYZ-table and scanned by the electron beam. Right: photograph of JUDITH 1 located in the hot cells [88].

The induced thermal shock damages were investigated by SEM, OM, as well as focused ion beam (FIB) for cutting into certain interesting cracks. To quantify the surface morphology (roughening and cracks), erosion and redeposition, a profilometer with a confocal sensor (KF3 by OPM GmbH) was used. The sensor is able to determine the vertical position of the surface with a precision up to 0.02 μm . Line scans or 3D-surface profiles can be recorded using a rapid stage positioning system (up to 10 mm/s); the maximum measurement frequency is 1 kHz. The maximum travel distance of the stage positioning system is limited to 50 and 100 mm in x- and y-direction, respectively. The maximum measurement range in the z-direction is 1 mm. Besides quantitative analyzes on the materials' erosion during intense transient thermal loads, the system is qualified to measure the roughness and micro-morphological characteristics of polished samples' surfaces before and after thermal load tests. This makes it possible to determine the kind of surface damage/modification induced by transient or steady state heat loads. The profilometry gives a value of the surface roughness and enables to classify and compare the results in dependence on the materials and testing conditions.

3.3.2.2 Thermal fatigue tests

As shown in Table 1.1 of Section 1, designed number of normal operation cycles for FW of ITER and DEMO are 30000 and < 1000 , respectively. Therefore, the performance of the coating system under cyclic operation condition is important. The non-homogenous temperature field under thermal-mechanical loads of helium cooled pebble bed-test blanket module (HCPB-TBM) has been observed and concluded in [89]. The temperature varies between a minimum of 300 $^{\circ}\text{C}$ at the inlet pipe for the coolant and a maximum of 572 $^{\circ}\text{C}$ in the plates of the horizontal stiffening grid. The maximum temperature of FW is 535 $^{\circ}\text{C}$, which is below the design limit 550 $^{\circ}\text{C}$ for EUROFER. In the work, 350 $^{\circ}\text{C}$ and 550 $^{\circ}\text{C}$ were chosen respectively as the minimum and maximum temperature of one thermal cycle to simulate thermal fatigue of FW.

To simulate thermal fatigue vacuum furnace was used, as shown in Figure 3.11. Samples with the diameter of 5 mm were placed in the middle of the furnace. Temperature calibration was performed to get a stable and homogeneous temperature field, and two thermocouples were used to measure the upper and bottom temperature of the samples. A stable temperature cycle between 550 $^{\circ}\text{C}$ and 350 $^{\circ}\text{C}$ was observed after the first cycle. Cooling water was used to keep the cooling rate constant. In total 500 thermal cycles were performed, and two samples were taken out after each 100 cycles. OM and SEM were used to observe cracks on the surface and inside the sample, and Vickers hardness was performed to compare mechanical properties after each 100 cycles.

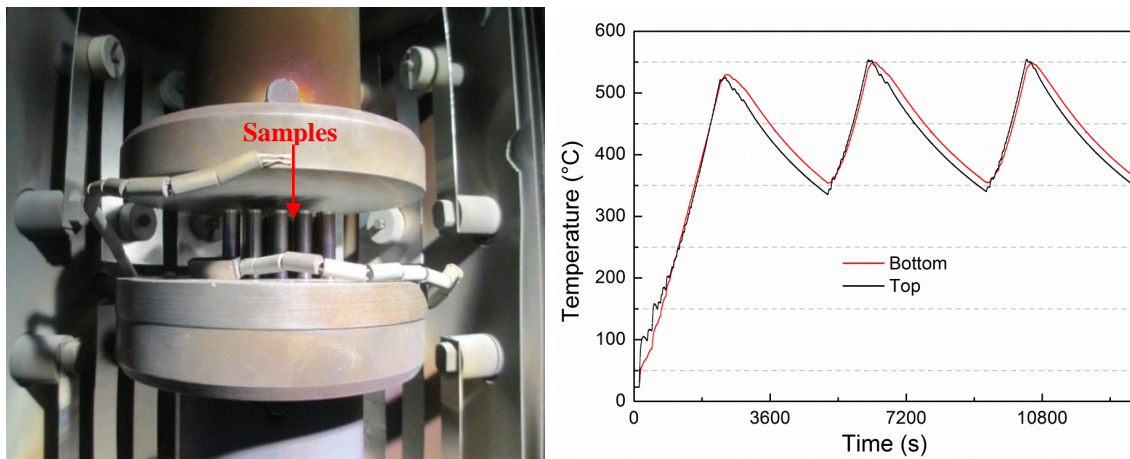


Figure 3.11: Thermal fatigue test. Left: vacuum furnace facility; Right: temperature curve over time.

3.3.3 Interface toughness

Material toughness characterization is one aspect of fracture mechanics. In 1956, Irwin [90] developed the energy release rate concept. It is derived from the Griffith theory but is more useful for solving engineering problems. Around 1960, researchers turned their attentions to crack-tip plasticity when the fundamentals of linear elastic fracture mechanics were fairly well established. Except the crack-tip-opening displacement (CTOD) proposed by Wells, Rice developed J-integral to characterize nonlinear material behavior ahead of a crack [91]. A series of standard methods were established based on the above theory. ASTM E-1820 test method [92] is applied widely for the determination of metallic materials' fracture toughness by using the following parameters: K, J, and CTOD. The fracture toughness determined in accordance with this test method is for the opening mode (Mode I) of loading. Based on the force vs. deflection curves and the crack length as well as specimen geometry for each specimen the J-R curve can be constructed, from which the fracture toughness can be then calculated.

Fracture at interfaces between dissimilar materials is a very common and critical phenomenon in many systems, for example, composites, microelectronic devices and thin films. Interface toughness is a critical assessment of the thermal spraying coating quality and the interfacial bonding strength. Yet both the fundamental mechanics and experimental techniques on interface toughness are seldom reported in literature. In addition, most of the interface fracture problems involve combinations of normal and shear load modes, which are called mixed mode. The phase angle represents the mixed level. It is equal to 0° for pure opening load (mode I), and equal to 90° for pure shear load (mode II).

Charalambides et al. [93] develop a model for determining the fracture resistance of bimaterial interfaces by introducing a bimaterial constant. The constant is a function of the shear modulus and Poisson's ratio of both materials, and then a complex stress inten-

sity factor at position r ahead of the crack tip could be expressed by this constant. The estimated value of the energy release rate (steady-state energy release rate) can be obtained based on the beam theory and plane strain conditions analytically and numerically, and the two values from the two methods fit quite well. In addition, the energy release rate calculated by FE simulation has been assessed by the four-point bending experiment performed on a bimaterial beam specimen with a central notch and a symmetrical pre-crack at the interface. This reliable method could be applied to other material systems, e.g. FG W/EUROFER coating system, only by adjusting the geometry parameter and Young's modulus.

Another model introduced by Phillips et al. is also acceptable. Specifically, they apply beam theory to establish the expression of the roller displacement, and then get the expression of compliance. Since it is equal to displacement divided by load, in the end, they get the expression of strain energy release rate by differentiating the expression of compliance [94]. In addition, the method is also assessed by three-point bending test on a laminated SiC/C composite [95], and is used to calculate the interface toughness of a $\text{Si}_3\text{N}_4/\text{BN}+\text{Si}_3\text{N}_4(\text{BN}+\text{Al}_2\text{O}_3)/\text{Si}_3\text{N}_4$ sandwiched sample [96]. Except three-point and four-point bending test methods, double cantilever beam, double-cleavage drilled compression and indentation method are also widely used for measuring the interface toughness. These methods encompass a range of loading modes, with the phase angle of loading ranging among 0° (e.g. double-cantilever beam) and 90° (e.g. barb test).

In the work, due to the geometry of the coating system, three-point and four-point bending tests were performed to achieve the load vs. deflection curve during crack propagation, and then interface toughness was calculated based on the above models.

3.3.3.1 Method and set-up

Three-point and four-point bending tests were performed at 550°C in a vacuum furnace, and the set-ups are shown in Figure 3.12. It is necessary to calibrate the temperature at the certain position to achieve a stable temperature field at 550°C during the bending test. The deflection was measured and controlled by a transducer.

Figure 3.13 shows the schematic of load and moment for three-point (a) and four-point (b) bending tests. Comparing to three-point bending, four-point bending has an advantage that it can provide a constant moment between the two inner loading points. Normally samples with large size are needed for four-point bending test, and this may restrict the application of four-point bending. Meanwhile, the mechanical strength measured by four-point bending will be lower and much reliable than the one measured by three-point bending.

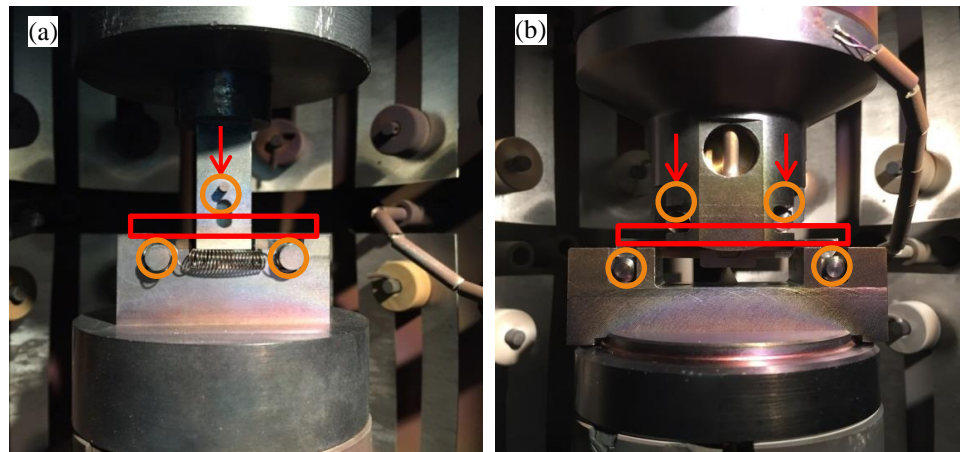


Figure 3.12: Set-ups: (a) three-point bending and (b) four-point bending.

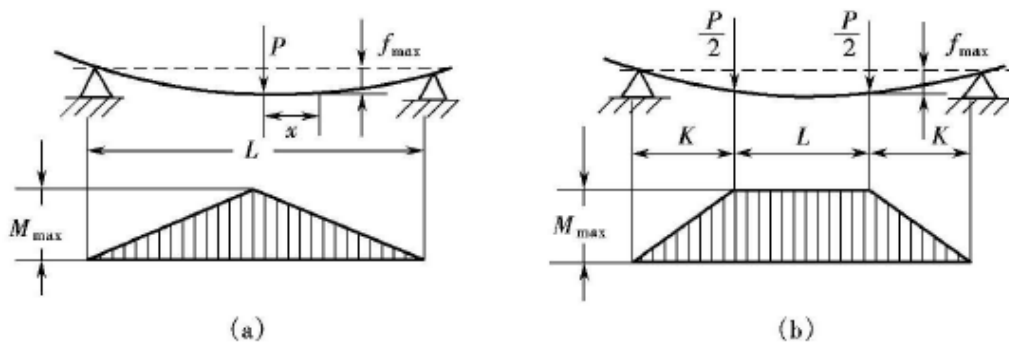


Figure 3.13: Schematic view of load and moment for three-point (a) and four-point (b) bending.

3.3.3.2 Specimen

Single-edge bend sub-size specimen (also called “KLST” specimen) with the dimension of $27 \times 4 \times 3 \text{ mm}^3$ ($L \times W \times B$) was chosen in the work because of the thin coating and the limited dimension. The sample was cut into $27 \times 4 \times 3 \text{ mm}^3$ with 0.5 mm deep notch by electrical discharge machining (EDM) for three-point bending test. Two lateral surfaces were grinded and polished for observing the crack. A through-thickness fatigue pre-crack showed in Figure 3.14 (a) was introduced by resonating fatigue machine.

The specimen was machined into $45 \times 4 \times 3 \text{ mm}^3$ with 0.5 mm deep notch for four-point bending test. Since the resonance fatigue machine could only produce through-thickness pre-crack as shown in Figure 3.14 (a), two methods were attempted for introducing interfacial pre-crack. One method was by performing three-point bending test in a small range of deflection, the other method was to introduce a “T” notch by EDM, as shown in Figure 3.14 (b). However, two methods for introducing interfacial pre-crack were not successful. In the end, the same through-thickness pre-crack as three-point bending was used for four-point bending test.

Lengths of the notch and pre-crack, as well as width and thickness of each specimen were measured before bending tests. For the cases where the lengths of pre-cracks on both sides were not uniform, the mean value was taken for the calculation. For the cases where the pre-crack was only observed on one side, the calculated value was considered to be invalid.

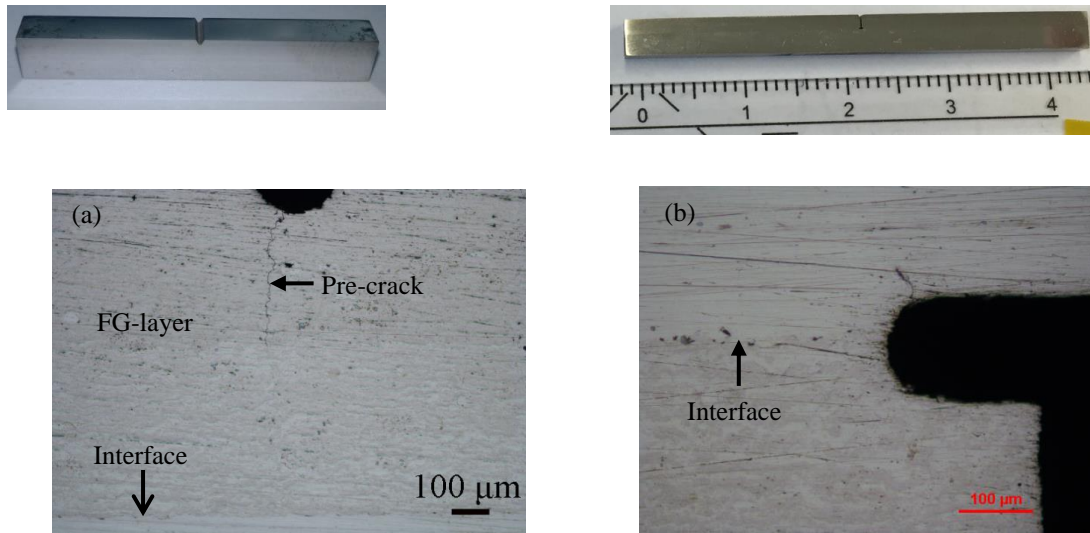


Figure 3.14: (a) Three-point and (b) four-point bending specimen.

3.3.3.3 Experimental principle

Three and four-point bending tests were performed to evaluate the interface toughness of FG W/EUROFER coating system. A schematic view of the beam for bending tests is showed in Figure 3.15. The precrack and the through-thickness cracks are assumed to occur in the center of the beam and the interfacial cracks propagate symmetrically from the center.

For calculating the interface toughness, the Young's modulus and stiffness of the composite beam need to be determined primarily. According to the definitions of the moment of inertia and stiffness, the stiffness of the substrate can be calculated based on the formula (3.9). For determining the stiffness of the whole composite, the moment of inertia for the composite is calculated firstly based on the formula (3.10) and (3.15) from [93]. Then the stiffness of the whole specimen can be calculated according to the formula (3.11) and (3.12). The Young's modulus and the Poisson ratio of the coating system are interpolated linearly according to the properties of the bulk material at 550 °C, and the proportion of each layer is assumed to be related to its thickness, as shown in the formula (3.13) and (3.14).

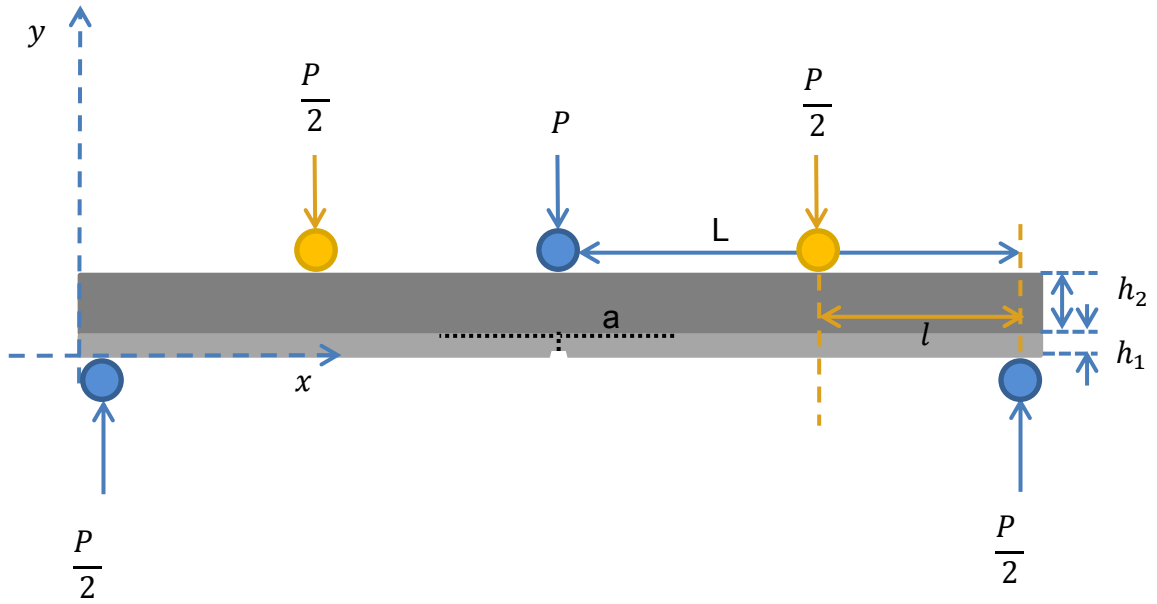


Figure 3.15: Schematic view of the beam for three- and four-point bending test.

$$\Sigma_{Sub} = \frac{Bh_2^3}{12} \times E_{Sub} \quad (3.9)$$

$$I_c = \frac{h_1^3}{12} + \frac{\lambda h_2^3}{12} + \frac{\lambda h_1 h_2 (h_1 + h_2)^2}{4(h_1 + \lambda h_2)} \quad (3.10)$$

$$E_c = \frac{E_1 \times h_1 + E_2 \times h_2}{h} \quad (3.11)$$

$$\Sigma_c = I_c \times B \times E_c \quad (3.12)$$

where

$$E_1 = \frac{E_w \times T_w + E_{w75\%} \times T_{w75\%} + E_{w63\%} \times T_{w63\%} + E_{w50\%} \times T_{w50\%} + E_{w37\%} \times T_{w37\%} + E_{w25\%} \times T_{w25\%}}{T_w + T_{w75\%} + T_{w63\%} + T_{w50\%} + T_{w37\%} + T_{w25\%}} \quad (3.13)$$

$$\vartheta_1 = \frac{\vartheta_w \times T_w + \vartheta_{w75\%} \times T_{w75\%} + \vartheta_{w63\%} \times T_{w63\%} + \vartheta_{w50\%} \times T_{w50\%} + \vartheta_{w37\%} \times T_{w37\%} + \vartheta_{w25\%} \times T_{w25\%}}{T_w + T_{w75\%} + T_{w63\%} + T_{w50\%} + T_{w37\%} + T_{w25\%}} \quad (3.14)$$

$$\lambda = \frac{E_2(1-\vartheta_1^2)}{E_1(1-\vartheta_2^2)} \quad (3.15)$$

$$h = h_1 + h_2 \quad (3.16)$$

E_1 , E_2 and E_c are the Young's modulus of the coating system, the substrate and the whole composite specimen, respectively. ϑ_1 and ϑ_2 are the Poisson ratios of the coating system and the substrate. The material parameter λ is an expression of the Young's modulus and Poisson's ratio of both materials: coating system and substrate. B and h are the width and the thickness of the specimen. h_1 and h_2 are the thicknesses of the

coating system and the substrate, respectively. Σ_{sub} and Σ_c are the stiffness of the substrate and the whole composite specimen. I_c is the moment of inertia for the composite.

3.3.3.3.1 Three-point bending test

The interfacial crack propagation of the composite specimen is separated into two stages. The stage one is defined to be that the crack propagates in the FG-layer, in which the composite beam (both the coating system and the substrate) is assumed to carry the load. The second stage is that crack deflects along the interface, in which only the substrate is assumed to carry the applied load. Therefore, the beam stiffness is set equal to the composite stiffness for the first stage. For the second stage, the beam stiffness is equal to the substrate stiffness.

According to the beam theory, during the first stage, the deflections of the specimen can be evaluated as following formulas since the whole specimen carry the stress:

$$\frac{d^2y_1}{dx^2} = -\frac{Px}{2\Sigma_c} \quad (3.17)$$

For the second stage, only the substrate is assumed to carry the stress:

$$\frac{d^2y_2}{dx^2} = -\frac{Px}{2\Sigma_{sub}} \quad (3.18)$$

where y_1 and y_2 are the deflection of the neutral axis during the first and second stage, respectively. And Σ_c and Σ_{sub} are the stiffness of the whole specimen and the substrate.

The mathematical relation (3.19) between the deflection of the central loading point and the propagating crack length can be obtained taking into account the boundary conditions of the model. The derivational process and the boundary conditions are specified in Appendix C.

$$y = \frac{PL^3}{6\Sigma_{sub}} + \frac{P(L-a)^3}{6} \left(\frac{1}{\Sigma_c} - \frac{1}{\Sigma_{sub}} \right) \quad (3.19)$$

Since the compliance $C_b = \frac{y}{P}$, then

$$C_b = \frac{L^3}{6\Sigma_{sub}} + \frac{1}{6} \left(\frac{1}{\Sigma_c} - \frac{1}{\Sigma_{sub}} \right) (L-a)^3 \quad (3.20)$$

The propagating cracks are assumed to be symmetric on both sides of the central point, the interface toughness can be obtained according to the fracture mechanic expression (3.21):

$$G_c = \frac{P^2}{4b} \frac{dC_b}{da} \quad (3.21)$$

After the differentiation of the formula (3.20), the interface toughness can be expressed as:

$$G_c = -\frac{P^2}{8b} \left(\frac{1}{\varepsilon_c} - \frac{1}{\varepsilon_{sub}} \right) (a - L)^2 \quad (3.22)$$

3.3.3.3.2 Four-point bending based on Charalambides Model

The specimen is subjected to a constant moment condition when the crack located between the inner loading lines during four-point bending test. Therefore, the strain energy release rate should exhibit steady-state characteristics. “The steady-state value, G_{SS} , has been deduced analytically by recognizing that it is simply the difference in the strain energy in the uncracked and cracked beam.” Then the strain energy release rate can be expressed with the formula (3.23), which is deduced from Euler-Bernoulli beam theory and plane strain conditions [93]. As shown in Figure 3.16, the steady-state value G_{SS} increases with the thickness ratio, and it decreases over the material parameter λ . The dotted lines are the analytical and finite element results by Charalambides et al. [93]. As it can be seen, the two results fit very well, what proves the analytical model reliable. Applying the model to FG W/EUROFER coating system, the energy release rate as a function of the thickness ratio is plotted in Figure 3.16 for sample 3-T(7) with the certain λ . Four-point bending tests were performed to determine the critical load during the propagation of the interfacial crack,

$$\frac{E_2 G_{SS} h^3 B^2}{P^2 l^2 (1 - \theta_2^2)} = \frac{3}{2} \left\{ \frac{1}{\left(\frac{h_2}{h}\right)^3} - \frac{\lambda}{\left(\frac{h_1}{h}\right)^3 + \lambda \left(\frac{h_2}{h}\right)^3 + 3\lambda \left(\frac{h_1 h_2}{h^2}\right) \left(\frac{h_1}{h} + \frac{\lambda h_2}{h}\right)^{-1}} \right\} \quad (3.23)$$

where G_{SS} is the steady-state energy release rate, P_c is the load for the propagation of the interfacial crack, l is the distance between inner and outer load lines.

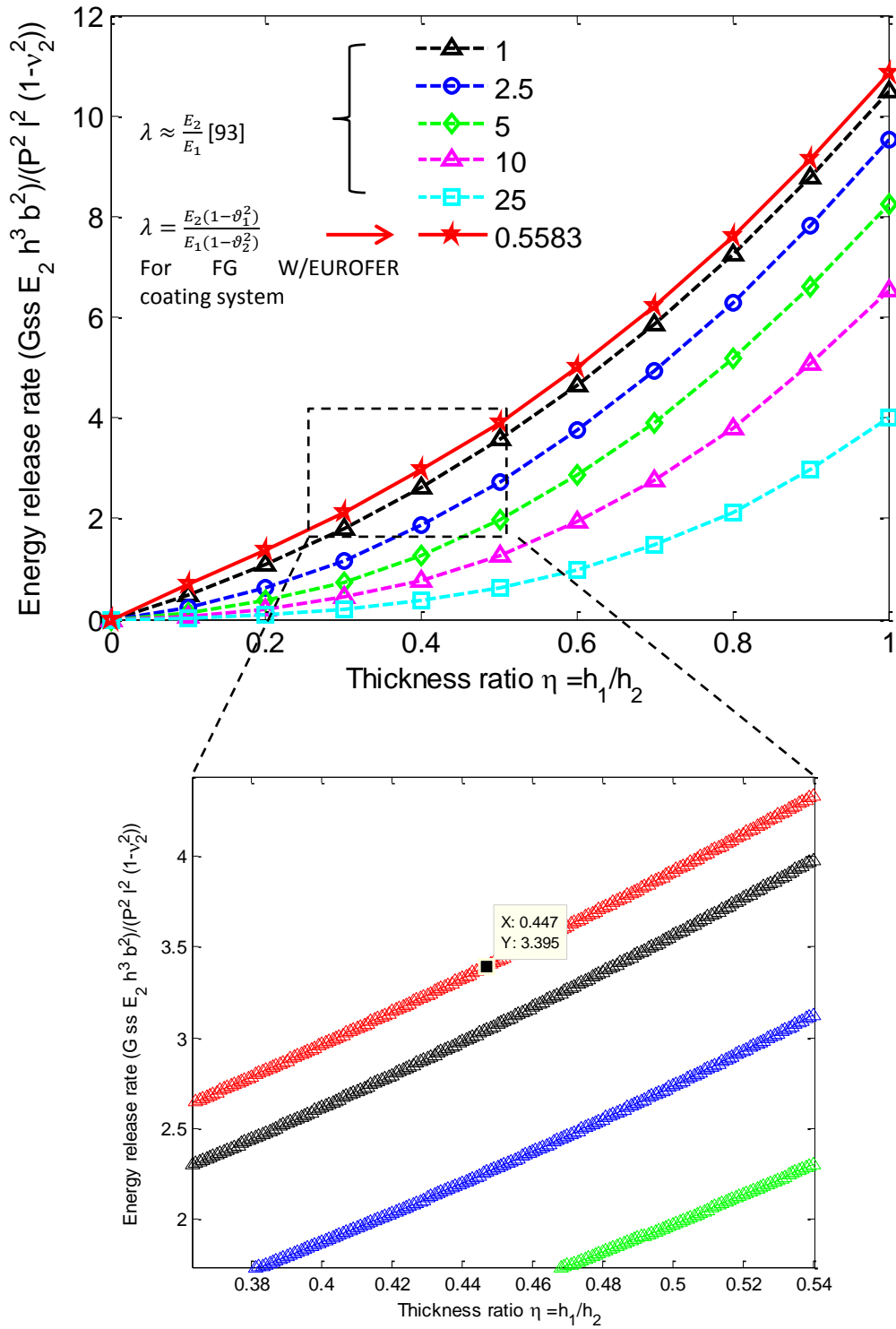


Figure 3.16: The steady-state energy release rate as a function of the thickness ratio and material parameter λ calculated for FG W/EUROFER coating system according to [93].

4 Results and discussion

In the chapter the FG-layer thickness was determined and specified for fabrication by performing FE-simulation. Five VPS produced FG W/EUROFER coating systems were investigated including their microstructural and thermo-mechanical properties. Their interface toughness and thermal load resistance were evaluated as FW application.

4.1. FE simulation

4.1.1 Simulation of the cooling down phase

Figure 4.1 (a) shows von Mises stress distribution of the FE-model with 0.5 mm thick FG-layer. The maximum von Mises stress occurs in tungsten, which is limited by the yield stress of tungsten. Then it reduces gradually from tungsten to EUROFER substrate. In addition, the principal stress σ_{11} along the dashed path (in Figure 4.1 (a)) is shown in Figure 4.1 (b). The stress in tungsten coating is compressive, and it stays nearly constant for both FE-models with elastic (E) and elastic-plastic (E+P) material behavior, respectively. Since W is a brittle material, the compressive stress do not induce damage even if it is equal to the yield stress of tungsten. The absolute value of the stress decreases gradually and becomes tensile in the FG-layer. The stress in EUROFER is tensile until about 13 mm from the interface, and then it becomes compressive again. The induced tensile stress in EUROFER is lower than its yield stress given in Table 3.1.

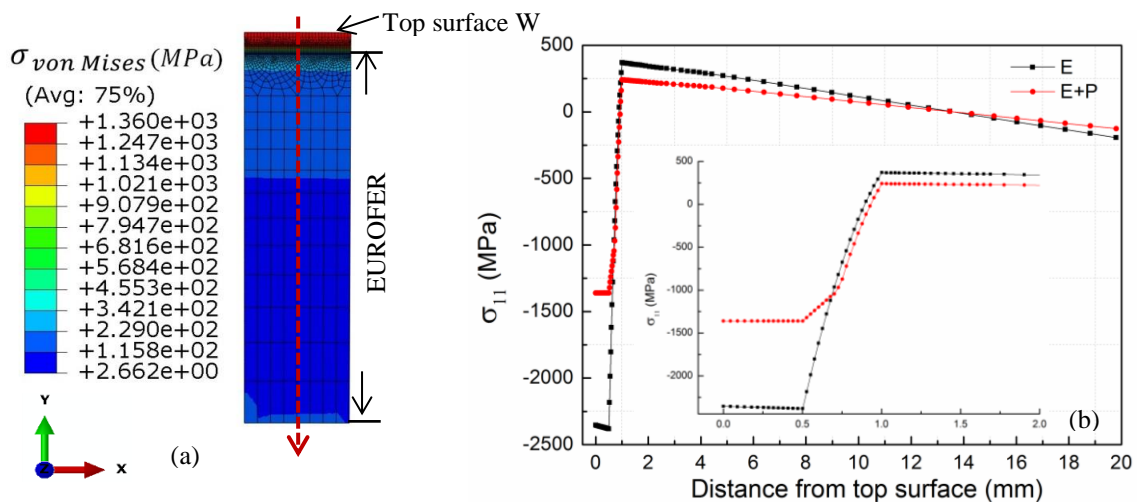


Figure 4.1: (a) von Mises stress distribution and (b) distribution of principal stress σ_{11} of the FE-model with 0.5 mm thick FG-layer.

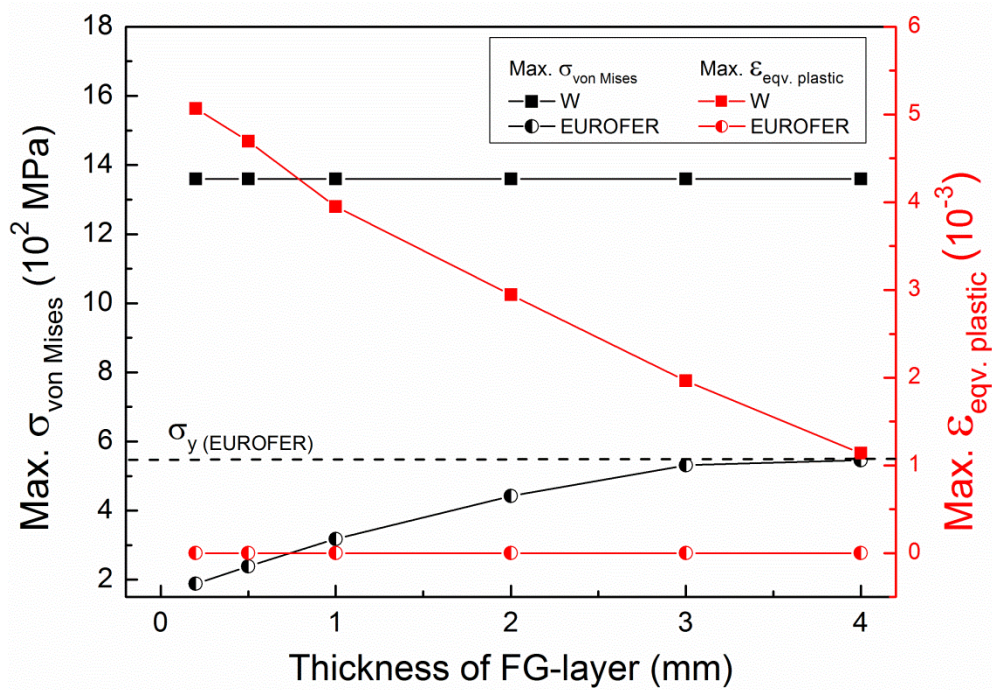


Figure 4.2: Maximum von Mises stress and maximum equivalent plastic strain versus thickness of FG-layer.

Figure 4.2 shows the maximum von Mises stress and equivalent plastic strain as a function of FG-layer thickness in both W and EUROFER. The maximum equivalent plastic strain in tungsten decreases with increasing thickness of FG-layer while that in EUROFER is equal to 0 for all investigated thicknesses. Maximum von Mises stress in EUROFER slightly increases with increasing thickness of FG-layer, but it is not high enough to cause plastic deformation when the FG-layer thickness is thinner than 4 mm. In addition, maximum von Mises stress in EUROFER is limited by the yield stress for 4 mm thick FG-layer. Therefore, considering the further fabrication the maximum thickness of FG-layer is determined to be 4 mm since plastic deformation induced by tensile stress in EUROFER is very damaging during thermal cyclic operation phase of FW.

4.1.2 Simulation of the operation phase

Figure 4.3 (a) illustrates the dependence of maximum equivalent creep strain after 365 cycles with the hold time of 365×24 h on FG-layer thickness. The equivalent creep strain decreases drastically with increasing thickness of FG-layer. When the FG-layer thickness is greater than or equal to 1.2 mm, the equivalent creep strain is less than 10^{-5} after 365 thermal cycles.

As it can be seen in Figure 4.3 (b), maximum equivalent creep strain of FE-models with all investigated thicknesses increases with thermal cycles, but the thicker the FGM, the smaller the creep strain. Particularly for FG-layer thicker than 0.7 mm a sharp fall is observed. In addition, maximum equivalent creep strain becomes small and constant

versus the number of cycles for FG-layer thicker than 1.0 mm. Maximum equivalent creep strain is less than 10^{-5} and independent on number of cycles when the FG-layer thickness is greater than or equal to 1.2 mm.

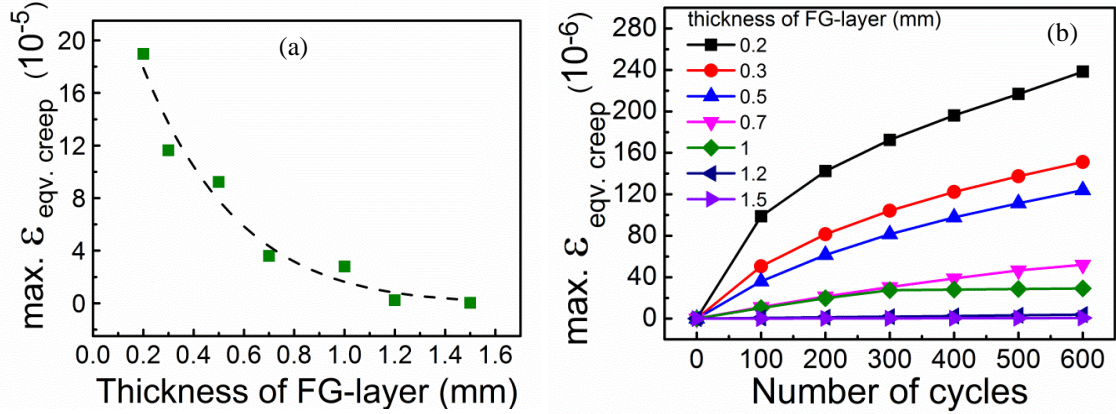


Figure 4.3: (a) The dependence of max. equivalent creep strain after 365 cycles on thickness of FG-layer, and (b) Max. equivalent creep strain versus the number of cycles for all investigated thicknesses.

4.1.3 Creep lifetime evaluation of EUROFER

In the RCC-MR codes, the stress-to-rupture curves [97] are derived from lifetime data of creep tests. The minimum stress value S_r which yields to rupture at the given temperature θ after the given time T_d (design time) is deduced as the following equation:

$$S_r = 1936 - 88.452P + 0.888324P^2 \quad (4.1)$$

where

$$P = (30 + \log(T_d))(\theta + 273)/1000 \quad (4.2)$$

To obtain the allowable stress S_d , the minimum stress S_r is divided by a safety factor k which is specified as constant for all materials and equal to 0.9 in RCC-MR codes [89]. The derived design criteria [98] is then given by the equation:

$$S_d = 0.9(1936 - 88.452P + 0.888324P^2) \quad (4.3)$$

The equations 4.2 and 4.3 can be used for calculating the allowable design time T_d for a given stress, while in the general multiaxial loading case the equivalent stress σ_e is considered. σ_e is calculated by the equation (4.4) based on the results of inelastic stress analysis, e.g. performing proper non-linear FE simulation:

$$\sigma_e = 0.867\bar{\sigma} + 0.133J_1 \quad (4.4)$$

where

$$J_1 = \sigma_1 + \sigma_2 + \sigma_3 \quad (4.5)$$

$$\bar{\sigma} = \frac{1}{\sqrt{2}} [(\sigma_1 - \sigma_2)^2 + (\sigma_2 - \sigma_3)^2 + (\sigma_1 - \sigma_3)^2]^{1/2} \quad (4.6)$$

with σ_1 , σ_2 and σ_3 denoting the principal stresses.

The creep damage of one cycle is calculated according to the linear damage accumulation as shown in the equation (4.7):

$$D_{Cr} = \sum_{i=1}^j \frac{\Delta t_i}{T_d(\sigma_{e,i})} \quad (4.7)$$

With j denoting the number of time intervals, in which the hold time of the considered cycle is subdivided. In each time interval i with the duration Δt_i the equivalent stress $\sigma_{e,i}$ is considered constant. $T_d(\sigma_{e,i})$ is the allowable design time for the equivalent stress $\sigma_{e,i}$, and it is determined by solving equation 4.2, as mentioned above. To obtain the maximum creep damage per cycle one interval with the duration of the hold time and the equivalent stress at the beginning of the hold time is considered ignoring its relaxation during the hold time. Figure 4.4 shows creep damage per cycle versus number of cycles for all investigated thicknesses of FG-layer. Creep damage per cycle decreases with the increasing number of cycles, especially for the FE-models with FG-layer thinner than 0.7 mm. For the FE-models with FG-layer thickness greater than or equal to 0.7 mm, the creep damage of each cycle is more or less constant. Considering the decreasing creep damage with cycle number, the allowable number of cycles determined in [99] is too conservative. The sufficient conservative N_{Cr} is determined as following:

$$N_{Cr} = 600 + \frac{1 - \sum_{600} D_{Cr}}{D_{Cr}^{600}} \quad (4.8)$$

Figure 4.5 shows the allowable number of cycles for EUROFER versus the FG-layer thickness. The allowable number of cycles N_{Cr} increases proportionally to thickness for the FE-models with FG-layer thinner than 1.0 mm, while it increases similarly over half order of magnitude for the FE-models with 1.2 and 1.5 mm thick FG-layer.

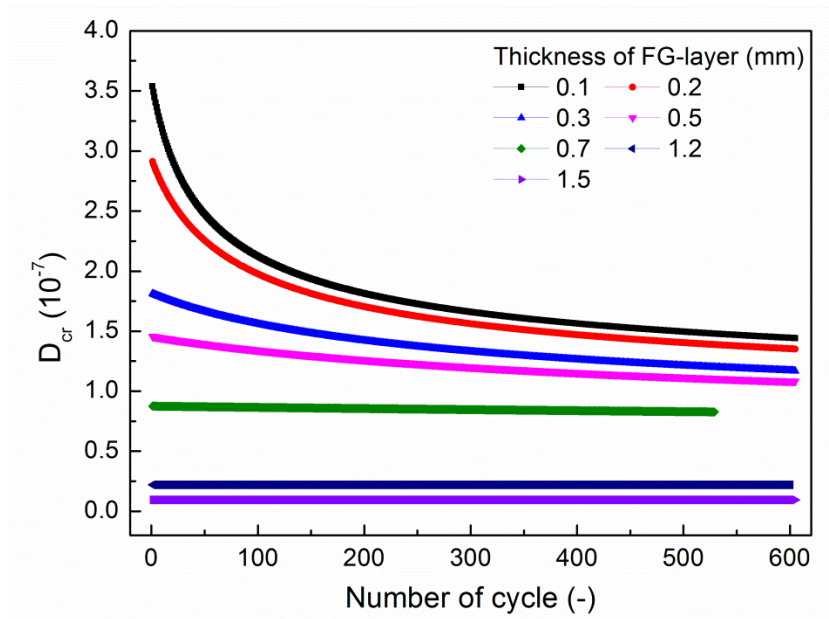


Figure 4.4: Creep damage per cycle versus number of cycles for all investigated thicknesses of FG-layer.

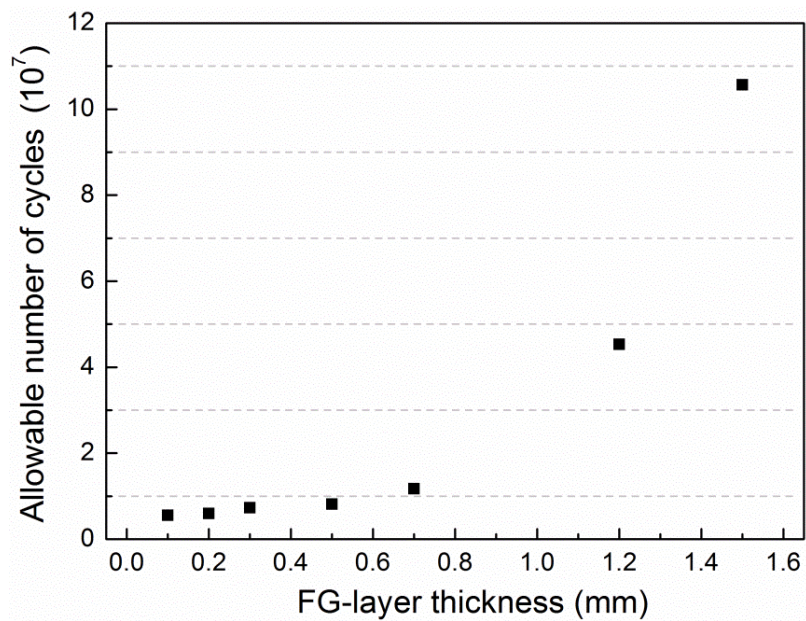


Figure 4.5: Allowable number of cycles for EUROFER versus the FG-layer thickness.

4.1.4 Discussion and conclusion

For the fabrication phase, the gradient CTE in FGM releases residual stresses in the coating system which can be seen from the dependence of the maximum von Mises stress and equivalent plastic strain on FG-layer thicknesses. Even though it shows that the thicker thickness the less residual stress in tungsten, the slight increase of residual stresses in EUROFER should be noticed. Therefore the maximum thickness should be less than 4 mm due to the plastic deformation induced by the tensile residual stress in EUROFER based on the simulation results of cooling down process.

Considering the operation phase, equivalent creep strain is analyzed for the assessment of thicknesses since the von Mises stress is not suitable when the material behavior includes plasticity and creep. The applied FGM reduce residual stresses and creep strains, respectively. It is clear that the thicker the FG-layer the better for the reduction of creep strain. While for FG-layer thickness greater than or equal to 1.2 mm the maximum creep strain becomes negligibly small and independent on number of cycles. Moreover, the allowable number of cycles increases remarkably. Therefore, the sufficient thickness is 1.2 mm based on the simulation results of the operation process.

FE-simulation results show that the best thickness of FG-layer is among 1.2 - 4 mm, however, the spalling off coating from the WL10 substrates was observed with increasing the thickness after deposition [54, 100]. Even though the reason for the poor interfacial strength might be the low tungsten substrate roughness instead of the thick coating thickness, this former spraying experience should be considered. We start with the coating with a 0.7 mm thick FG-layer as the first VPS batch, which produces a sharp fall of equivalent creep strain. The coating with a 0.7 mm thick FG-layer is chosen to be fabricated, and the coatings with 0.3 and 0.5 mm FG-layer are chosen for comparison.

4.2. VPS samples

Five coating systems with the same tungsten coating and different FG-layer (variable thicknesses and layer numbers) were deposited on EUROFER substrates by VPS. Five samples are named n-T(i) according to the layer number n and the nominal thickness i in 100 micrometer of FG-layer. Three and five stepwise layers were introduced to represent linear gradient considering the feasibility of the fabrication process. For forming of each FG-layer, both tungsten and EUROFER powders were sprayed synchronously from two nozzles, melted and mixed before they solidified on the substrate. The sample and its dimensions are shown in Figure 4.6. Table 4.1 shows nominal variations of five coating systems. The volume concentration of tungsten in the FG-layer gradually increases from the substrate to the tungsten coating. As it can be seen in Table 4.1, samples with five layers show a smoother gradient than those with 3 layers, and the same nominal thickness is specified for 3-T(5) and 5-T(5), as well as for 3-T(7) and 5-T(7).

Table 4.1: The nominal variations of five coating systems

Sample identifier	FG-layer				Tungsten coating
	No. and volume ratio (W/EUROFER)	Thickness μm			Thickness μm
		T(3)	T(5)	T(7)	
3-T(3)	3	25:75	100	166	500
3-T(5)		50:50	100	166	
3-T(7)		75:25	100	166	
5-T(5)	5	25:75	-	100	
		37:63	-	100	
50:50		-	100		
5-T(7)		63:37	-	100	
		75:25	-	100	

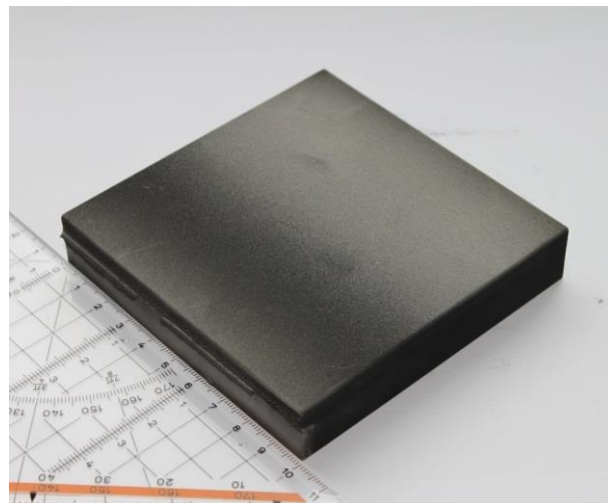


Figure 4.6: Sample 3-T(7) with a ruler.

Figure 4.7 shows the schematic of the sample layout used for investigations. Two blue parts with $50 \times 10 \text{ mm}^2$ in size are used for thermal shock tests which performed by FZJ. The orange parts with the dimension of $22 \times 5 \text{ mm}^2$ are used to investigate microstructure and mechanical properties of the coating system, and they are taken from the position parallel and perpendicular to the spraying direction (the moving direction of the substrate during spraying), and named P1, P2, and M1, M2, respectively. The green parts with the dimension of $27 \times 3 \times 4 \text{ mm}^3$ and $45 \times 3 \times 4 \text{ mm}^3$ are prepared for the bending tests.

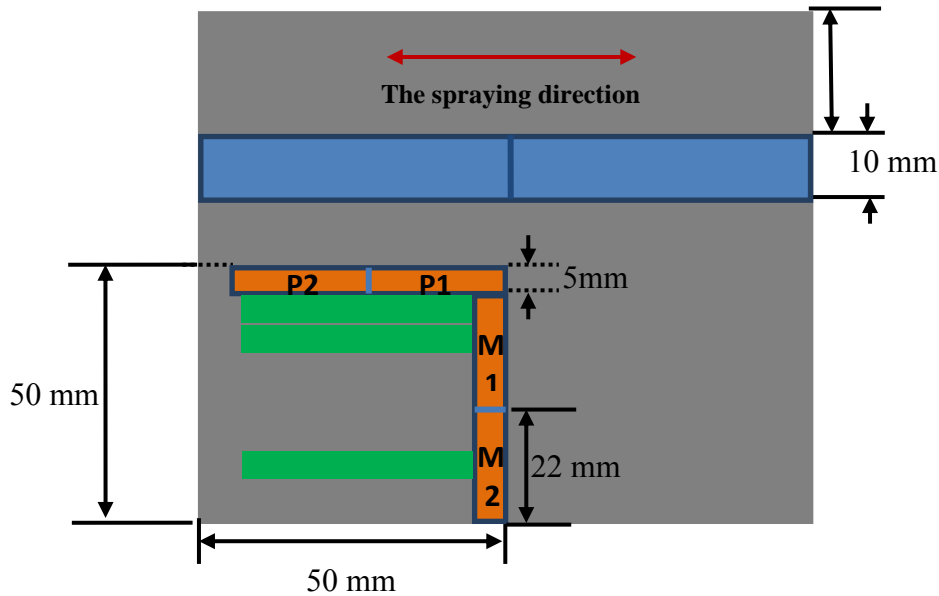


Figure 4.7: Schematic of sample layout and geometry.

4.2.1 Investigation on as-received surfaces

Before cutting the samples, roughness, elemental analysis and topography of the as-received surfaces were measured for five samples. 2D and 3D topography of the top surface were measured by the white light interferometer with 0.5 mm range, and the topography of five samples has the same tendency. Taking sample 5-T(7) as an example, as showed in Figure 4.8, the red color reflects relatively high morphology while the blue color reflects a low one in the range bar. A characteristic of 2D and 3D topography is a relatively low part in the middle comparing to the symmetrical edges of the whole sample (convex downward). The maximum height at the edge is $453 \mu\text{m}$, and the height reduces gradually from the edge to the middle. The bending is not caused by the residual stress introduced from the mismatch of CTE since if so, the opposite bending should be expected. Probably the reason is that one side of the substrate is fixed, so that the substrates could not freely shrink like the coating during the cooling phase.

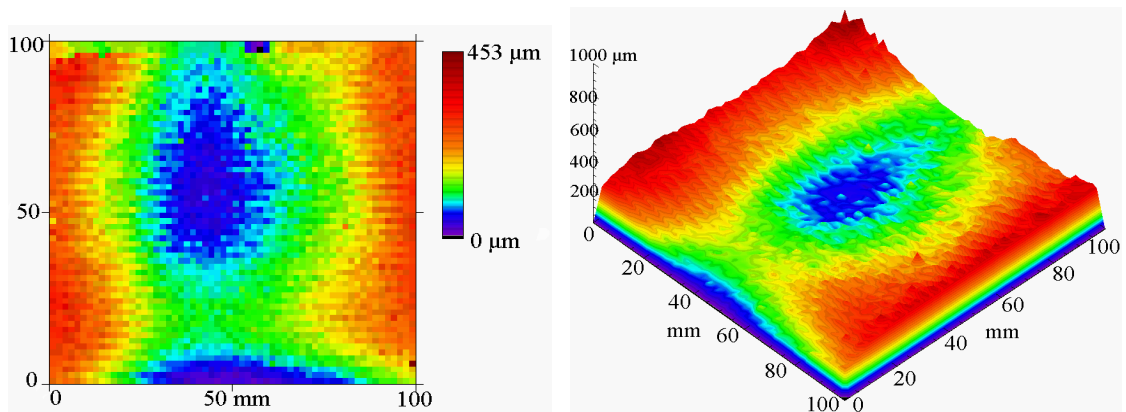


Figure 4.8: 2D and 3D topography of sample 5-T(7) from the top view (convex downward).

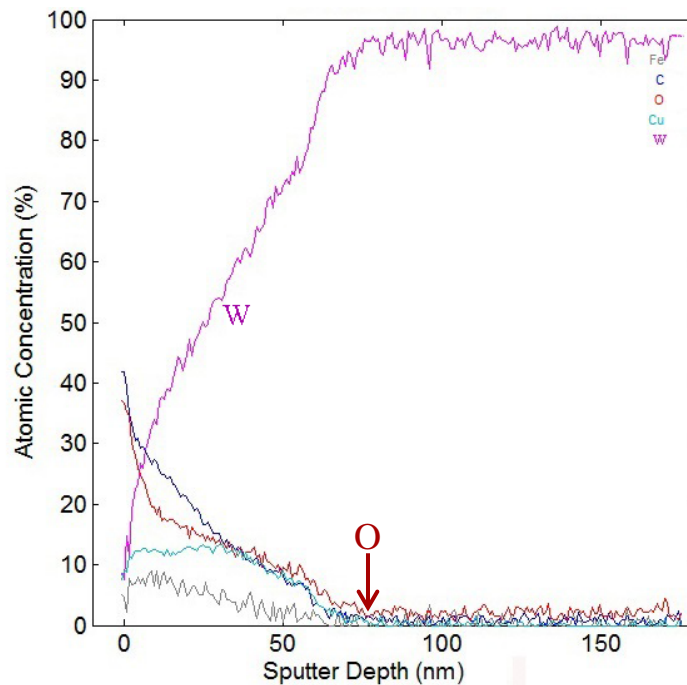


Figure 4.9: AES-Analysis of element concentration on the as-received surface of sample 3-T(5).

Figure 4.9 shows the element concentration on the as-received surface of sample 3-T(5). In addition to W, other impurities elements including Fe, C and Cu, in particular O, are observed on the as-received surface. However, with the increasing of sputtering depth, the atomic concentrations of the impurities are decreasing until they are nearly equal to zero when the sputtering depth is 68 nm. The sputtering depth is calculated from the sputtering time based on the sputtering rate of standard SiO_2 , which is equal to 1.7 nm/min. Even the real sputtering rate is heavily dependent on the characteristics of each material, the depth of impurities should be in the range of several tens of nanometers. This indicates that the oxygen impurity is from the surface absorption, and the vacuum

is guaranteed during VPS process. Other impurities are from the preparation process, e.g. EDM cutting process.

The as-received sample's roughness R_a is measured by a profilometer, and is shown in Figure 4.10. The R_a is $\approx 6.5 \mu\text{m}$ for the five samples. The rough surface is corresponding to un-melted tungsten particles on the as-received surface.

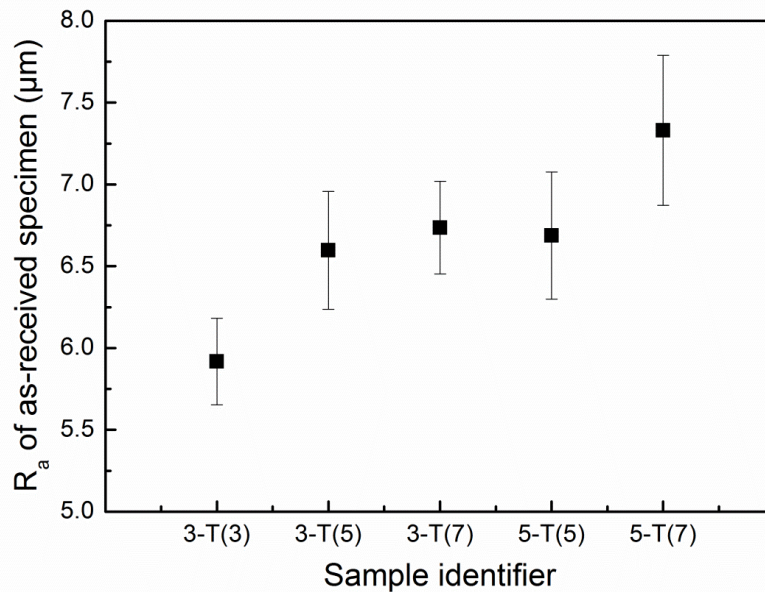


Figure 4.10: Roughness of as-received samples.

4.2.2 Comparison of the samples

True concentrations of tungsten were evaluated by area-scanning with EDX, as shown in Figure 4.11. Different layers of FG-layer are identified from microstructure and nominal thickness. A clear interface between the coating system and EUROFER substrate could be observed, while, there is no clear interface among each coating layer. True concentrations of tungsten in percent by volume are summarized and compared with nominal ones, as shown in Figure 4.12. True concentrations of W are quite consistent for the cases with 25% and 63% nominal value, while the true values are slightly lower than the cases with the other nominal values. Specifically, the error bar for the case with 50% nominal value is large. However, after linear fitting of the true concentration, the concentration of W follows a globally linear gradient as desired.

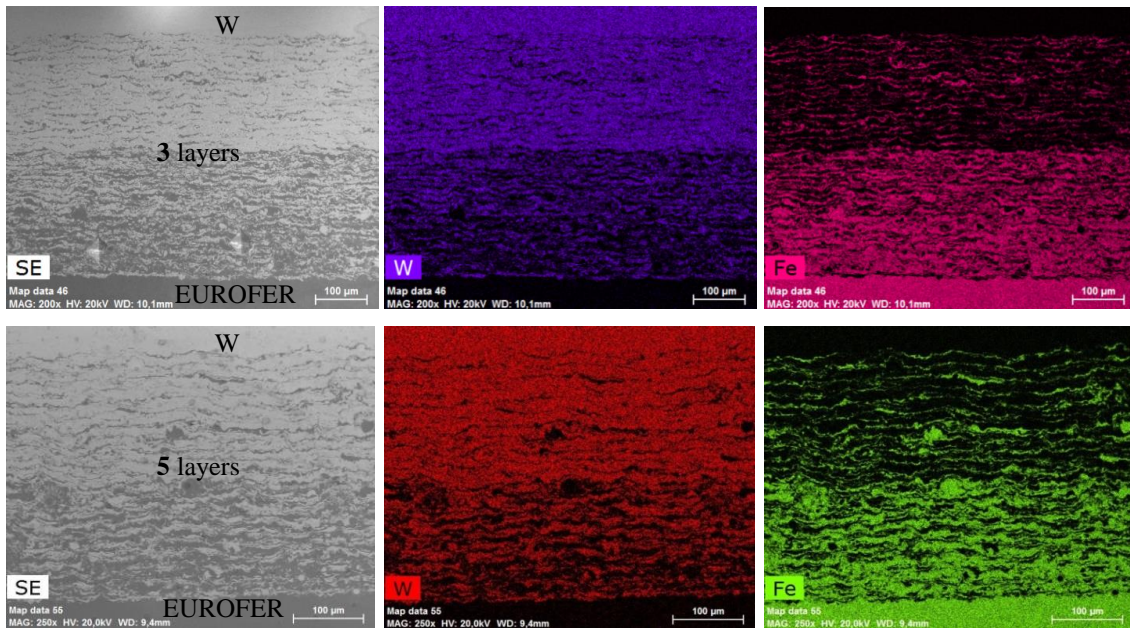


Figure 4.11: Distribution of tungsten and iron in cross-section of samples with 3 and 5 layers as FG-layer.

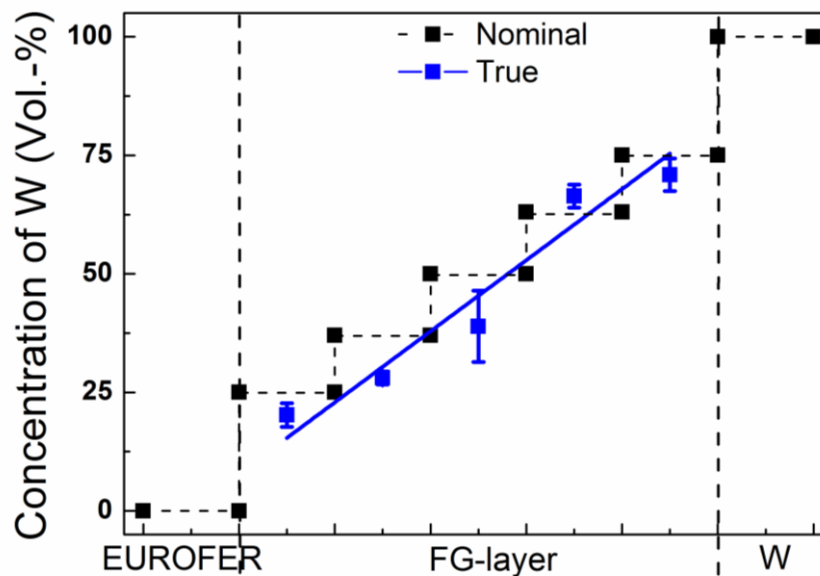


Figure 4.12: Gradient of FG-layer.

Figure 4.13 and Figure 4.14 compare five samples' nominal and true thicknesses of the FG-layer and the total coating system, respectively. The nominal thicknesses of the five samples are given in Table 4.1. Even true thicknesses are comparable with nominal ones, all of them are thicker than nominal ones. The thicknesses of coatings with 3 layers as FG-layer are indeed 341.1, 527.6, and 862.5 μm , and thicknesses of coatings with 5 layers as FG-layer are 638.8 and 935.5 μm . As shown in Figure 4.14, the total nominal thicknesses of the coating system are designed to increase gradually from 800 μm , 1000

μm to $1200 \mu\text{m}$ for FG-layer with three layers, and the thicknesses of FG-layer with five layers are designed to be $1000 \mu\text{m}$ and $1200 \mu\text{m}$, respectively. The true thicknesses of the five samples, shown by green bars, are comparable with the nominal ones. The thickness of tungsten coating is designed to be $500 \mu\text{m}$ for all the samples, while the true thickness of tungsten coating for sample 3-T(5) is $600 \mu\text{m}$. As a consequence, the total thickness of sample 3-T(5) is approximately similar to that of sample 5-T(5) even if the true thicknesses of FG-layer for both samples are different as shown in Figure 4.13.

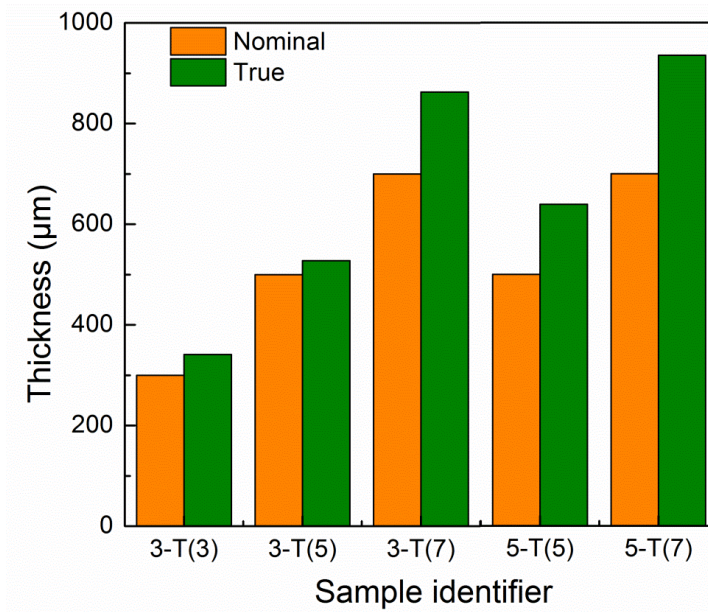


Figure 4.13: Nominal and true thickness of FG-layer.

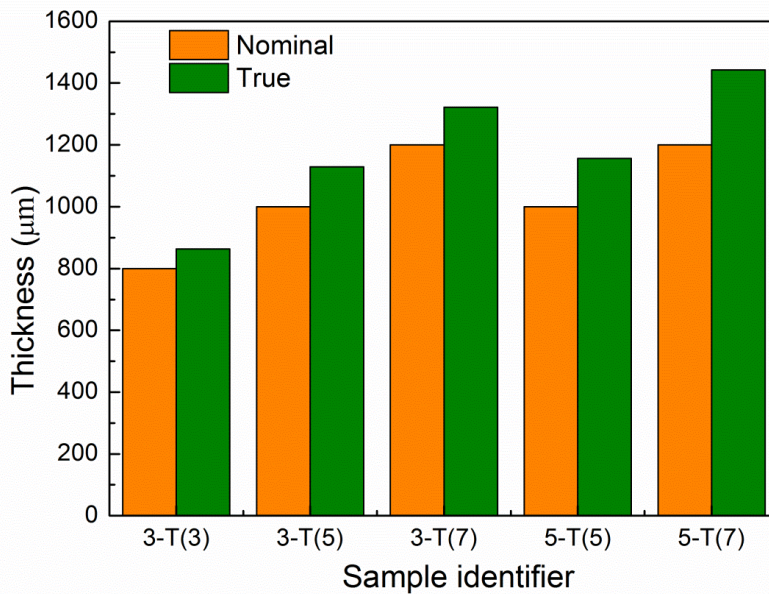


Figure 4.14: Nominal and true thickness of the coating system (thickness of tungsten + FG-layer).

4.2.3 Discussion and conclusion

Three and five stepwise layers as the representative of linear gradient were chosen for FG-layer considering the feasibility of fabrication and former spraying experience on W/EUROFER composite coating [54, 100]. FG-layer with linear gradient and thicknesses in the range of 0.1 to 4 mm has been investigated by FE simulation in section 4.1. Three thicknesses were chosen for the 1st batch VPS fabrication.

The FG W/EUROFER coating system on EUROFER substrates has been fabricated by VPS successfully. The five fabricated samples have several aspects in common including the as-received surface topography and surface roughness.

Based on the analysis of gradient, the stepwise linear gradients with three and five layers as FG-layer are observed for all five samples. In addition, the samples with five layers as FG-layer have the advantage of smooth gradient as expected. However, the distinction between the layer with nominal tungsten volume concentration of 75% and that of 63% is not obvious. This could be due to a slight difference of both layers' powder weight. In addition the fact that both powders were mixed during spraying from two nozzles makes precise control of the volume concentration difficult.

Besides gradient, the thickness of the coating is another important characteristic. The true thicknesses of FG-layer and the whole coating system are a bit larger than but still comparable to the nominal ones. The effect of thickness on microstructural and mechanical properties will be reported in the following sections.

4.3. Microstructure

4.3.1 Pure W coating

The microstructure characteristic of as-received tungsten surfaces from top view is shown in Figure 4.15 (a-f). Figure 4.15 (a, b and d) show that each pancake-like structure covers on the others, what indicates that tungsten particles melt well during the spraying process and re-solidify to form a pancake-like structure. A sloppy surface is observed in Figure 4.15 (c), and the reason for this kind of surface is that the flowing of melted particles is hindered by unmelted particles. Disk-shaped splats (also called pancake-like structures in the work) with less peripheral fingers are observed. As discussed in Section 2.2.2, the forming of the structure of disk-shaped splat is not only owing to well-melted particles benefited by optimized spraying parameters, owing to a preheating substrate with the temperature higher than the transition temperature. The diameter of the pancake-like structure is measured based on SEM images and summarized in Figure 4.16. The mean diameters of the pancake-like structure are around 27 μm . The comparable pancake-like structures of five samples prove a reproducible fabrication. Several spherical or irregular particles with the diameter of $\approx 10 \mu\text{m}$ are observed on the surface (see Figure 4.15 (b, c and d)) and they are unmelted tungsten particles with a size similar to the original tungsten powder. The irregular particles were deformed during peening on the pre-coated ground. The surface with unmelted particles is rough. In addition, even the pancake-like structures are joined with each other well (see Figure 4.15 (a, b and d)), few pores are observed in the connection areas among pancake-like structures, as shown in Figure 4.15 (d). The SE and BSD images of pure tungsten coating after polishing are shown in Figure 4.15 (e, f), respectively. Pores with several micrometers can be observed for both modes of micrograph, while unmelted particles are not so clear.

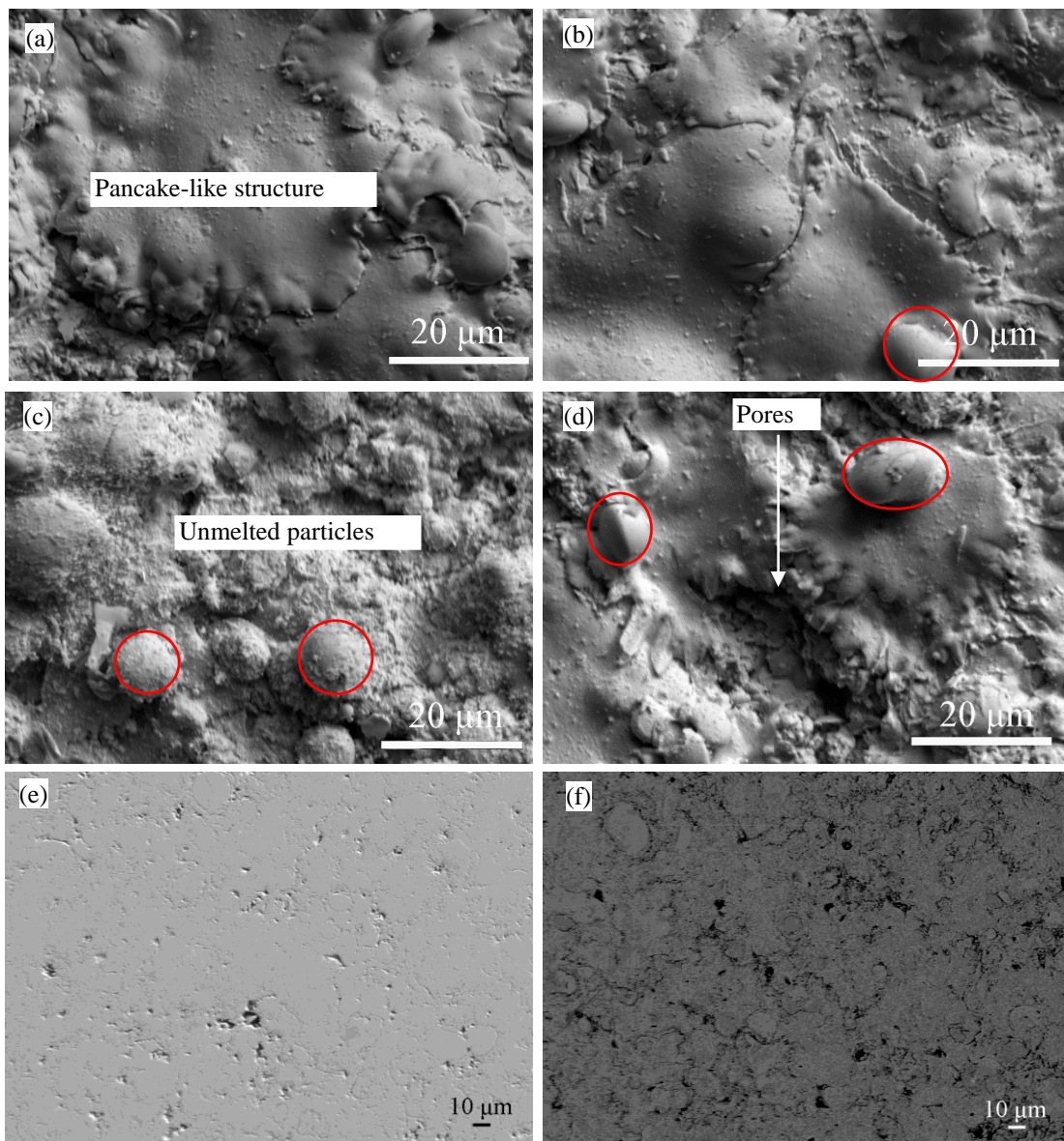


Figure 4.15: The characteristics of as-received pure tungsten coating surfaces: (a-d) unpolished surfaces; (e, f) polished surfaces.

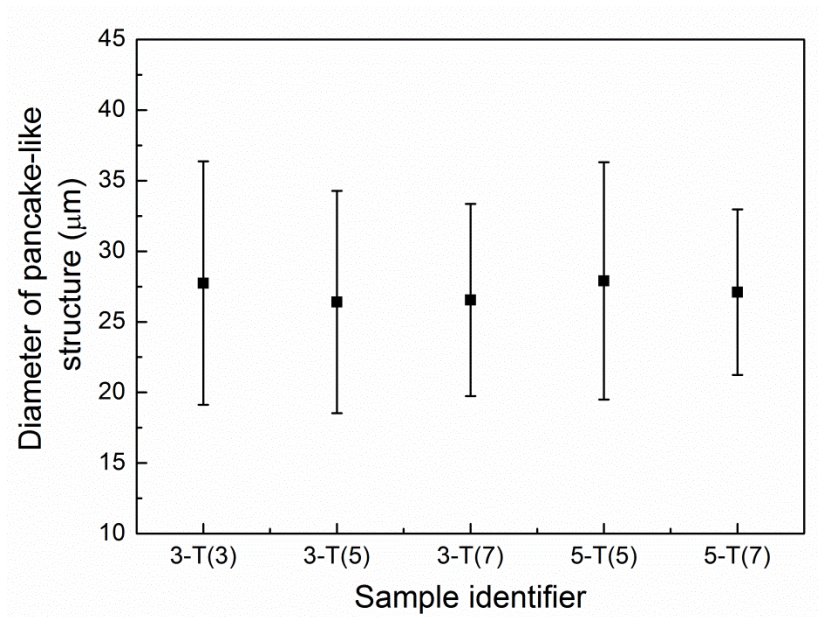


Figure 4.16: Diameter of the pancake-like structure.

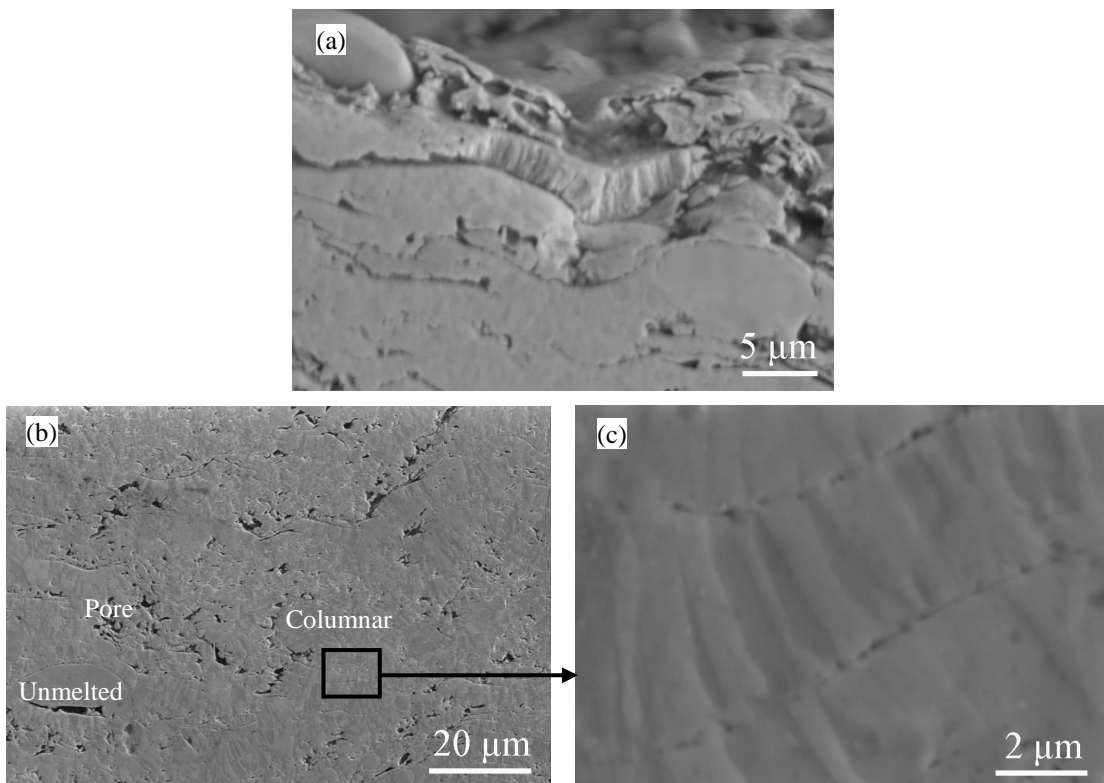


Figure 4.17: Cross-section microstructure of pure tungsten coating.

Figure 4.17 shows the cross-section microstructure of pure tungsten coating. A laminar structure is one common characteristic of thermally sprayed coating, as shown in Figure 4.17 (a). Irregular pores with several micrometers in diameter and few un-melted tungsten particles are observed in Figure 4.17 (b). Most pores occur around un-melted parti-

cles and at interfaces among lamellar layers. Except those defects, columnar grains with aspect ratio ≈ 3.9 as shown in Figure 4.17 (c) account for a large proportion after zooming in. Columnar grains were formed due to the temperature gradient during the resolidification of well-melted particles on the substrate or a precoated surface. The size of the columnar crystals is $\approx 4 \mu\text{m}$ in height and the columnar grain is radially oriented perpendicular to the substrate. No crack or delamination could be observed in tungsten coating and FG-layer. It is assumed that the porous structure constrains the propagation of fissures or cracks [47].

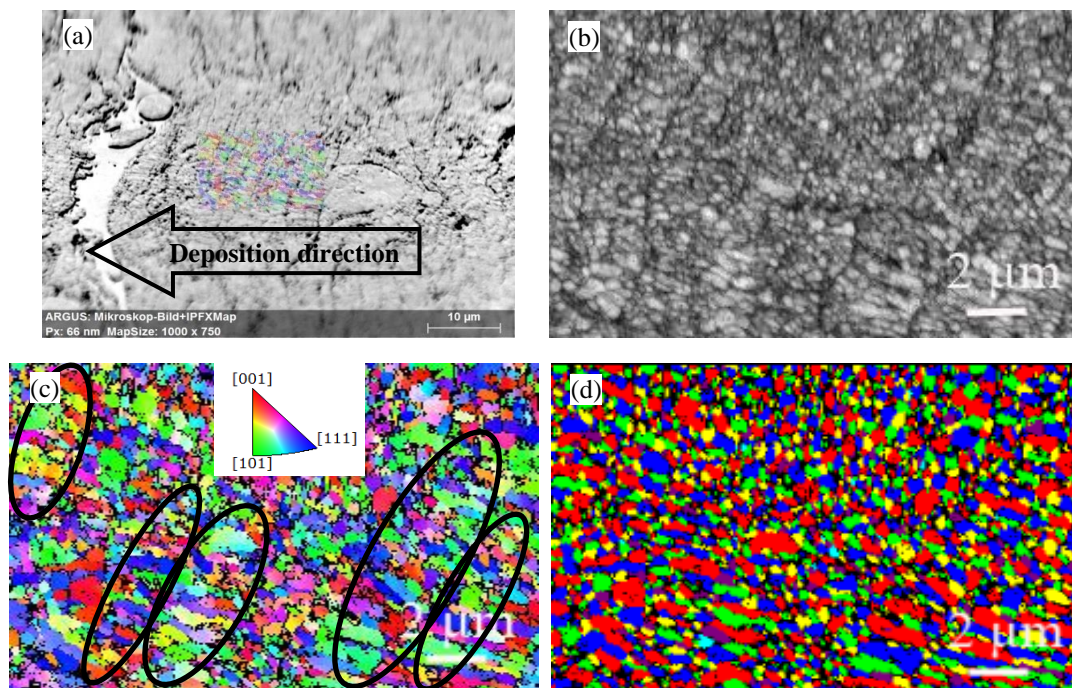


Figure 4.18: The grain characteristics of pure tungsten coating: (a) SEM image; (b) pattern quality; (c) grain orientation map and (d) grain distribution map.

EBSD is used to investigate the grain characteristics of tungsten coating, e.g. the orientation of columnar grain and the grain size. The detection region of EBSD on microstructure, and its related pattern quality, grain orientation map and grain distribution map in tungsten coating are shown in Figure 4.18. The grains are identified based on the minimum misorientation 5° and the minimum pixel size 5. The colors on grain distribution map are randomly chosen by software, and are no relationship with grain orientation. SEM micrographs show the deposition direction which is perpendicular to the substrate. Columnar grains lie inside each pancake-like structure labeled by the ellipses shown in Figure 4.18 (c) and they are parallel to the deposition direction. The grain size of pure tungsten coating is measured and concluded in Figure 4.19, the average size of 1385 grains is $0.561 \mu\text{m}$, and the average size after fitting based on Gauss distribution is equal to $0.355 \mu\text{m}$. When the degree of supercooling is larger during the condensation of melted particles, the nucleation sites of grains will be much more than the one with

smaller degree of supercooling, correspondingly the columnar grain size will be much finer. Some even finer grains are also observed in Figure 4.18 (c), those are considered to be the “figures” of splats.

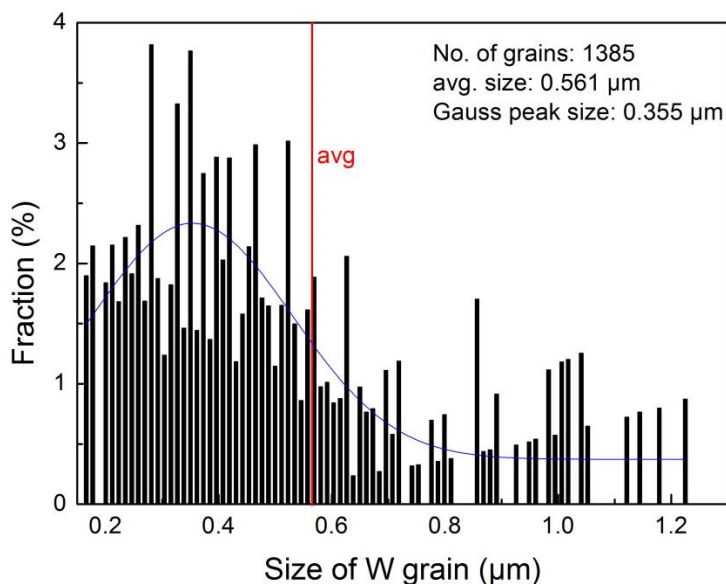


Figure 4.19: Grain size of pure tungsten coating.

The software ImageJ was used to analyze porosity in the work. Its principle is to calculate the area ratio of pores by adjusting the contrast of microstructure images. Figure 4.20 (a, b) is an example for calculating and evaluating of the porosity. An 8-bit image is firstly transformed from the original microstructure as illustrated in Figure 4.20 (a). The threshold of the 8-bit image is adjusted to get a figure as Figure 4.20 (b) in which pores are black comparing to other phases. In the end, the area fraction of pores is calculated to represent the porosity. For statistics, ten pictures are taken for each specimen. The porosity versus the nominal concentration of W of sample 3-T(5) is summarized in Figure 4.20 (c). The optimized spraying parameters and the vacuum condition, accompanied by proper melting and re-solidification of powders, produce a low porosity of all coating systems. In particular, the porosity of W coating is $\approx 4\%$ according to the images analysis, and that of FG-layer is less than 2%. The low melting point and ductility of EUROFER powders benefit the flowing of melted particles and yield the low porosity. In addition, the comparable low porosity is observed for other samples, as shown in Figure 4.20 (d).

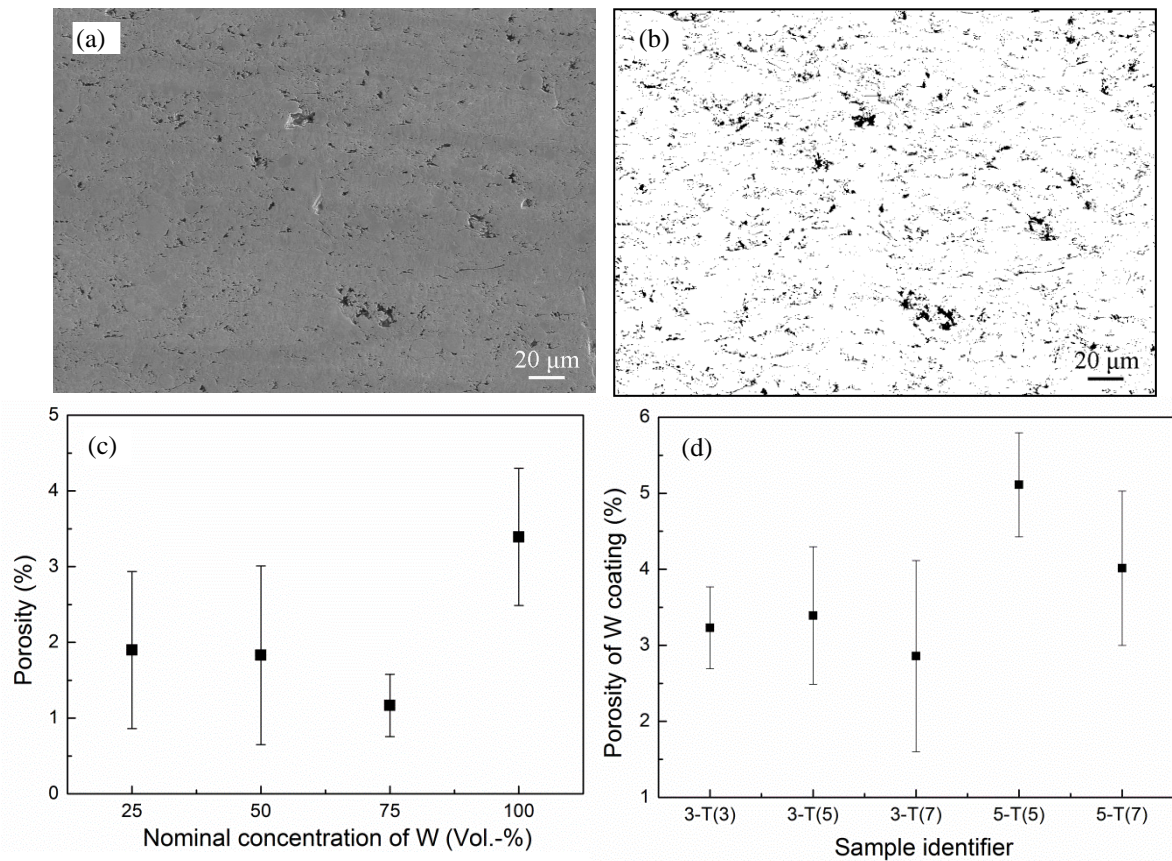


Figure 4.20: (a, b): an example of porosity calculation (pure tungsten coating of sample 3-T(7)); (c): the porosity versus the nominal concentration of W of sample 3-T(5); (d): comparison on porosity of the five samples' tungsten coating.

4.3.2 FG W/EUROFER coating with three layers

As shown in Figure 4.21, the cross-sectional SEM micrographs of FG-layer with three layers show that stepwise linear gradient is formed successfully between tungsten coating and EUROFER substrate. There is no obvious interface among each FG-layer. The tungsten concentrations in the three layers have been investigated by area scanning of EDX and discussed in section 4.2.2. A laminar structure and small pores among laminar layers are observed in FG-layer. No delamination or defects are observed in all the coatings.

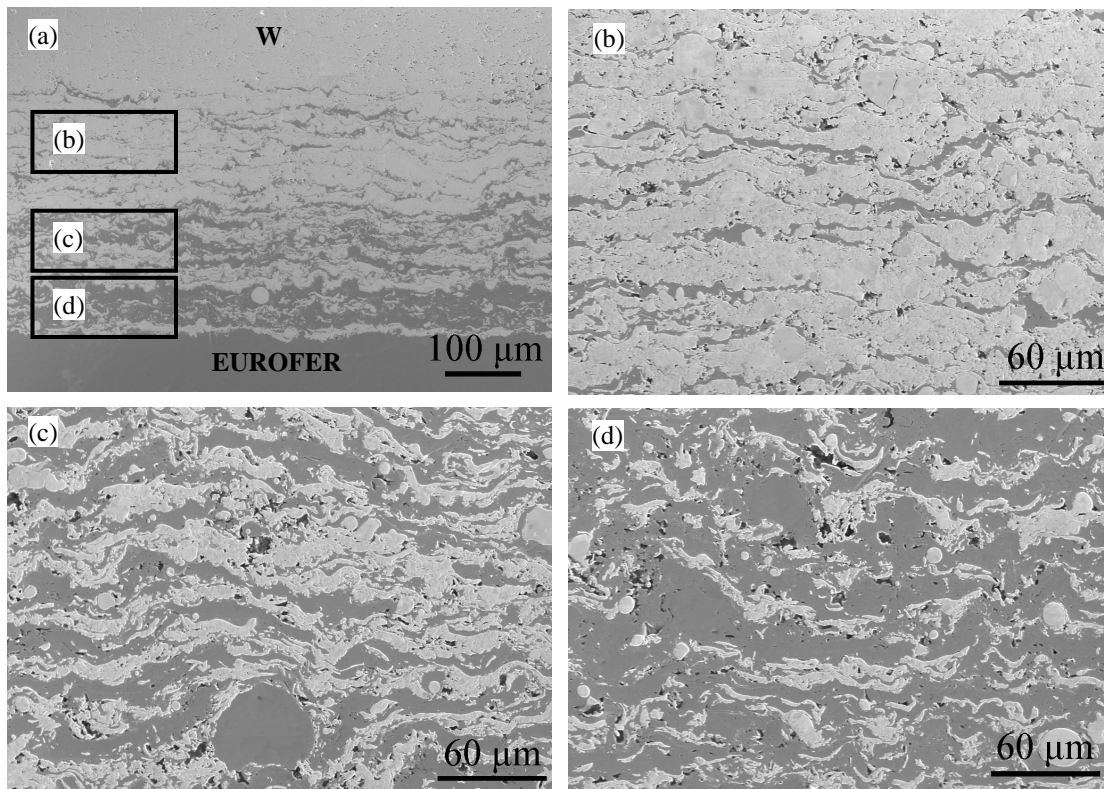


Figure 4.21: (a) The cross-section microstructure of sample 3-T(7) and its FG-layer with the nominal concentration of W: (b) 75; (c) 50 and (d) 25 in Vol.-%.

The magnification of FG-layer with tungsten concentration of 50% is shown in Fig. Figure 4.22 (a). As it can be seen, W and EUROFER phases can be distinguished from the contrast. Pores exist at the interfaces of laminar layers, and most of them are around tungsten phase. Columnar tungsten grains are observed in three FG layers, as shown in Figure 4.22 (b, c and d). Although no columnar EUROFER grain is observed in SEM images, columnar grains are also formed in well-melted EUROFER particles, as marked by the ellipse of Figure 4.23 (c) and in the EBSD images (see Figure 4.23 (c-e)). Considering the forming process of columnar grain, the re-solidification of well-melted particles is proved to exist not only in W coating but also in FG-layer.

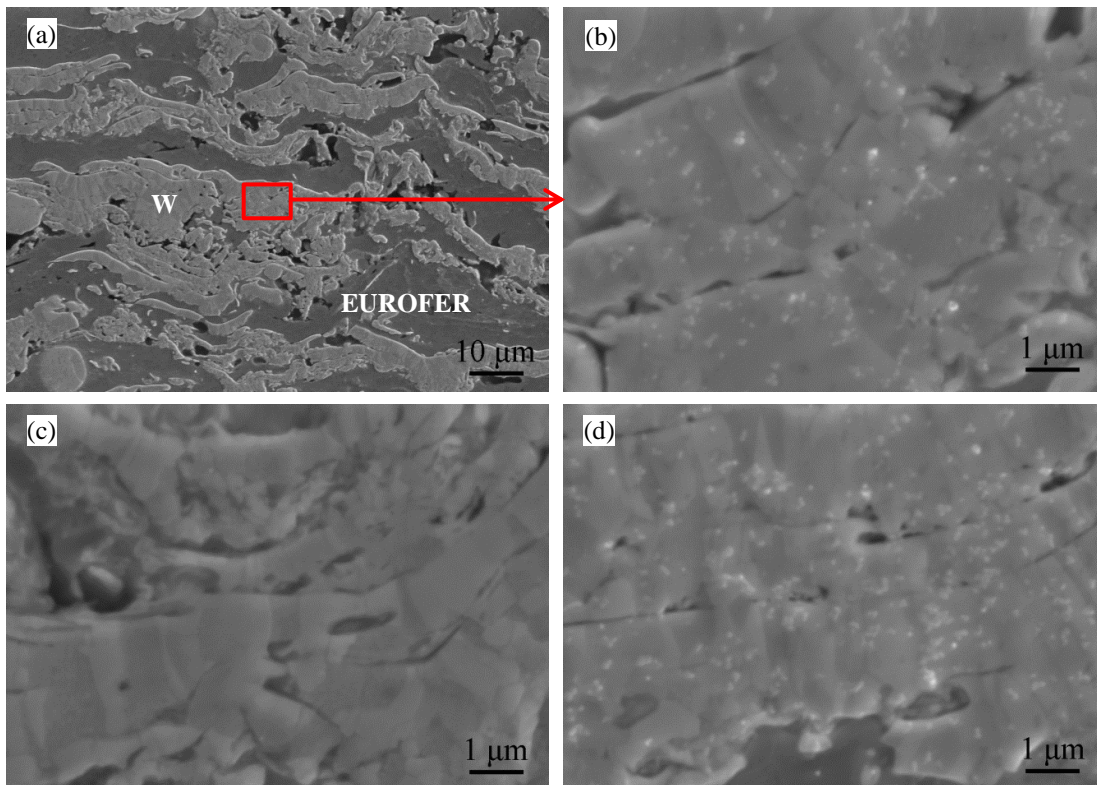


Figure 4.22: (a) Magnification of FG-layer (W50% layer) and columnar tungsten grains in FG-layer with (b) W50%, (c) W25%, and (d) W75% of sample 3-T(7).

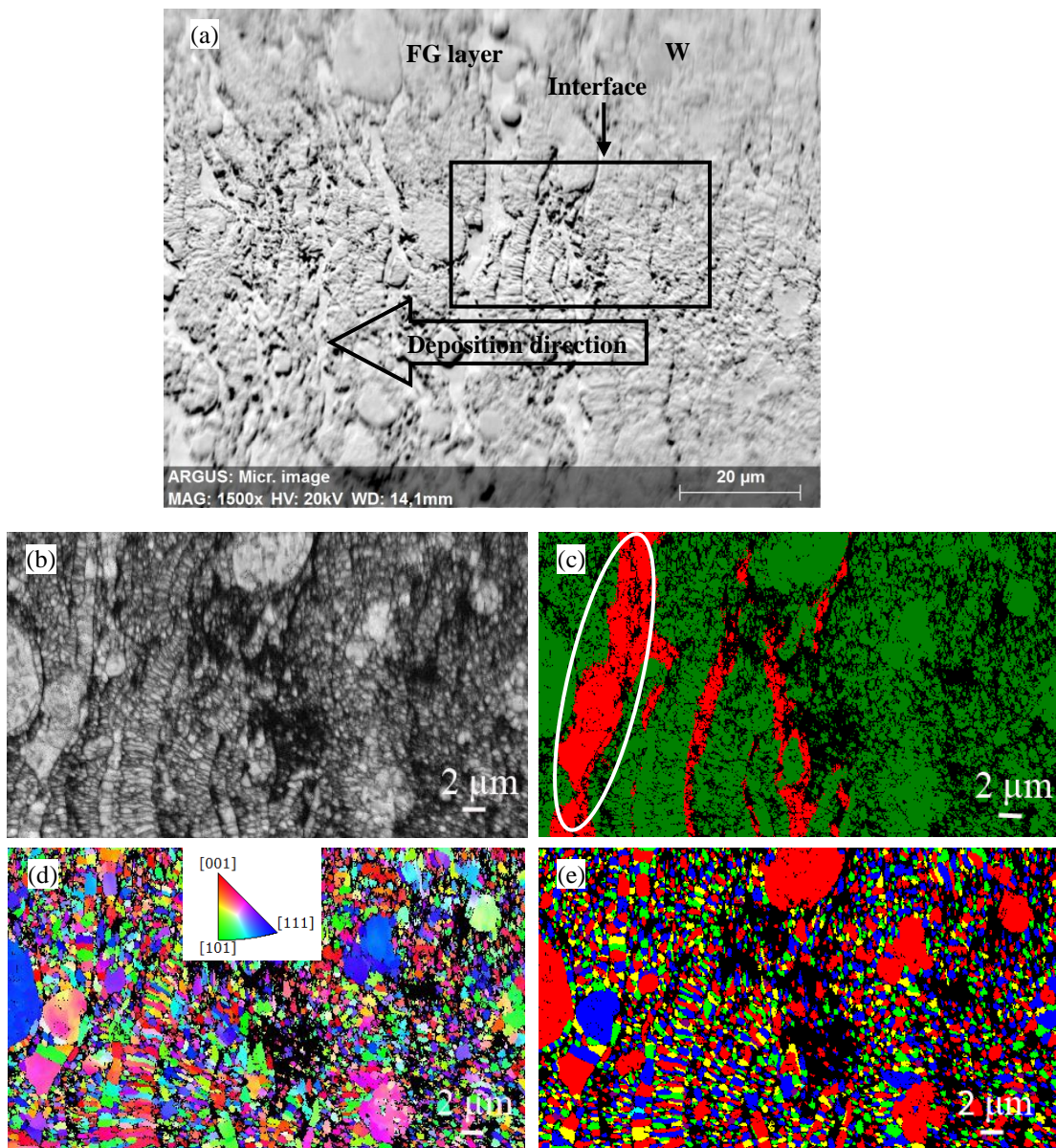


Figure 4.23: EBSD shows grain characteristics of W75%-W100%: (a) SEM image; (b) pattern quality; (c) phase map; (d) grain orientation map and (e) grain distribution map.

An inhomogeneous texture of the coating system has been observed in Figure 4.23, it composes of few large round un-melted particles and fine randomly oriented grains (less than 1 μm in size), as well as columnar grains. Tungsten phase is in green and iron phase is in red as shown in Figure 4.23 (c).

4.3.3 FG W/EUROFER coating with five layers

The cross-sectional SEM micrographs show that stepwise linear gradient is formed successfully between tungsten coating and EUROFER substrate. There is no delamination and no obvious interface among FG-layer, especially for the coating system with five layers as FG-layer, as shown in Figure 4.24.

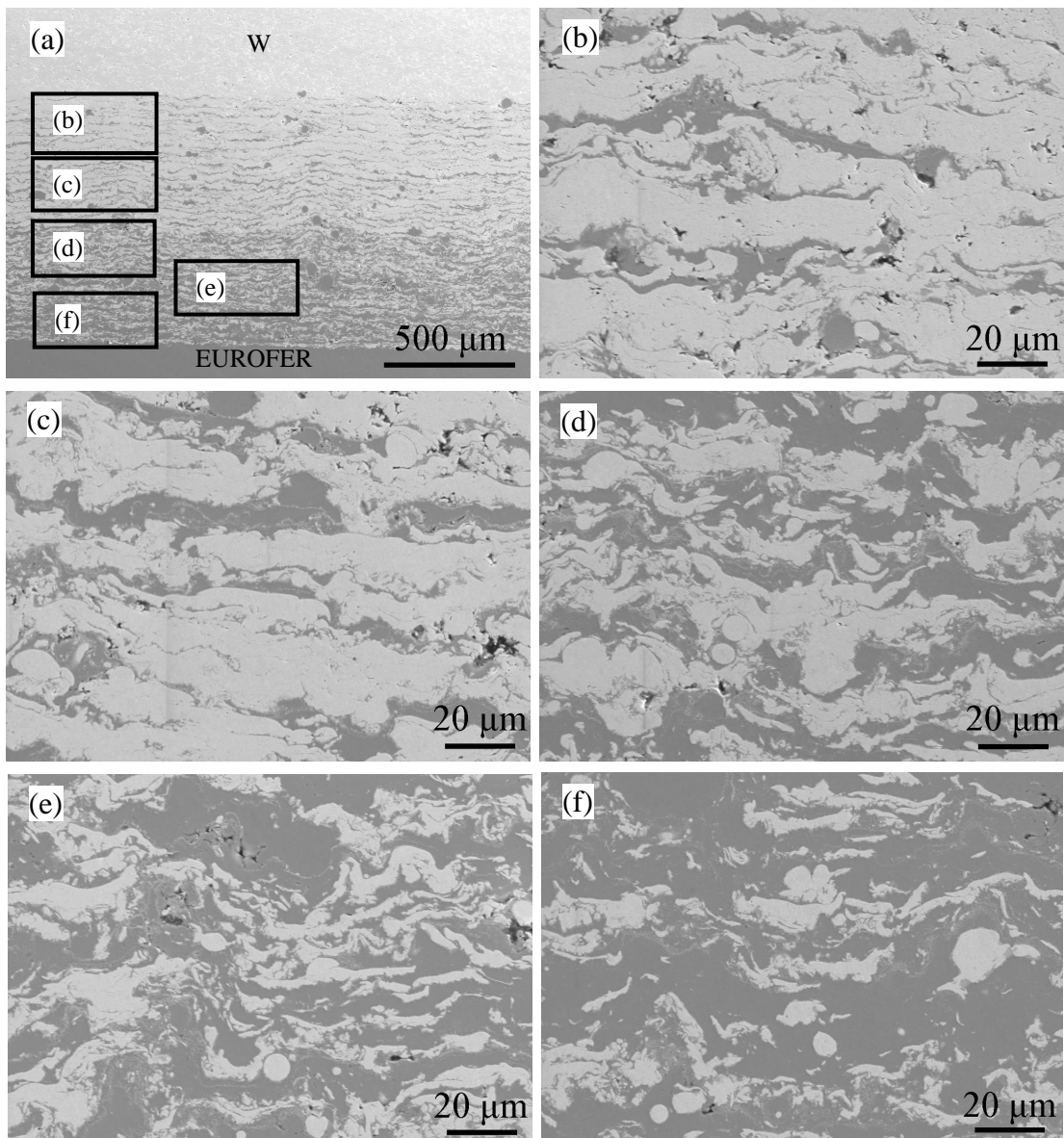


Figure 4.24: (a) The cross-section microstructure of sample 5-T(7) and its FG-layer with the nominal concentration of W: (b) 75; (c) 63; (d) 50; (e) 37 and (f) 25 in Vol.-%.

4.3.4 Interface between the coating system and substrate

Sandblasting was applied on the substrate surface prior to the spraying process. Thereby a rough surface with $R_a = 3.96 \mu\text{m}$ was achieved. Since a rough substrate surface is nominally considered to be beneficial for improving bonding strength, sand or grid-blasting is also used to get a rough surface in other works [46, 101, 102]. This surface preparation is similar to the surfi-sculpt technology which is proven to improve the mechanical adhesion due to regulated coating's cracking and segmentation [20].

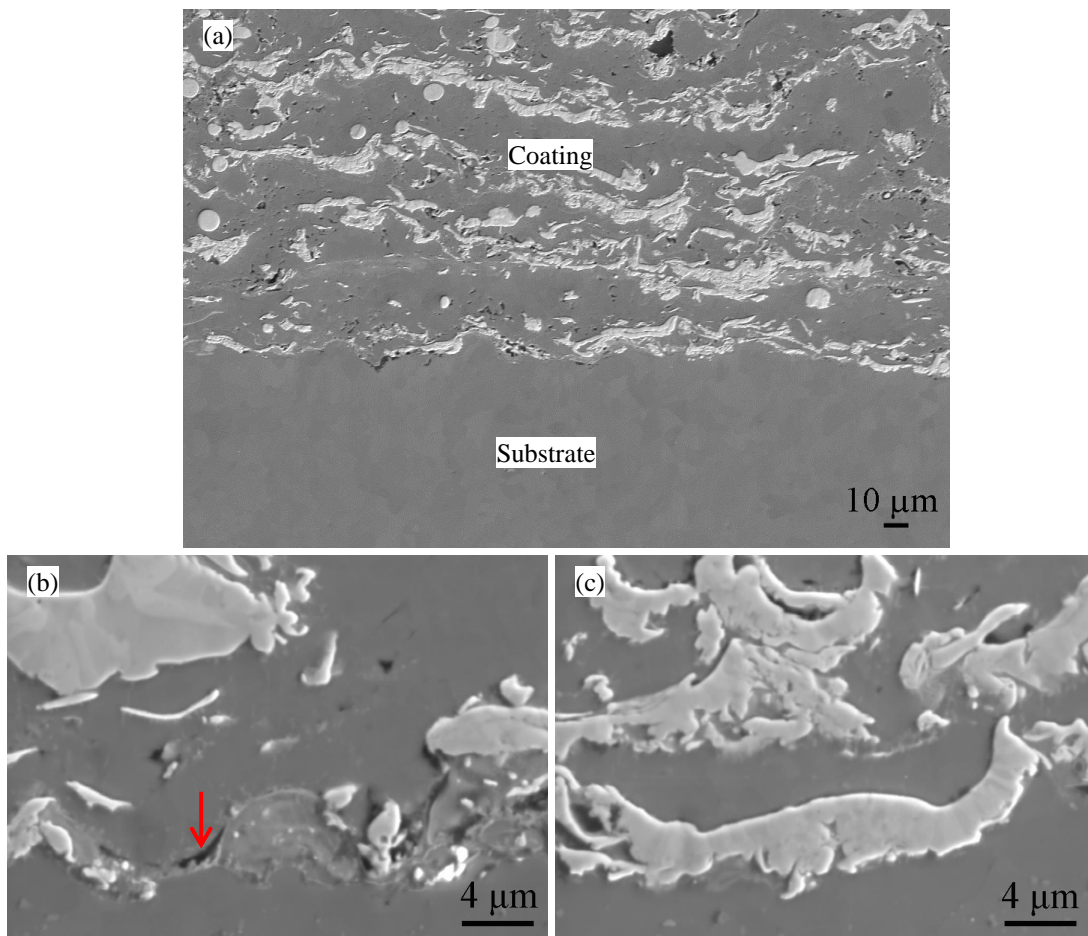


Figure 4.25: Substrate interface morphology of sample 3-T(7).

A sound interface between the FG-layer and EUROFER substrate (named substrate interface in the work) has been observed for all five samples, and the substrate interface of sample 3-T(7) is shown in Figure 4.25 (a). Figure 4.25 (b) and (c) specify two possibilities of the first deposition layer: EUROFER and W layer. No matter if the first deposition layer is composed of EUROFER or W, interfaces without crack or delamination have been obtained, even there are few gap-like defects (pointed out by an arrow in Figure 4.25 (b)).

4.3.5 Discussion and conclusion

As discussed in section 2.2.1, the properties of thermal spraying coating mainly depend on the substrate morphology and temperature, as well as the powder size, temperature and velocity of the sprayed particles. The powder size and the spray parameters have been optimized and fixed based on a former work by Weber [54]. In general, a higher temperature of the substrate benefits on the formation of a well-defined columnar microstructure. The influence of substrate temperature on texture has been investigated in [78]. With increasing the temperature of the substrate (tungsten substrate), the fraction of columnar grains increases while the fraction of large unmelted grains and the number of pores decreases [78]. The transition temperature for mild steel and AISI304 steel is around 300 °C [74, 77], and the transition temperature of 400 °C is estimated for a stainless steel in [76]. Accordingly, the preheating temperature should be at least higher than 300 - 400 °C. Furthermore VPS-W coating formed on F82H substrate with the preheating temperature of about 600 °C has an inhomogeneous texture. Therefore, the preheating temperature of substrate over 600 °C should be beneficial for a homogeneous texture. Considering the temperature for tempering heat treatment of EUROFER substrate, the substrate temperature shall be kept below 760 °C.

Microstructures of both tungsten coating and FG-layer have been investigated and reported in this section. Characteristics including porosity, unmelted particles and columnar grain have been observed for all five samples, which are the typical characteristics for VPS coating owing to thermal spraying process.

There are three kinds of grains: large round grains, fine randomly oriented grains and columnar grains. Columnar grains are considered to be formed due to the temperature gradient during the re-solidification of well-melted powders. While the “figures” of pancake-like structure could be one of forming reasons of fine grains, the other forming reason could be the splashing of melted powders during impacting on the substrate or the former layer. Large degree of supercooling contributes fine grain. The large round grains are mainly from the un-melted or partly melted powders. Columnar grains account for the main structure of the coating system based on microstructure investigation.

Porosity is an important assessment criterion of coating quality. Two kinds of pores are observed from cross-section microstructure. Pores with the size of submicron occur regularly among laminar coatings, and pores with the size of micrometer are around large un-melted or partly melted particles. Those pores are formed during the re-solidification process. The pores lead to a reduction of Young's modulus and hardness, which will be compared and discussed in section 4.4. Compared to 20% of VPS-W coating [47], or ~ 9% of VPS-W coating [20, 103], the porosities of pure W coating and FG-layer in this work are ~ 4% and 2%, respectively. Low porosity has been observed here for all five samples. Even lower porosity of 0.6% is reported in [46].

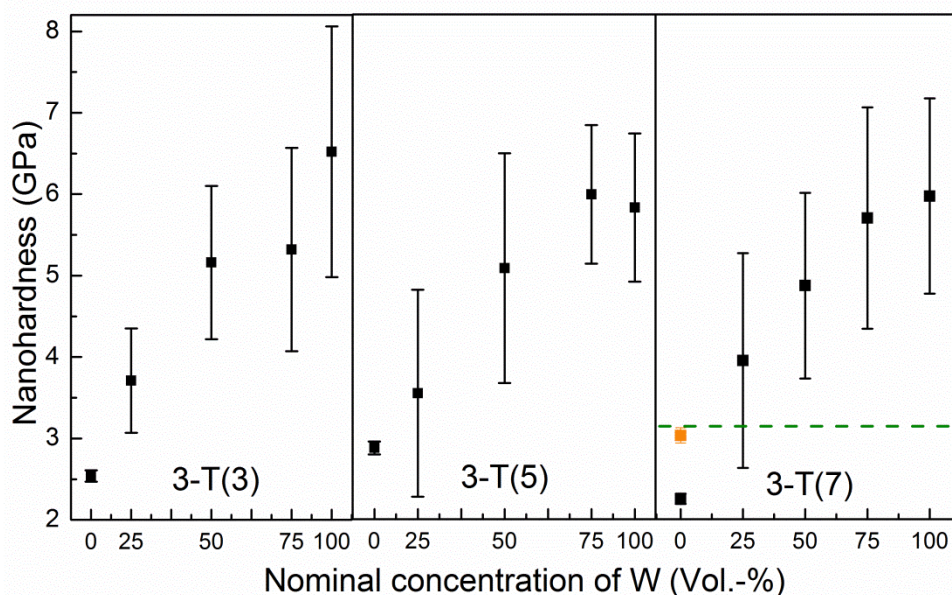
Substrate interfaces are free of cracks and delamination. It seems that a metallurgical bonding has been achieved as a result of proper spraying parameter and rough substrate surface. Quantitative investigation on interface toughness and interface bonding are performed and reported in section 4.4.

4.4. Mechanical Analysis

4.4.1 Nanohardness and Young's modulus

Nanohardnesses of the five coating systems have been investigated and summarized in Figure 4.26. Nanohardnesses of the five samples are comparable and the hardness values for each sample increase proportionally with the concentration of tungsten, which also reflects a successful gradient. In addition, comparing to the bulk substrate material, the scatters of all coatings' hardness are relatively high due to the heterogeneous microstructure. The diameter of the indentation for tungsten coating is $\approx 7 \mu\text{m}$, while that for FG-layer is $\approx 10 \mu\text{m}$. Hardness of the coating can be affected by the re-solidification composite, a single large unmelted particle or even a pore. The indentations' data capacity of 30 for each layer is not large enough to follow the Gaussian distribution or other distributions. Therefore, the mean value is used here. Each data in Figure 4.26 represents a mean value of 30 indentations. The uniform distance between two indents is $100 \mu\text{m}$ which is around 10 times of the indent's dimension. No cracks are observed around indentations.

For sample 3-T(7), the green dotted line shows the nanohardness (3.14 GPa) of the as-received EUROFER plate, and it is 39.6% higher than the nanohardness (black dot: 2.25 GPa) of the substrate. It is also higher than the others samples' substrates. However, the nanohardness of the as-received EUROFER plate is close to the orange dot which is the hardness at the position from the substrate interface $> 4 \text{ mm}$. Except the hardness of the orange point, all the others hardness values of the substrate were measured at the position near the substrate interface ($< 4 \text{ mm}$). Further investigation and explanation on the mechanical changes of the substrate will be discussed in the section 4.4.2.



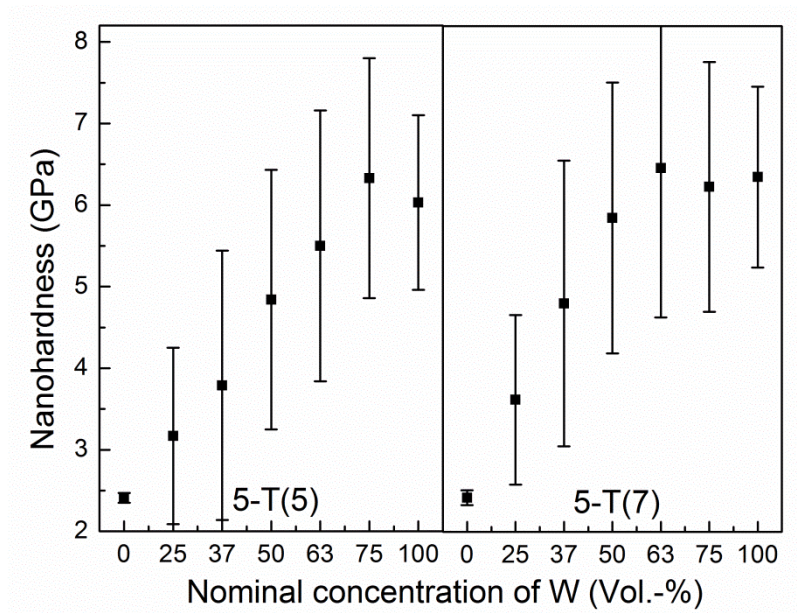


Figure 4.26: Nanohardness versus the nominal concentration of W.

Nanoindentation could be also used to measure the Young's modulus. The details are introduced in Section 3.3.1.1. In the Figure 4.27, each dot represents the mean Young's modulus of 30 data. The Young's modulus of each sample increases gradually with the nominal concentration of tungsten. The Young's modulus of W37% and W63% are quite similar to that of W25% and W75%, respectively, the results of the Young's modulus are quite consistent with the microstructure characteristic. Comparing to the Young's modulus of bulk tungsten at RT, the Young's modulus of tungsten coating is roughly 77% of bulk tungsten even the porosity of the tungsten coating is only about 4%. Young' modulus of W coating is not linear related to the porosity. The correlation of Young' modulus and porosity is demonstrated to be closely related to the power-law empirical relationship for pores materials [104]. Predictive equations which link characterizations of pore geometry, orientation, and pore arrangement with fundamental mechanical properties do not yet exist since only the density or the average porosity is considered in most investigations [105].

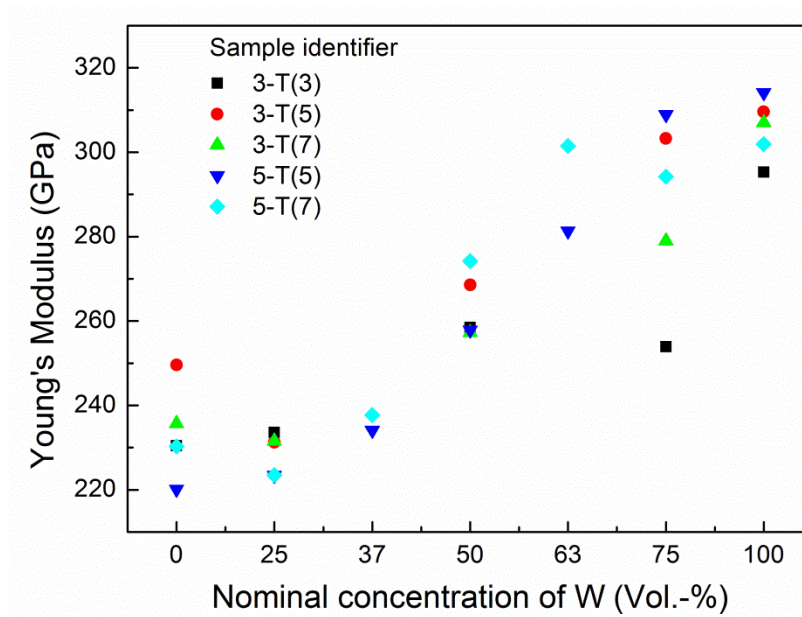


Figure 4.27: Young's modulus versus the nominal concentration of W.

4.4.2 Microhardness

Unlike local mechanical properties measured by nanoindentation, microhardness reflects global properties on a scale of 60-90 μm . Because of its relative global characteristic, microhardness measurement has been performed to investigate the global homogeneity of the whole sample. Four pieces of one sample have been chosen, and two of them are from the parallel to the moving direction of the substrate, the others are from the perpendicular direction, as shown in Figure 4.7. The results are shown in Figure 4.28, the microhardness at different positions is comparable with each other; nevertheless, the error bars are still large. Those prove that even the local microstructure is heterogeneous with three kinds of grains and pores, global homogeneity and good coating quality with well overlapping of laminar layers have been observed. The microhardness of FG-layer increases proportionally with the increasing concentration of tungsten, which is another proof of a fine gradient.

Average microhardness of tungsten coating is 4.1 GPa, which is comparable with that of W coating in [106] and equal to 89.7 % of bulk tungsten fabricated by powder injection moulding [38]. This low hardness is attributed to the porosity of the microstructure. However, it is much higher than that of VPS-W coating with 20% porosity [47].

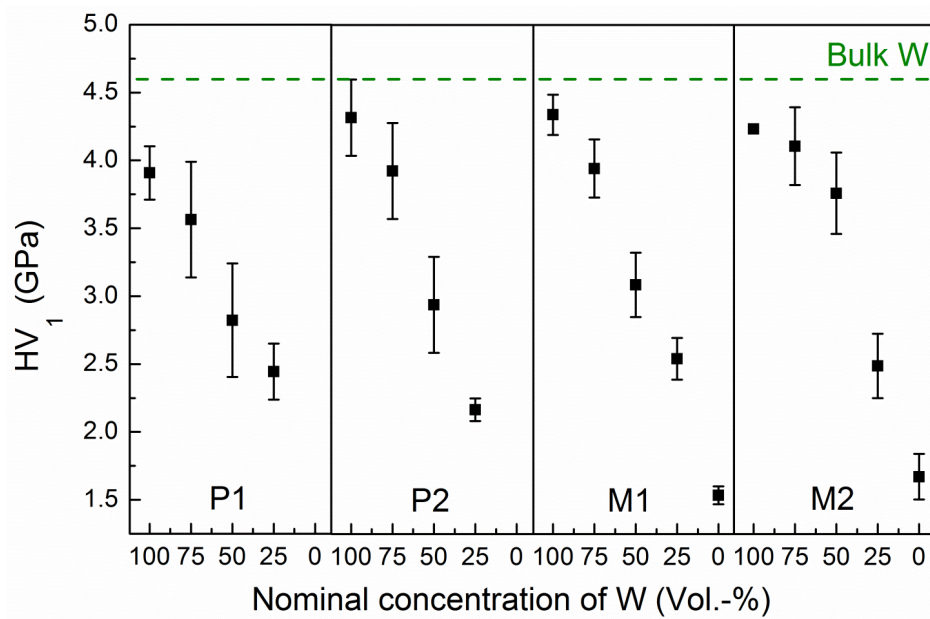


Figure 4.28: Vickers hardness versus the nominal concentration of W of sample 3-T(7).

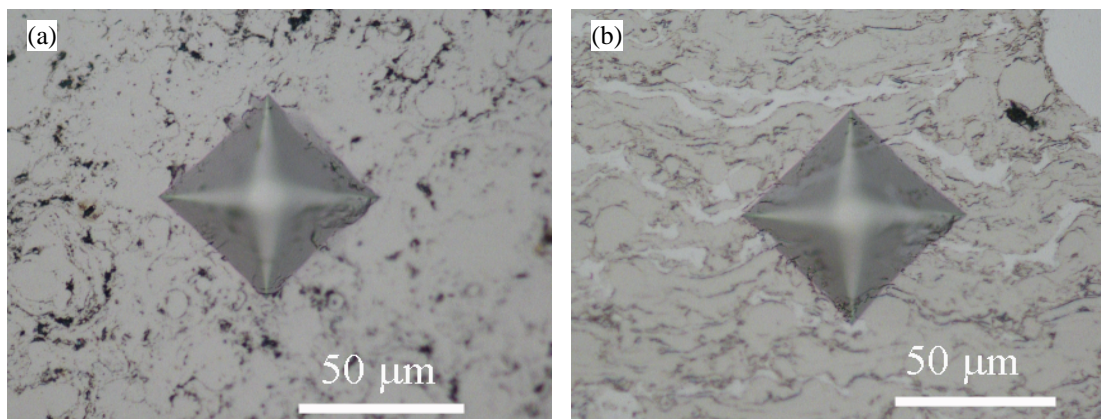


Figure 4.29: Micrographs of microhardness's indentations (a) pure W from the top view; (b) FG-layer (W75% layer) from the cross-section view.

The indentations' microstructure is shown in Figure 4.29. There is no micro-crack near the indentations. It seems that tungsten coating and FG-layer have high toughness and sufficient ductility.

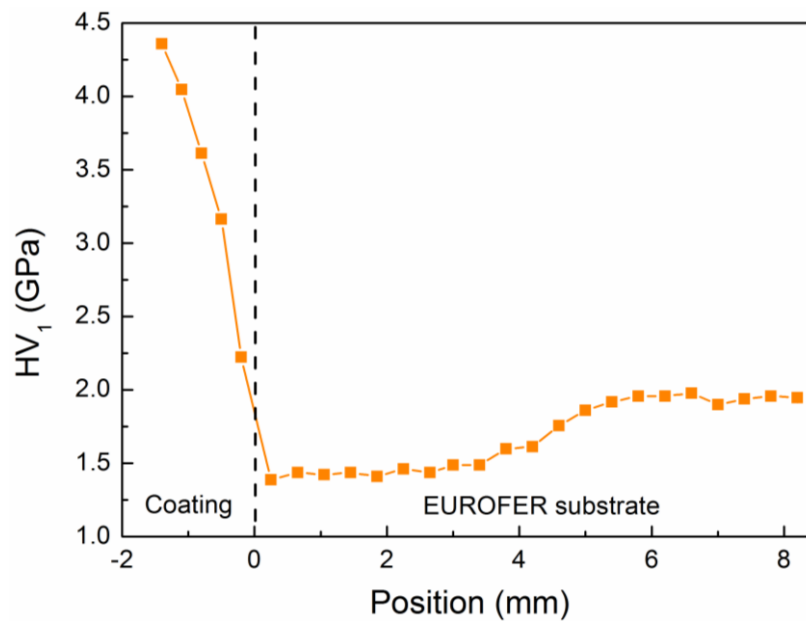


Figure 4.30: Microhardness at different positions of sample 3-T(7).

As already observed in Section 4.4.1, the nanohardness near the substrate interface is lower than that of the as-received EUROFER plate, while the nanohardness at the position away from the substrate interface (> 4 mm) is similar to that of the as-received EUROFER plate. Due to the limit of local properties of the nanohardness measurement and also for a better understanding, microhardness at different positions (from W coating to EUROFER substrate) has been investigated, and is shown in Figure 4.30. The dashed line shows the substrate interface. As it can be seen, a slight decrease of the hardness has been observed when the distance from the substrate interface is less than 4-5 mm. The decreasing of the hardness has also been observed for the other four samples, as shown in Figure 4.31. The microhardness of EUROFER plate [29] is shown by green dashed line as a reference. The depth with reduced hardness for the substrate of sample 3-T(5) is similar to that for the sample 3-T(7), while the affected depth of sample 5-T(7) is a little deeper to about 10 mm, and it even expands to the whole thickness for the samples 3-T(3) and 5-T(5).

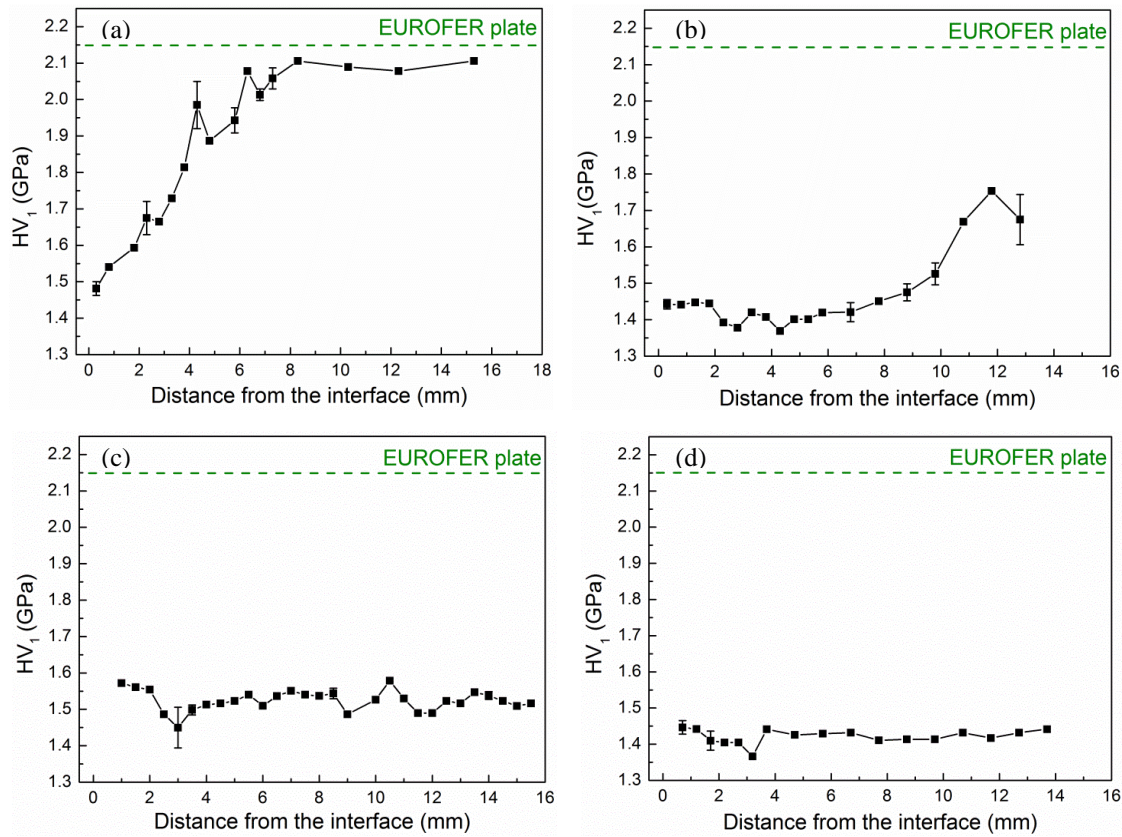


Figure 4.31: Microhardness versus the distance from the interface of sample: (a) 3-T(5); (b) 5-T(7); (c) 3-T(3) and (d) 5-T(5).

To understand the changes of substrates, the BSD microstructure of sample 3-T(7) has been investigated and is shown in Figure 4.32. The microstructure of the substrate is a typical ferritic/martensitic structure when the distance from the substrate interface is larger than 4 mm. With decreasing distance from the substrate interface, grains start to grow. Moreover, more and more grains grow with decreasing distance until all grains near the interface grow. It is clear that the changes of microstructure lead to the decreasing of the hardness. The growing of grains could be due to the high temperature introduced by the melted particles with high energy since it is hard to control the temperature during thermal spraying. Nevertheless, the change of the substrate should be avoided in further fabrication process by introducing a coolant channel or reducing the preheating temperature. As discussed in Section 4.3.5, the preheated temperature should be in the range between ≈ 600 °C to 760 °C. Since the preheating temperature in the work is proved to be too high, it should be less than 760 °C in the future.

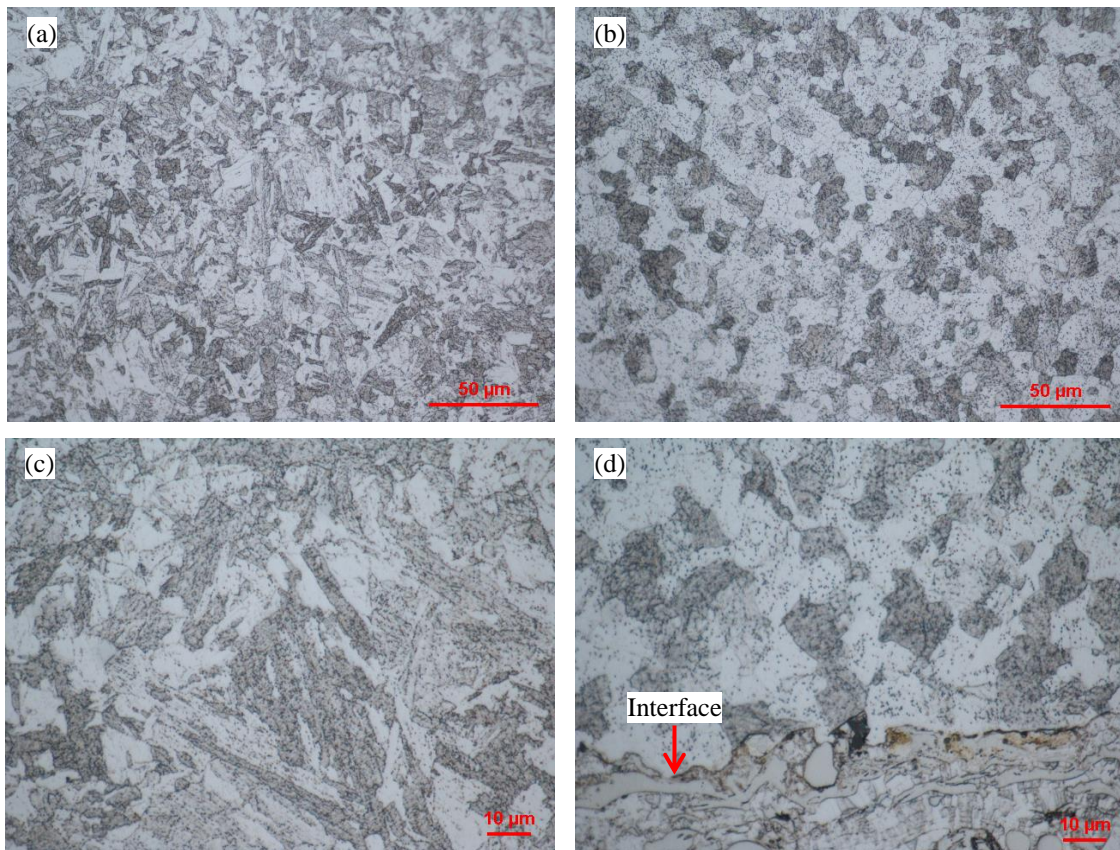


Figure 4.32: Optical microstructure of the sample 3-T(7)' substrate after etching: (a, c) distance from the interface ≥ 4 mm; (b, d) near the interface.

4.4.3 Interface toughness

4.4.3.1 Load-deflection curve

Figure 4.33 (a) shows load vs. deflection curves during three-point bending of the samples 3-T(5), 3-T(7) and 5-T(7). Comparing to a larger loading and unloading rate of two specimens of 5-T(7) (black and red lines of Figure 4.33 (a)), the rate for the other tests is kept equal to $0.2 \mu\text{m/s}$ for obtaining more details during unloading. The geometry effect is also observed obviously. Samples 3-T(7) and 5-T(7) have more or less the same thicknesses of FG-layer and substrates, therefore, the bearing part during the bending test is more or less the same which leads to comparable maximum loads. While the thinner FG-layer of samples 3-T(5) and accordingly thicker bearing substrate result in the largest bending load. Figure 4.33 (b) shows load vs. deflection curves of the sample 3-T(7) during four-point bending.

As it can be seen from Figure 4.33, after the monotonic elasto-plastic increase of the loads, loads drop down from the peak and then keep constant for all specimens. For better understanding, a CCD camera was installed outside the furnace to monitor the specimen through a glass window. Thereby plastic deformation has been observed at the

tip of the pre-crack. Drops of load are directly related to the propagation of the crack as well as new secondary cracks in the FG-layer. The load keeps falling until it becomes constant where the main crack deflects along the substrate interface.

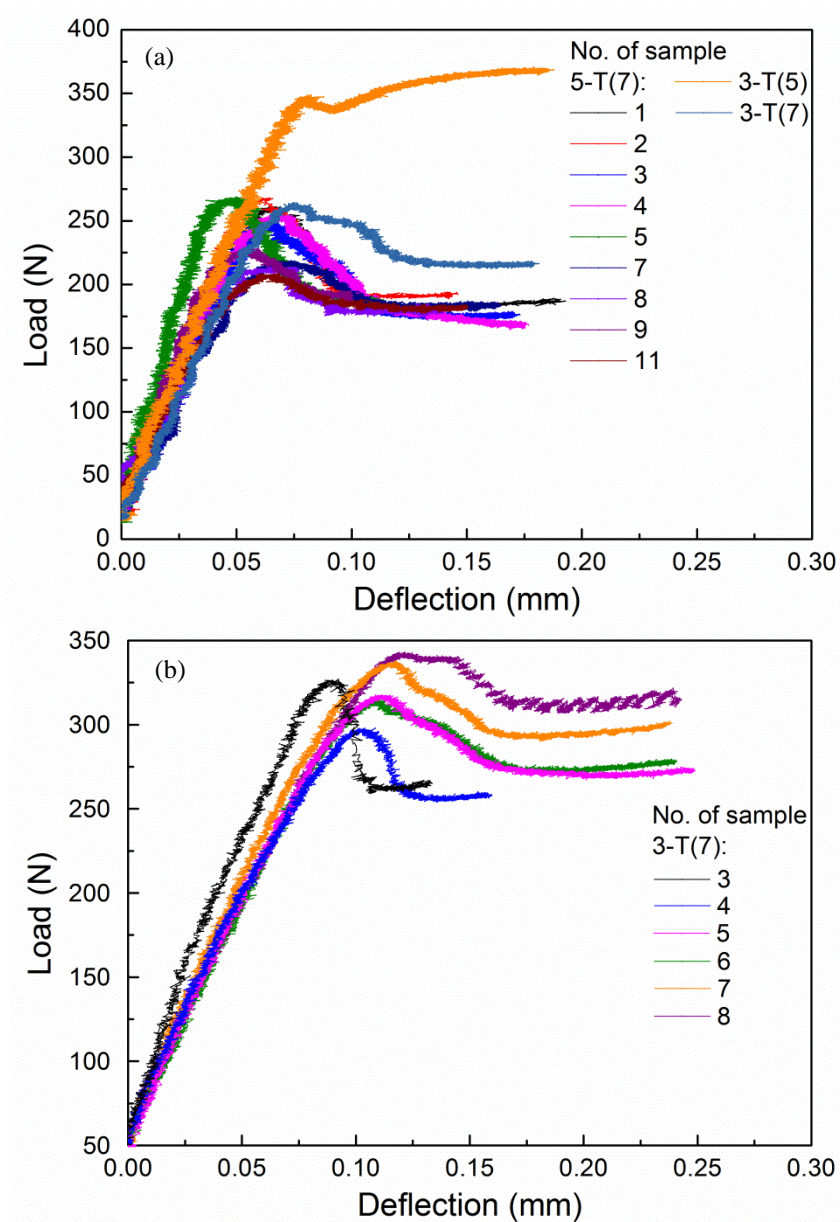


Figure 4.33: Load vs. deflection curve of pre-cracked specimens during three-point (a) and four-point (b) bending tests.

Load gradually drops at one two or three stages with nearly constant rate in each stage. Comparing the position of the pre-crack tip for each specimen, the cases with more than one dropping rate occur mostly for specimens with the pre-crack tip in the FG-layer that the concentration of tungsten is less than 50%. This is because the FG-layer with the concentration of tungsten less than 50% behaves more ductile, therefore the energy required for crack propagation is higher. The propagation of the crack in FG-layer is not

always perpendicular straight to the substrate interface, but accompanied by propagations into small interfaces among the laminar layers with possibly weak bonding strength. This zigzag crack is proven by the video of crack propagation and the optical microstructure of pre-cracked specimen after bending, as shown in Figure 4.34. Nevertheless, cracks propagate through the whole coating system overall. All cracks deflect along the substrate interface, and propagate a certain distance along the substrate interface.

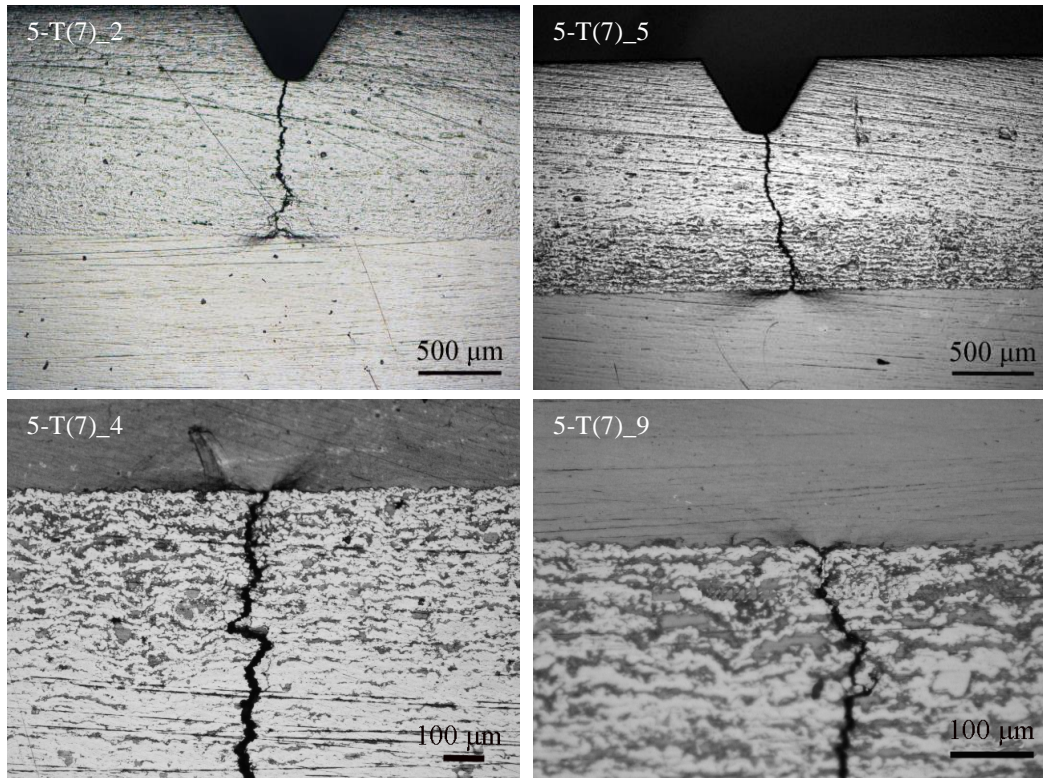


Figure 4.34: Optical microstructure of pre-cracked specimens after three-point bending.

4.4.3.2 Microstructural propagation of crack in FG-layer

Figure 4.35 shows the crack propagation of sample 5-T(7) after three-point bending. A throughout crack propagates in the whole FG-layer, and then it deflects along the substrate interface, as shown in Figure 4.35 (a, b). Details of crack propagation in FG-layer are shown in Figure 4.35 (c). Comparing to the brittle fracture characteristic in W75% (nominal concentration in Vol.-%) layer of FG-layer, crooked shape and plastic fracture characteristics have been observed in the others FG layers. The ductile deformation showed in the red ellipse and delamination pointed out by arrows among laminar interfaces in FG-layer consume the energy of the crack propagation and hinder further propagation of the crack in the failure direction.

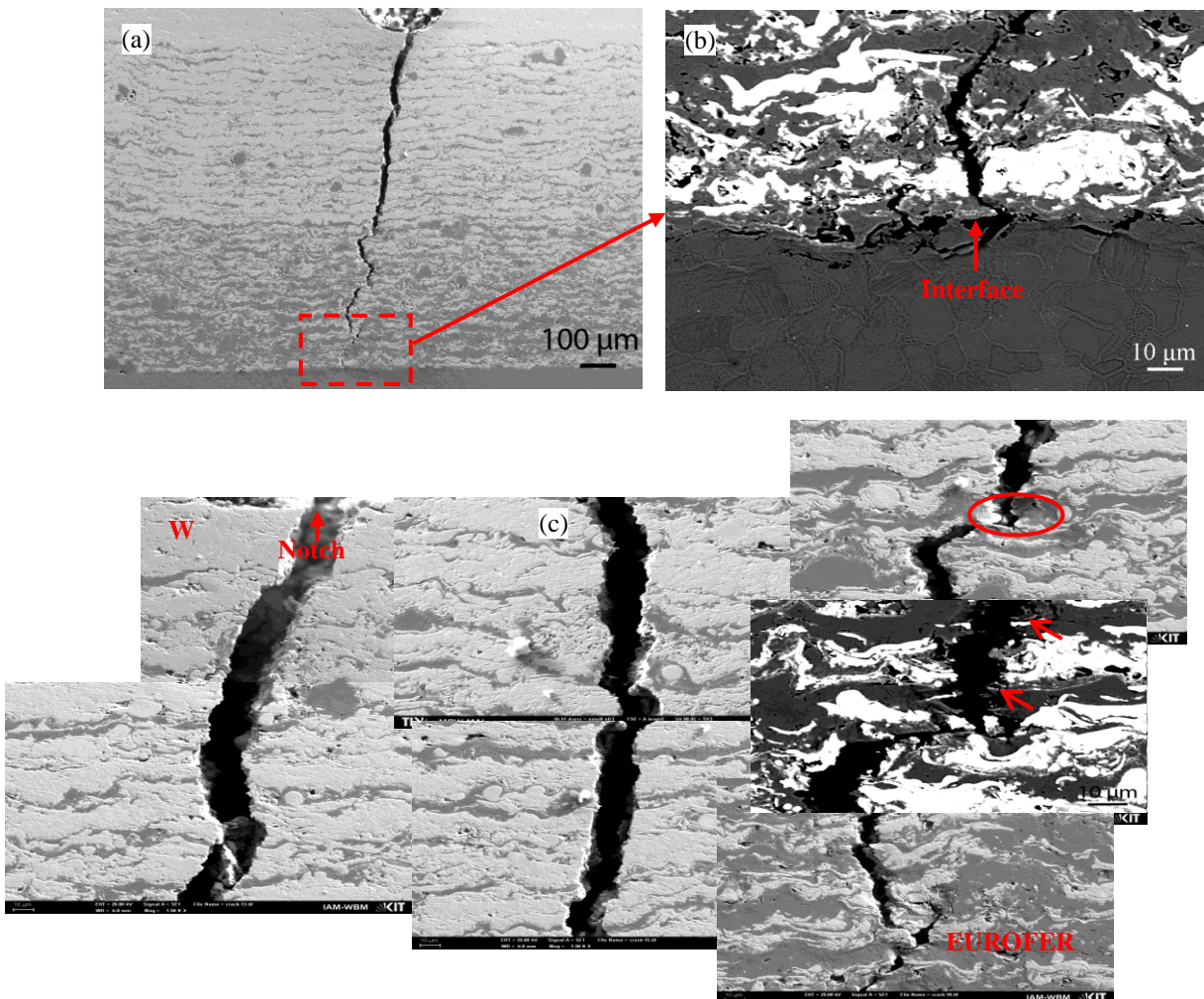


Figure 4.35: The crack propagation within FG-layer (a, c) and along the substrate interface (b) of sample 5-T(7) after three-point bending.

The fracture microstructure inside the FG-layer is observed and showed in Figure 4.36. As it can be seen, the fracture surfaces are rough and uneven. The delamination among laminar interfaces showed in the cross-section microstructure is much clearly observed in Figure 4.36 (b). In addition, there are a vast amount of plastic deformation in the FG-layer with the concentration of W25% (e.g. dimples in Figure 4.36 (a)) and intergranular fracture in the FG-layer with the concentration of W75% that is the main fracture mechanism of W in Figure 4.36(c).

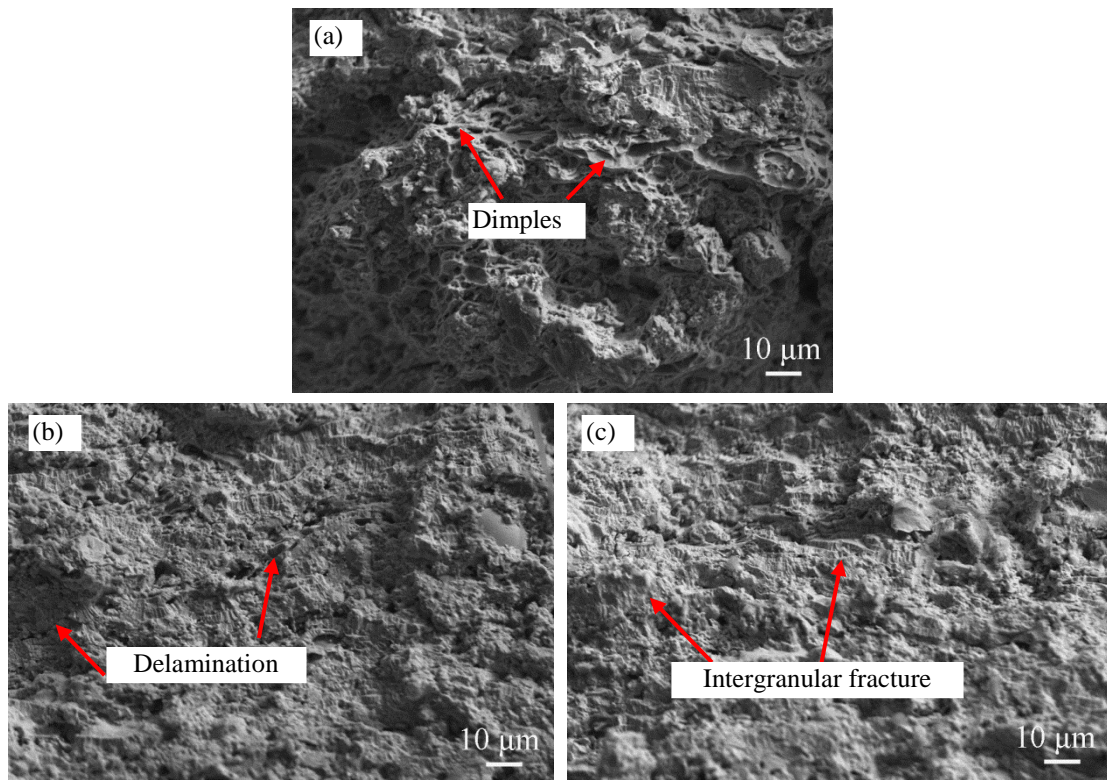


Figure 4.36: Fracture microstructure within the FG-layer with the nominal concentration of W(Vol.-%): (a) 25%; (b) 50%; (c) 75%.

4.4.3.3 Fracture microstructure at the interface

The specimens after bending tests were oxidized at 300 °C for 2h, and then were broken in liquid nitrogen for observing the fracture microstructure. Due to the oxidation of fracture surface introduced by bending, the fracture microstructure can be distinguished into two parts by the red line showed in Figure 4.37 (a). As shown in Figure 4.37 (b), the ductile fracture characteristic is observed at the coating-side interface. Both brittle and ductile fracture characteristics are observed at the substrate-side interface, as shown in Figure 4.37 (c) and (d). There are few cleavage fractures due to the mechanical interlocking interface. Many microporous formed in the initial state of ductile fracture indicate the metallurgic bonding at the interface.

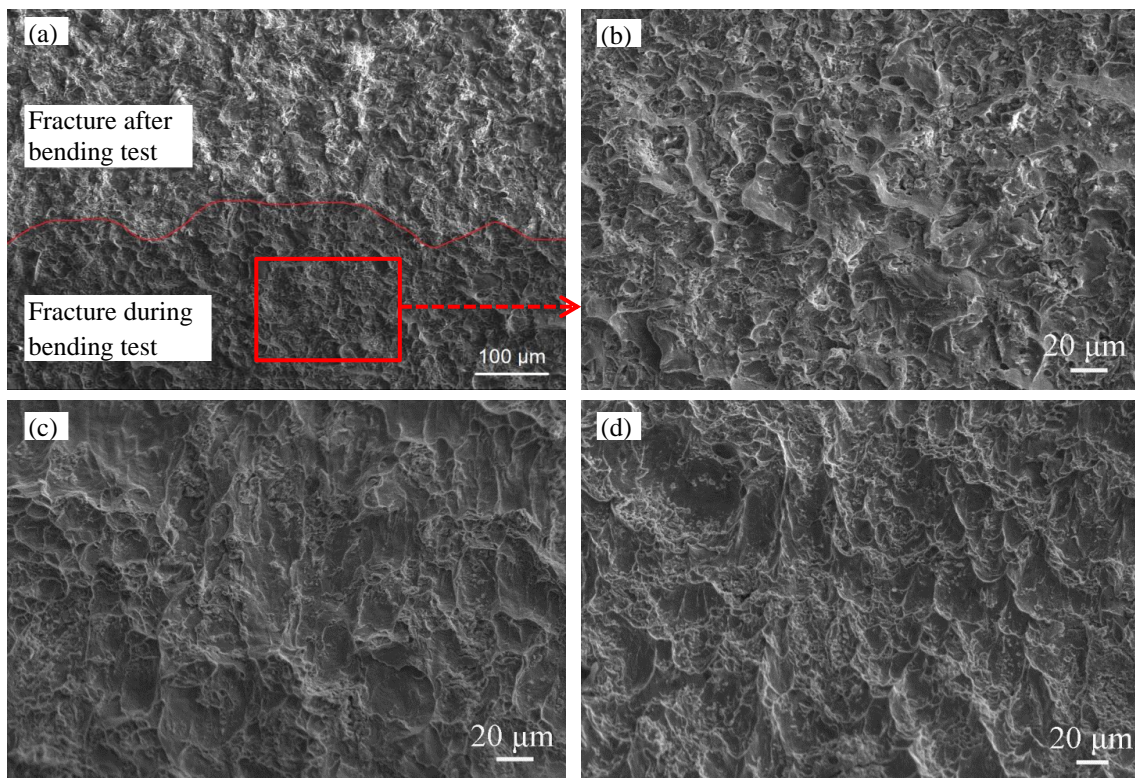


Figure 4.37: Fracture microstructure at the interface: (a) and (b) coating-side; (c) and (d) substrate-side interface.

4.4.3.4 Interface toughness

The interface toughnesses of FG W/EUROFER coating system with the same nominal thickness of FG-layer and two layer numbers are investigated by performing three- and four-point bending tests, respectively. Table 4.2 shows the measured data of specimen dimension, crack length and the load of the platform observed in the load-deflection curve. According to the calculated method introduced in Section 3.3.4, material properties including Young's modulus, Poisson ratio and stiffness of the coating system and the composite beam are calculated firstly. Then the energy release rates of the sample 3-T(7) and 5-T(7) are calculated by the equation (3.22) and concluded in Table 4.2 (a) and (b), respectively. The calculated energy release rate of each specimen from the same sample is comparable, and its mean value of samples 3-T(7) and 5-T(7) is 259 and 225 J/m^2 , respectively.

Table 4.2 (a): Interface toughness of sample 3-T(7) calculated based on three-point bending tests

No. of specimen	87-2	87-3	87-4	87-6	87-7	87-8	New 87-1
h_1 (mm)	1.27	1.26	1.25	1.27	1.28	1.28	1.26
h (mm)	3.94	3.93	3.91	3.92	3.91	3.92	3.94
B (mm)	3.01	3.01	3.01	2.98	2.99	3	3.01
P_c (N)	197.59	205.14	171.43	188.51	186.97	205.56	221.14
a_c (10^{-3} m)	0.49	0.33	0.26	0.27	0.13	0.28	0.28
G_c (J/m^2)	252.30	277.61	194.65	240.80	239.65	282.19	326.08

Table 4.2 (b): Interface toughness of sample 5-T(7) calculated based on three-point bending tests

No. of specimen	103-2	103-3	103-4	103-5	103-7	103-8	103-9	103-11
h_1 (mm)	1.42	1.38	1.41	1.40	1.40	1.39	1.39	1.40
h (mm)	3.96	3.96	3.95	3.95	3.96	3.97	3.97	3.96
B (mm)	3.01	3	2.98	2.98	2.96	2.96	2.97	2.97
P_c (N)	191.35	176.44	173.67	189.58	183.42	179.42	191.05	181.27
a_c (10^{-3} m)	0.21	0.05	0.56	0.14	0.21	0.08	0.04	0.29
G_c (J/m^2)	239.32	209.26	190.04	241.24	227.38	222.39	251.98	217.71

As analyzed in Section 3.3.4, the steady-state energy release rate is assumed during four-point bending. For sample 3-T(7) with the certain λ , the dependence of the energy release rate is determined on the thickness ratio. The dimension and the thickness ratio of each specimen are given in Table 4.3, by substituting the critical load and the geometry data, the energy release rate is calculated based on the formula (3.23), and they are summarized in the Table 4.3. The mean value of the energy release rate for samples 3-T(7) is 257 J/m².

Table 4.3: Interface toughness of sample 3-T(7) calculated based on four-point bending tests

No. of specimen	87-3	87-4	87-5	87-6	87-7	87-8
B (mm)	2.93	2.94	2.95	2.98	2.95	2.92
h (mm)	3.87	3.86	3.9	3.88	3.92	3.90
h ₁ (mm)	1.22	1.19	1.20	1.19	1.21	1.18
h ₁ /h ₂	0.463	0.447	0.445	0.442	0.447	0.435
$\frac{E_2 G_{ss} h^3 b^2}{P^2 l^2 (1 - \vartheta_2^2)}$	3.548	3.395	3.376	3.348	3.395	3.282
P _c (N)	262.03	255.82	271.27	272.85	293.24	312.01
G _c (J/m ²)	244.15	222.89	240.00	239.63	277.73	315.04

The interface toughnesses of two FG W/EUROFER coating systems are compared in Figure 4.38. The mean toughness of the coating system with five layers is 225 J/m², which is about 13 % lower than that of the coating system with three layers. Nevertheless, the toughnesses of the same coating system measured by three- and four-point bending tests respectively are comparable quite well. Many works have been done on investigating the effect of phase angle on interface toughness, in general, the energy release is expected to be lower when the phase angle is small [93, 107-109]. The phase angle is related to the thickness ratio of the beam and the residual stress [110]. The larger the thickness ratio, the lower the phase angle [93]. The phase angle is nominally 35°- 60° during four-point bending tests [95]. The thickness ratio h_1/h_2 for sample 5-T(7), sample 3-T(7)_3-Pb and sample 3-T(7)_4-Pb are 0.546, 0.477 and 0.447, respectively. The larger thickness ratio represents that the shear load is smaller, therefore, the phase angle is smaller. The smaller phase angle of sample 5-T(7) leads to the lower energy release rate.

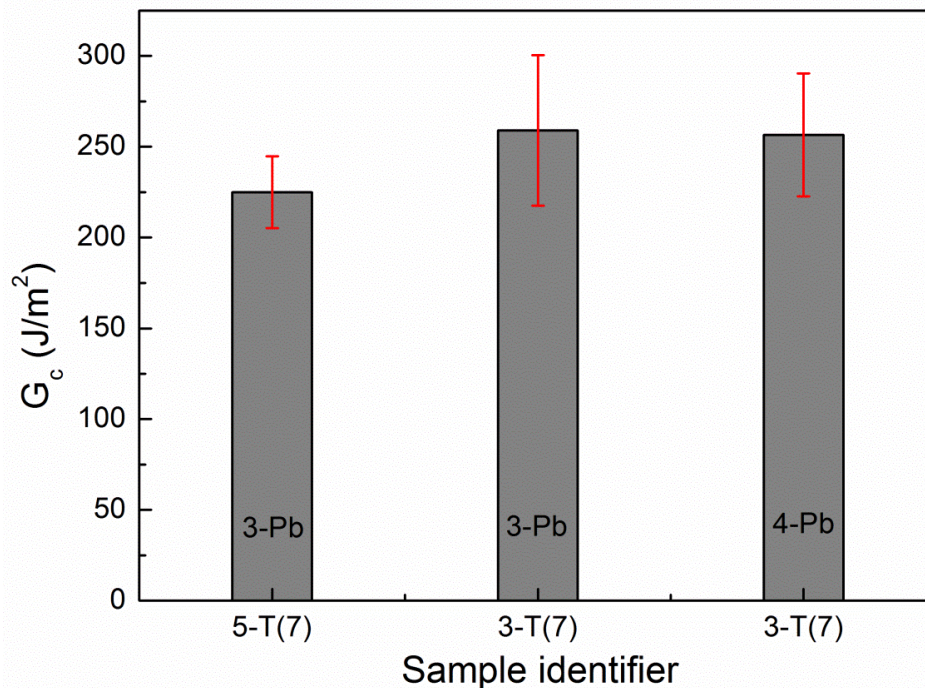


Figure 4.38: Comparison on interface toughness of two coating systems.

The energy release rate calculated in the work based on the beam theory (three-point bending) and the analytical method of Charalambides (four-point bending) are only considered an elastic solution. In the case of the calculation method based on the beam theory, the stiffness of the substrate is used for calculating the energy release rate when the crack starts to deflect along the interface. While the crack propagates a certain length along the interface and the consumed energy of this process aren't considered and calculated. For the case of the analytical method of Charalambides, the energy release rate is evaluated for a brittle system by considering a plane strain and small-scale yielding condition. However, the vast plastic deformation and the ductile fracture surface are observed at the platform of the load-deflection curve that is related to the propagated crack along the interface. Therefore, the consumed energy during the propagating of the interface crack in FG W/EUROFER coating system should be much higher than the energy release rate calculated in this work. Nevertheless, the interface toughness of FG W/EUROFER coating system calculated in the work is still reasonable since it is very complex to calculate the interface toughness of bimaterial material system, particularly for the coating system with FG-layer and both brittle coating and ductile substrate. FE simulation may be a feasible solution to start with the precise determination of interface toughness for FG W/EUROFER coating system.

The comparison of interface toughness among the FG W/EUROFER coating system and the other systems [93, 95, 96, 111] is concluded in Figure 4.39. As it can be seen, the interface toughness of the different systems varies by two orders of magnitude.

Except the SiC/C/SiC performed by three-point bending tests, the other systems' interface toughness is measured by performing four-point bending tests. The phase angle introduced by the different measured methods is assumed to be neglected. The fabricating methods are marked in Figure 4.39. The systems (FG W/EUROFER coating system and B₄C coating on a Ti-6Al-4V substrate) fabricated by VPS show high interface toughness comparing to the systems fabricated by sintering and tape casting. The fabricated method plays a key role in the interface quality, and may affect the interface toughness. However, the most prominent difference among them is the typical elastic characteristic of the others systems, specifically, the load-deflection curves of the others systems show that the load drops suddenly due to burst of crack and load keeps increasing instead of the platform observed for FG W/EUROFER coating system. A good interface toughness of FG W/EUROFER coating system is shown by a rough comparison, while the real interface toughness should be even higher as discussed earlier.

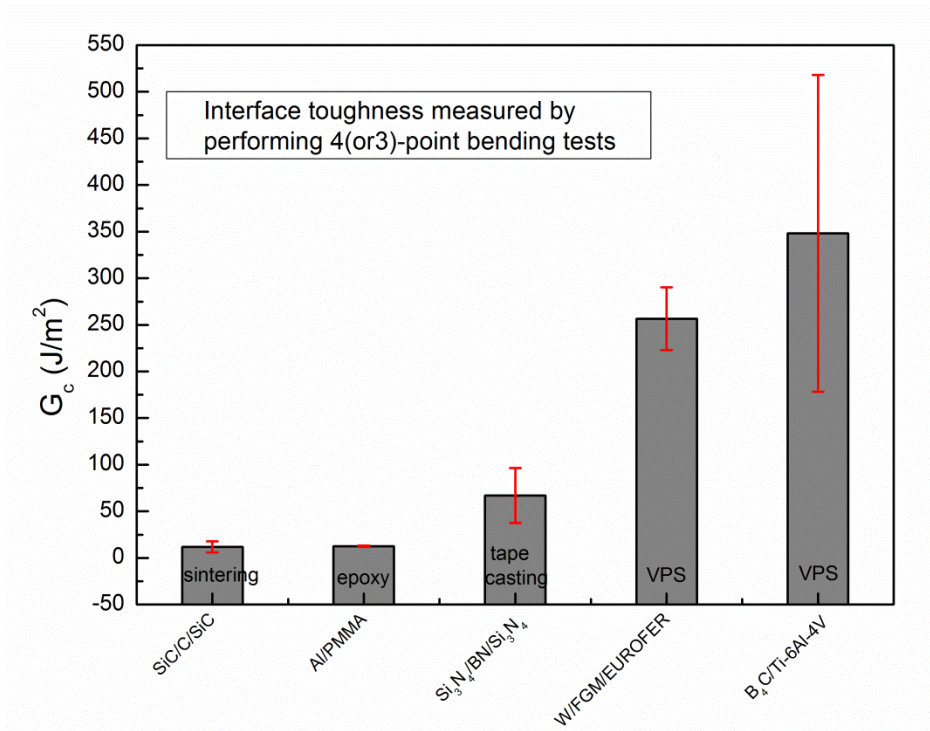


Figure 4.39: Comparison on interface toughness among FG W/EUROFER coating system and the others systems.

4.4.4 Thermal load resistance analysis

4.4.4.1 Thermal shock tests

4.4.4.1.1 Exposed surface morphology

Figure 4.40 shows the surfaces exposed to the power density of 0.19 GW/m^2 at the base temperature of RT and $550 \text{ }^\circ\text{C}$. There is no surface damage for all five samples no matter at RT or $550 \text{ }^\circ\text{C}$. While a dense crack network is observed on exposed surfaces when the power density is increasing to 0.38 GW/m^2 for all five samples, taking sample 3-T(3) showed in Figure 4.41 (a) as an example. Typical primary and secondary cracks induced by thermal shock test are observed, as showed in Figure 4.41 (b). The magnifications of primary cracks in Figure 4.41 (c, e and f) show that the width of the primary crack is in a range of $1.5\text{-}3 \text{ }\mu\text{m}$, and they are most likely formed due to the brittleness of the material in the first few shots. The temperature of the exposed surface can increase several hundred Kelvin in the thickness range of several tens of micrometers, then an irreversible swelling (up to a few micrometers) and a roughening of the surface can be detected during cooling down. The increasing range of temperature (several hundred Kelvin) is calculated based on the heat-diffusion equation for undamaged bulk tungsten. However, for the damaged surface, the temperature could be quite high due to the reduction of the thermal conductivity. For instance, the temperature of recrystallized tungsten exposed to 0.38 GW/m^2 heat load could be up to $\approx 2500 \text{ }^\circ\text{C}$ based on FE simulations [112]. Obvious surface roughening is shown in Figure 4.41 (c), even partially melting occurs at the crack edge in Figure 4.41 (d).

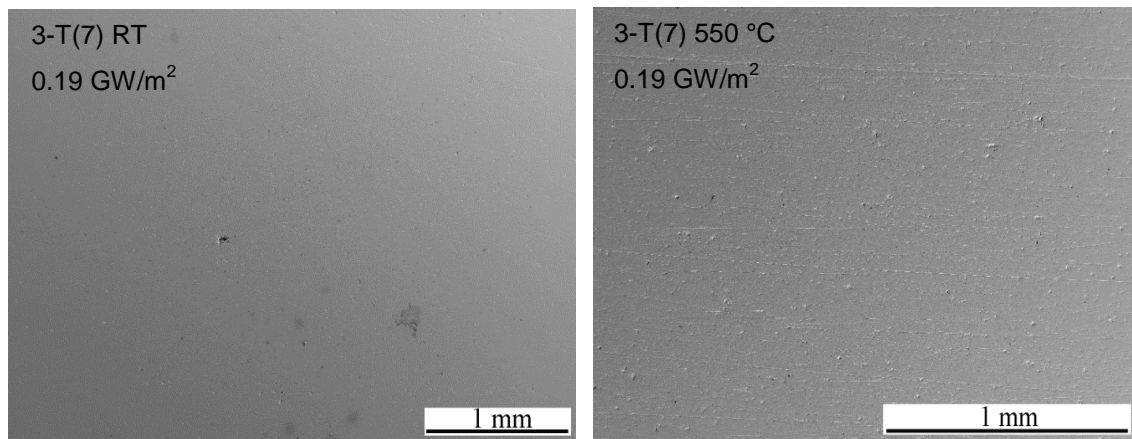


Figure 4.40: The surface exposed to the power density of 0.19 GW/m^2 at RT and $550 \text{ }^\circ\text{C}$ [113].

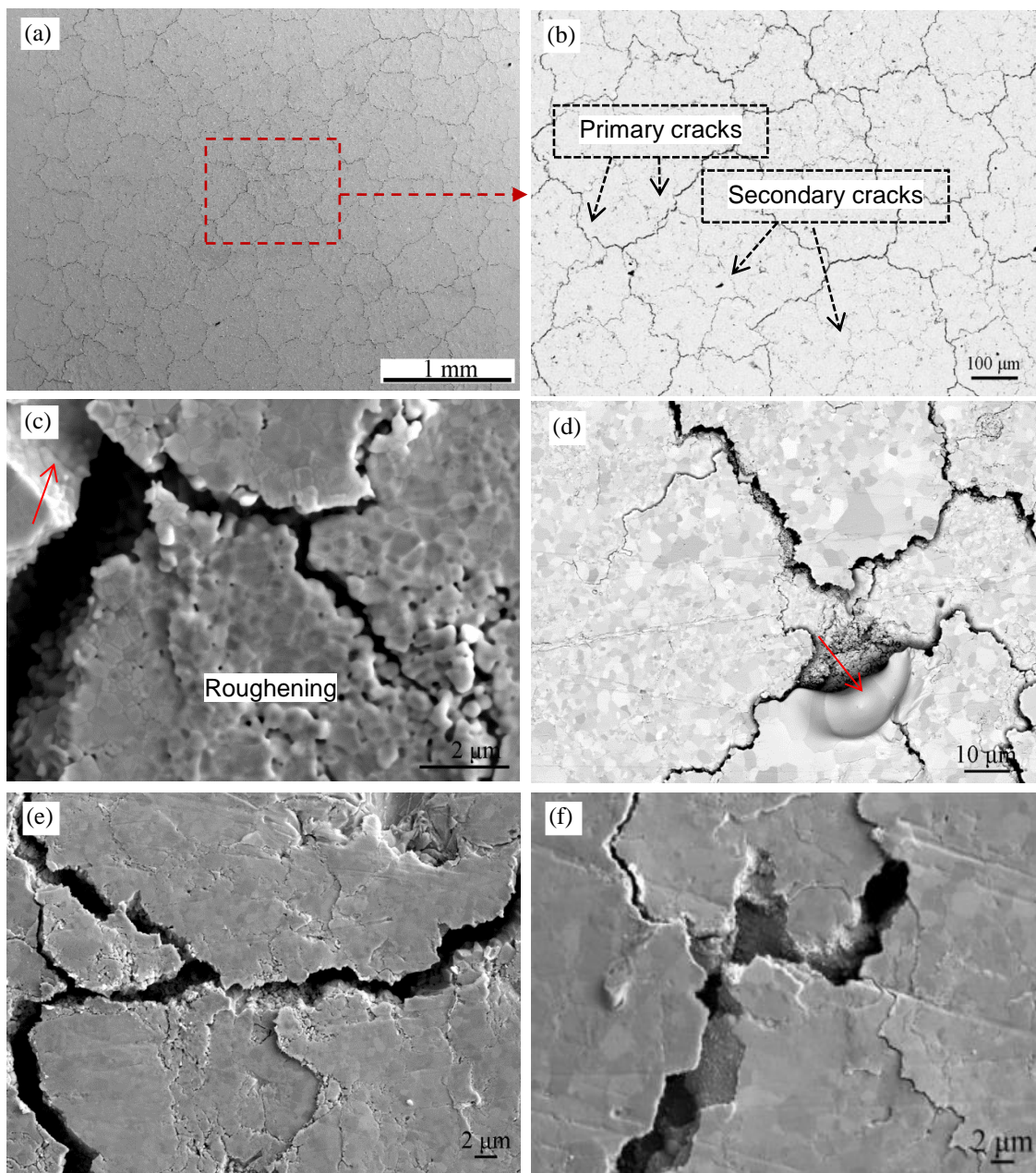


Figure 4.41: The surface damages exposed to the power density of 0.38 GW/m^2 at RT: (a, b) crack network of sample 3-T(3); (c-f) magnification of cracks of sample 3-T(3), 3-T(5), 3-T(7) and 5-T(7), respectively [113].

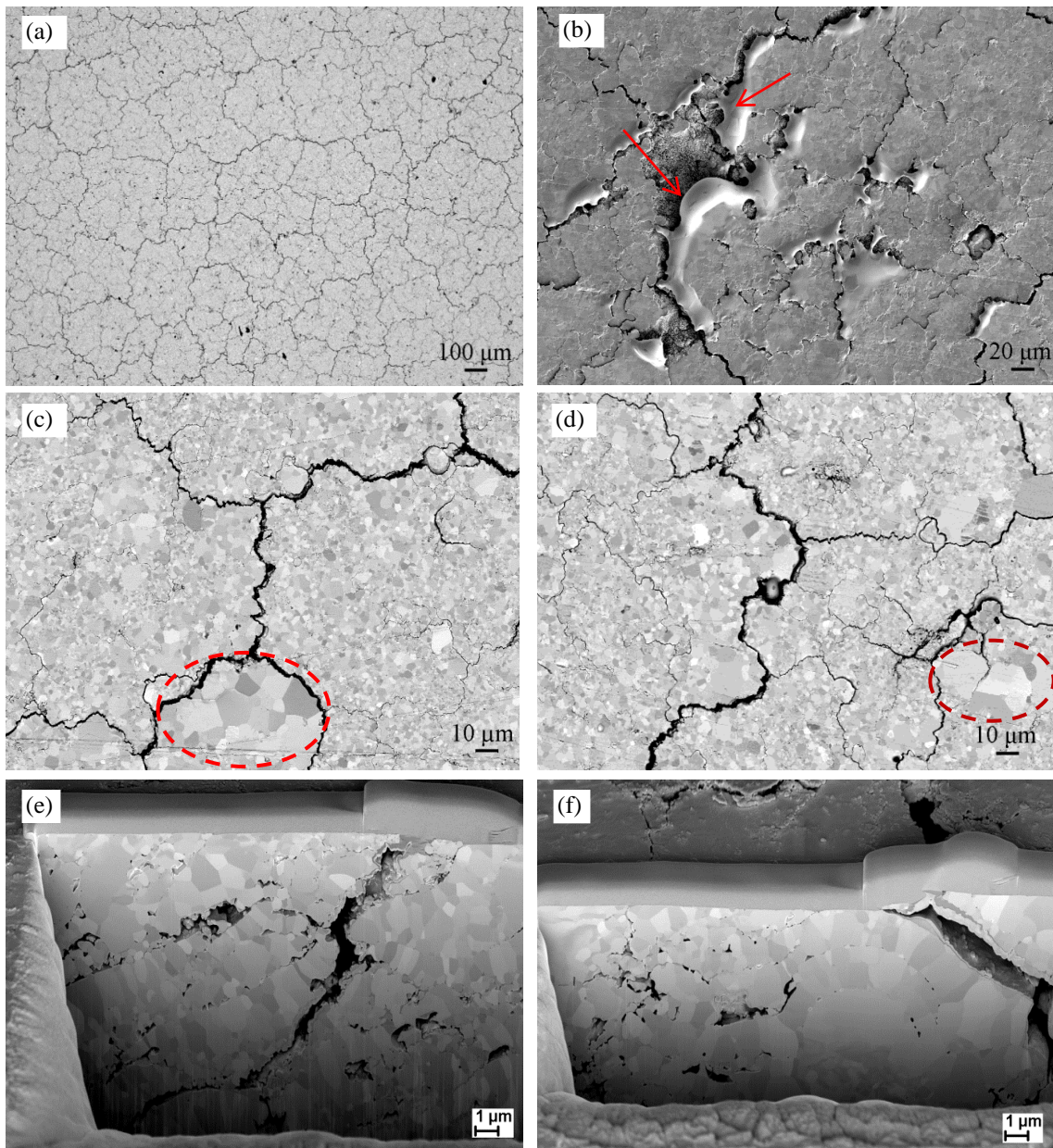


Figure 4.42: The surface damages exposed to the power density of 0.38 GW/m^2 at 550°C : (a) crack network of sample 3-T(3); (b) melted edges of sample 5-T(5); (c, d) grew grains of 3-T(5) and sample 5-T(5), respectively; (e, f) cracks under the surface of sample 3-T(5) [113].

As shown in Figure 4.42, a denser crack network is observed for the surfaces exposed to absorbed power density of 0.38 GW/m^2 at 550°C comparing to that at RT. The primary and secondary cracks are also observed, as shown in Figure 4.42 (a). The growing of grains is also observed around the crack edge, as shown in the red dotted line of Figure 4.42 (c, d), which is due to the overheating of a local area. The propagation of cracks under the surface is observed by FIB cutting, as showed in Figure 4.42 (e, f). The crack propagates initially perpendicular to the loaded surface into the sample, and then deflects to the parallel direction to the loaded surface at a certain depth. This extending

path of cracks leads to the overheating of a local area. Severe overheating can even introduce melted edges, as shown in Figure 4.42 (b).

4.4.4.1.2 Crack characteristic

The adjacent primary crack distances are measured on five samples' surfaces exposed to 0.38 GW/m^2 at RT and $550 \text{ }^\circ\text{C}$. The crack distances at RT are in the range of $400 - 500 \text{ }\mu\text{m}$, and they are higher than that at $550 \text{ }^\circ\text{C}$. The reciprocal of the adjacent crack distance is defined to be the crack density. Figure 4.43 shows crack density exposed to the power density of 0.38 GW/m^2 . The crack density at $550 \text{ }^\circ\text{C}$ decreases with FG-layer thickness firstly, and then drops down to a constant value when FG-layer thickness is greater than or equal to 0.7 mm . Since the effect thickness under the exposed surface is only in the range of several tens of micrometers, which means the effect zone remains in the W coating for the five samples. Therefore, the influence of FG-layer's thickness on crack density is assumed to be owing to the reduction of residual stress in W coating, specifically, the thicker the FG-layer, the less residual stress in W coating. The influence of stress state on thermal shock resistance of recrystallized tungsten is discussed in [114]. Except the residual stress in W coating, the temperature and strain rate also affect the crack density [40]. The crack density exposed to 0.38 GW/m^2 at $550 \text{ }^\circ\text{C}$ is higher than that at RT. The widths of primary cracks are in the range of $1.5 - 3 \text{ }\mu\text{m}$.

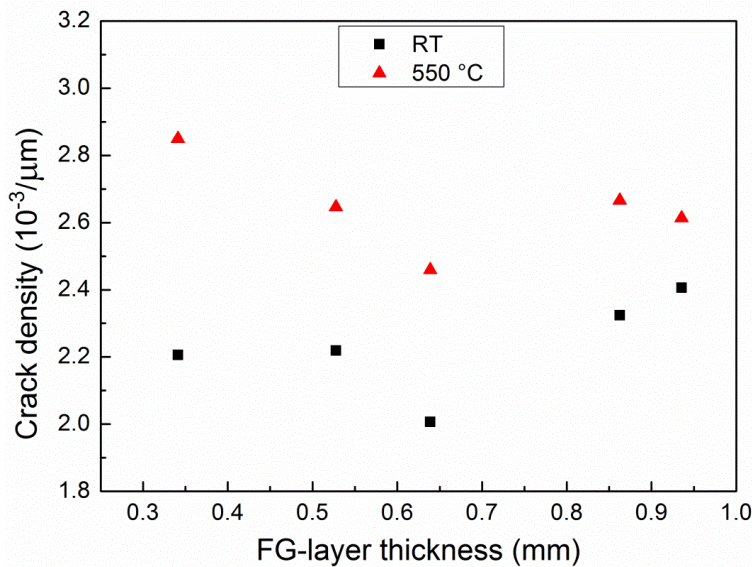


Figure 4.43: Crack density exposed to the power density of 0.38 GW/m^2 at the base temperature of RT and $550 \text{ }^\circ\text{C}$, respectively.

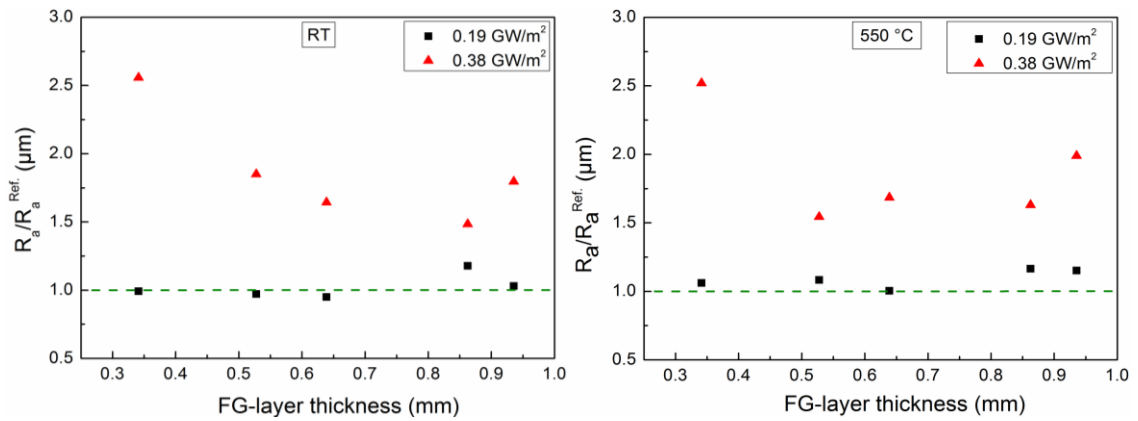


Figure 4.44: Roughness comparison before and after exposing to the power density of 0.19 and 0.38 GW/m^2 at the base temperature of RT and 550°C.

The Y-axis in Figure 4.44 is defined by the ratio of exposed surface's roughness divide by as-received surface's roughness. The roughness ratio is almost equal to 1 for the surfaces exposed to the low power density at both temperatures, which means no surface damage. While for the surfaces exposed to the high power density, it is more than 1 due to the surface roughening and cracking. In addition, it decreases with the increasing thickness of FG-layer at both temperatures, particularly when The FG-layer thickness is greater than or equal to 0.7 mm. According to the analysis of microstructure and crack characteristic, the damage threshold of the coating system is determined, and it is in the range of 0.19 and 0.38 GW/m^2 , as shown in Figure 4.45.

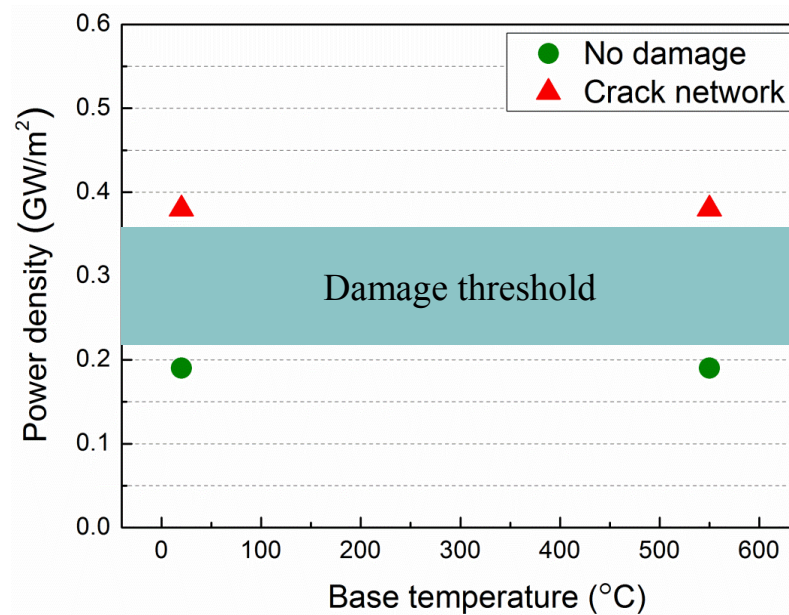


Figure 4.45: Thermal shock response of the coating system after 100 thermal shock events at different power densities and base temperatures.

4.4.4.1.3 Crack forming theory

The theoretical formation reason of cracks induced by thermal shock tests is the tensile stresses during the cooling process. Specifically, due to the high heat flux, the temperature in a thin layer under the loaded surface could increase in a range of several hundred to 2000 °C [115], thereby crossing the material's DBTT. Then the thermal induced expansion and the plastic deformation of the thin layer occur irreversibly due to compressive stresses. When the temperature becomes the initial value, the plastic deformation and the volumetric shrinkage take place due to tensile stresses. The tensile stresses lead to the formation of cracks [42]. In Ref. [116] one heating-cooling cycle is subdivided into five stages. The three conditions of crack formation are concluded as following: The first condition is that the temperature increases and reaches the DBTT (200 - 400 °C for pure tungsten) [117]; The second condition is that the maximum value of the plastic stress exceeds the ultimate tensile strength with the increasing temperature. When cooling begins, complete stress that consists of elastic and plastic ones reverses its sign, and the reversed complete stress causes tensile plastic deformation. Once the temperature becomes lower than the DBTT, the complete stress rises above the yield strength of the brittle material. Then cracks form when the stress is larger than the ultimate tensile stress. Comparing to RT, worse performance at 550 °C is related to the lower yield strength of tungsten at higher temperatures, which leads to stronger plastic deformation.

4.4.4.2 Thermal fatigue tests

The value of crack width multiplied by crack area or crack propagation rate per cycle are nominally used to assess the thermal fatigue resistance of the material [118, 119]. However, there is neither macro nor micro visible crack on sample 3-T(3) and 5-T(7) after 500 thermal cycles. Figure 4.46 shows microstructures of sample 3-T(3) after each 100 thermal cycles. Due to time consuming of thermal fatigue tests, the maximum cycle number in the work is as large as half of designed cycle number for DEMO application. The coating system shows a promising thermal fatigue resistance. The similar investigation is performed for W coating on EUROFER substrate [47]. There is no damage under heat load tests with steady state operation up to 2.5 MW/m² and cycling (720 cycles) heat loads of 2 MW/m². The porous structure is considered to constrain the propagation of cracks or fissures.

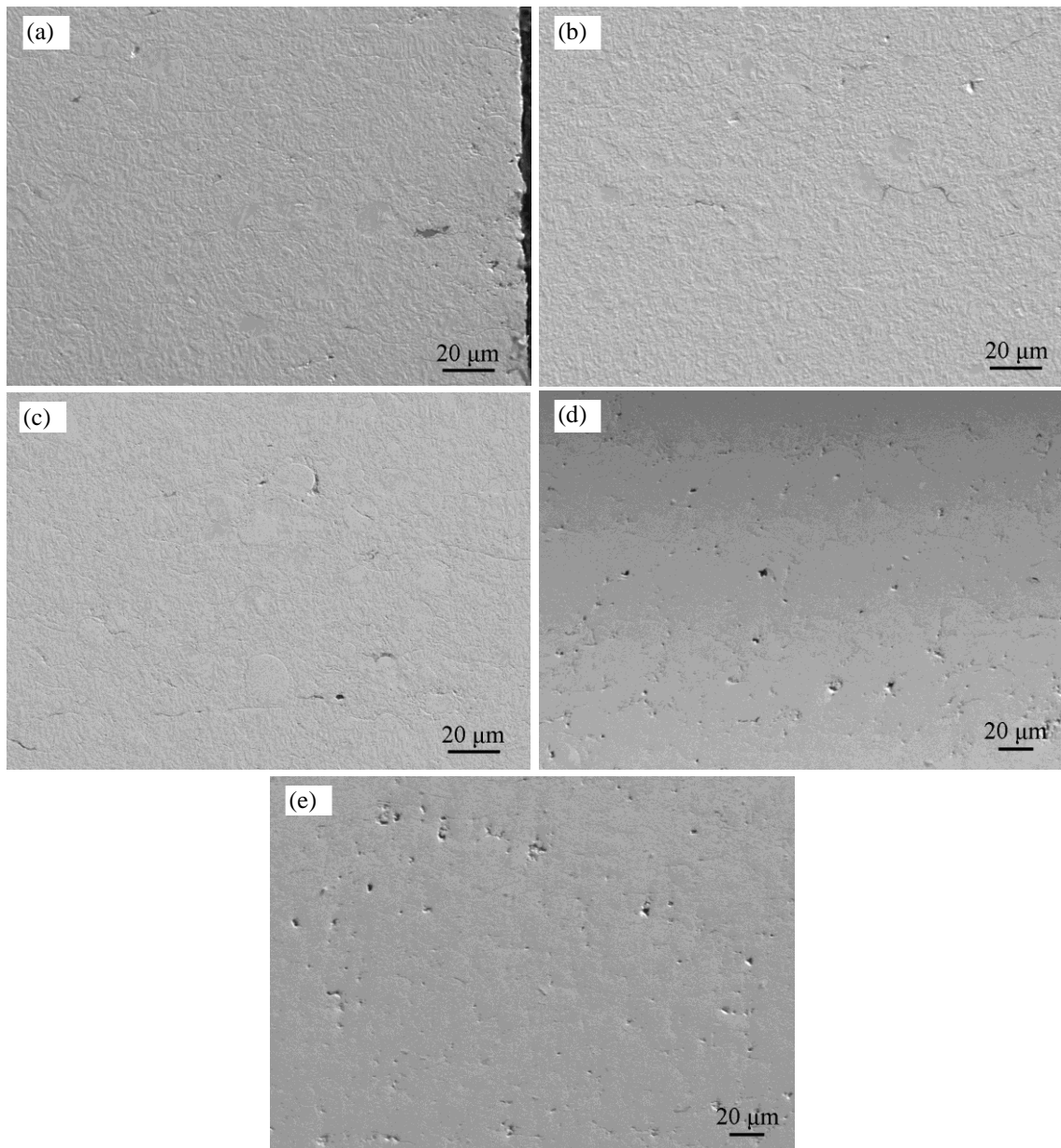


Figure 4.46: Microstructures of sample 3-T(3) after: (a) 100 cycles; (b) 200 cycles; (c) 300 cycles; (d) 400 cycles; (e) 500 cycles.

Micro-hardnesses are investigated after each 100 thermal cycles. Figure 4.47 compares the micro-hardnesses of the samples after each 100 thermal cycles with the as-received sample. As it can be seen, micro-hardness of tungsten coating after thermal fatigue tests decreases comparing to that of the as-received tungsten coating. The higher hardness of as-received tungsten coating is contributed by the high compressive residual stress observed in the FE-simulation. The compressive stress releases after 100 cycles or even only the first few cycles, which leads to a reduction of the hardness. But only a slight scatter of micro-hardness is observed among different thermal cycles. Non-obvious dependence of hardness on thermal cycles is owing to the high thermal fatigue re-

sistance. In addition, an unchanged micro-hardness is observed for the EUROFER substrate. Thermal fatigue tests show no impact on the substrate.

Small cracks are observed around indentations on samples after thermal fatigue tests. As shown in Figure 4.48, small cracks are normally along the laminar interfaces, but not along diagonals of indentations. It could be owing to the sliding and breaking among laminar interfaces under the thermal fatigue tests. This is also discussed in [120], where the sliding and breaking of the bonds among laminar splats lead to the decreasing of apparent Young's modulus. Whereby the apparent Young's modulus of YSZ top coating is determined by bending tests after exposed to thermal fatigue tests. The promising thermal fatigue resistance of the coating system benefits from the sliding and breaking of the bonds since they seem to accommodate the inelastic strain induced by thermal fatigue tests.

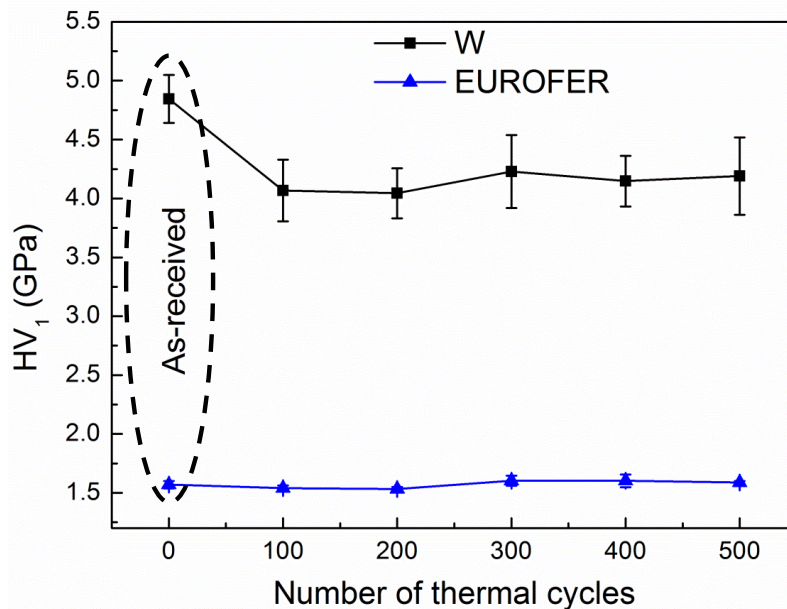


Figure 4.47: Comparison on microhardnesses of the samples after thermal fatigue tests with the as-received sample.

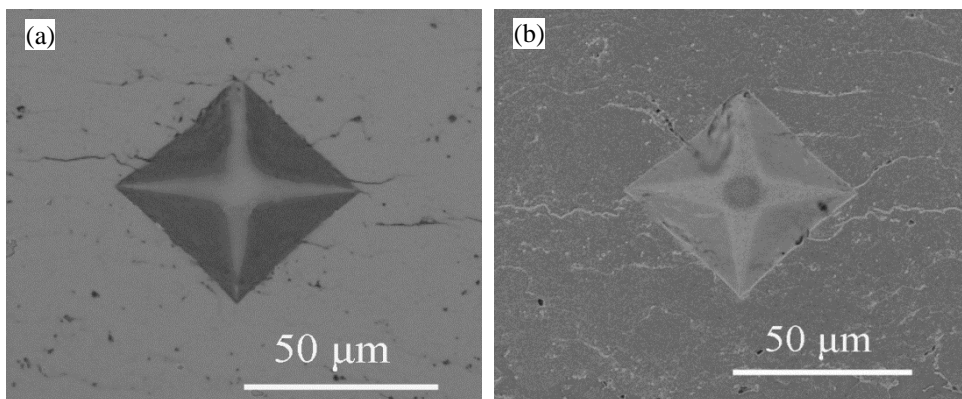


Figure 4.48: Small cracks around indentations on samples after (a) 400; (b) 500 thermal cycles.

4.4.5 Discussion and conclusion

4.4.5.1 Effect of FGM on residual stress

As discussed in section 2.1.3, the application of FGM could bring a gradient CTE, and then benefit the reduction of residual stress, which is proven by FE simulation in Ref. [20, 52-54]. Two and four stepwise linear layers, linear and quadratic gradient [52] have been simulated for the helium-cooled divertor design developed at KIT [53]. Elastoplastic and elastic-viscoplastic simulations have been performed under the variation of the layer thickness, layer orientation and gradient function. The resulting stresses and strains are used as the basis for the subsequent lifetime estimation. The performed FE-simulations show that a functionally graded joint between tungsten and EUROFER can drastically decrease the thermal mismatch stresses and strains occurring in the divertor component and thus improve its failure behavior during thermal cycling. Similar work simulating bi-layer (no interlayer), an interlayer (one layer), 5-layer, 11-layer with linear gradient and 11-layer with parabolic gradient ($n=2$) between tungsten coating and Diamalloy steel has been performed [20]. The main conclusion includes that a reduction of stress across the interface with increasing compositional graduation, and a reduction of stored strain energy which is the driving force of the coating delamination, have been observed within the coating and particularly at the interface by introducing FGM, especially for the FE-model with a linear compositional gradient.

The linear gradient of FGM behaves well in both simulations, and stepwise layers with linear gradient are feasible considering the fabrication processes. Therefore, the gradient of FG-layer is kept to be linear for the FE-simulation. By considering proper material behavior, boundary condition and load condition of FW application, the distribution and quantity of the residual stress as a function of the FG-layer thickness, as well as the lifetime, are evaluated and discussed in this work. The reduction of stress and equivalent plastic strain in W coating and the rearrangement of stress in the whole sample by the application of FG-layer have been discussed in section 4.1. The thicker of FG-layer, the better of the effect on the reduction of residual stress as long as the thickness is below 4 mm. The maximum thickness is determined to be 4 mm due to the plastic deformation induced by the tensile residual stress in EUROFER substrate. The lifetime of the coating system has been evaluated according to the operation condition of FW. With the increasing of thermal cycle number, the maximum creep strains are increasing for all investigated thicknesses, but a shake-down of the creep strain is observed for FG-layer with 0.7 mm thickness. The creep strain is negligibly small and independent on number of cycles when the FG-layer thickness is greater than or equal to 1.2 mm. The sufficient FG-layer thickness is 1.2 mm.

4.4.5.2 What benefits thermal load resistance?

After exposing to the same thermal loads with 100 pulses and 1ms duration, the crack thresholds at RT and 550 °C for five samples are between 0.19 and 0.38 GW/m². The crack thresholds are comparable with pure bulk W and W-UHP in Ref. [42]. There are three reasons for good thermal shock resistance of the coating system. The first reason is the low porosity of the coating system (< 4%). The second reason is the microstructure characteristic of the VPS coating including laminar structure and columnar grain. The reduction or re-arrangement distribution of the residual stress is the third reason.

Firstly, low porosity means high density and good thermal conductivity which are beneficial for heat transfer from the loaded surface into the whole sample. The effect of porosity on the crack threshold of W coating is proven in Ref. [46], coatings of APS-W and VPS-W with the porosities of 6% and 0.6 % start to crack at the power density of 0.19 and 0.38 GW/m², respectively.

Secondly, the effect of grain orientation and structure on how crack grows is discussed in Ref. [40]. The longitudinal specimens (grains elongated parallel to the loaded surface) and the recrystallized specimens (heat treated longitudinal specimens) show an arbitrary crack network as the thermal shock crack pattern within the loaded area. The thermal shock cracks of the transversal (grains elongated perpendicular to the loaded surface) follow the grain orientation. The investigation on cross-section microstructure also proves that, the cracks of longitudinal and recrystallized specimens grow perpendicular to the loaded surface into the material and bend to propagate parallel to the surface at a certain depth. However, the cracks of transversal specimen always propagate perpendicular to the loaded surface and grow along the grain boundary. For W/EUROFER coating system, the “grain” orientation is a mixture of longitudinal laminar pancake-like structure and transversal columnar grain. But the cracks follow the longitudinal mode, since small pores among laminar pancake-like structure make laminar interfaces weaker than columnar grains boundary. Even parallel crack to the loaded surface may lead to the overheating of the top thin layer, the columnar grain structure could be helpful to avoid the reduction of thermal transfer and subsequent delamination.

As discussed in Section 2.1.2, several kinds of W coatings behave differently after exposing to different thermal loads. Even thermal shock resistance could be improved by optimizing the coating quality, there is the large residual stress in the coating without any interlayers. This could lead to delamination and severe failure of the whole coating [19]. The tensile stress can lead to the crack according to the crack forming theory. The reduction of residual stress in W coating may release the tensile stress. Particularly when the FG-layer thickness is greater than or equal to 0.7 mm, the reductions of the crack density and the roughness ratio are observed on the loaded sample. Comparing to the samples with three layers as FG-layer, the samples with five layers as FG-layer show a comparable instead of a higher thermal shock resistance as expected.

Since only a slightly smoother gradient is observed for samples with five layers as FG-layer, it seems insufficient to show the advantages of smoother gradient. In addition, the application of FGM reduces the inelastic strain induced by thermal cycles. The less inelastic strain is beneficial for improving mechanical property of the coating system, and then improving the crack threshold.

4.4.5.3 Size effect/The effect of laminar interfaces

The application of FGM is to reduce or rearrange the residual stress induced by the large mismatch of CTE in the coating. The basic idea is that the volume fractions of the constituents vary gradually resulting in a corresponding change in the microstructure and properties of the coating. Therefore, although the huge interface between W coating and EUROFER substrate are avoided by the application of FGM, but it need to be clarified that the small interfaces among laminar structure still exist in FG-layer. The small interfaces improve the fracture toughness of FG-layer since secondary cracks at the small interfaces consume the crack propagation energy and hinder further failure. Moreover, the sliding and breaking among the interfaces accommodate the inelastic strain induced by thermal fatigue test.

5 Summary and outlook

5.1. Summary

The concept of FGM has been introduced to solve the thermal mismatch problem between tungsten armor and EUROFER first wall. FG W/EUROFER coating systems have been investigated and developed theoretically and experimentally in the work. The FG-layer thickness is determined and specified primarily by performing FE-simulation. VPS produced FG W/EUROFER coating systems have three kinds of thicknesses and two kinds of stepwise linear gradients. In the end, the coating quality including microstructural and thermo-mechanical properties has been evaluated as FW application.

Specifically, the FE-simulation considering elastic-perfectly plastic and elastic-viscoplastic behavior of the materials has been performed to simulate the fabrication and operation process. For the fabrication process, a gradient CTE in FG-layer releases residual stresses in the coating system. Moreover, the thicker the FG-layer, the less residual stress in tungsten. However, the slightly increasing of residual stresses in EUROFER limits the maximum thickness of FG-layer to 4 mm. Considering the operation phase, equivalent creep strain has been analyzed to assess the minimum thicknesses. It is clear that the thicker the better of FG-layer for reduction of the maximum creep strain, while a 0.7 mm thick FG-layer produces a sharp fall of equivalent creep strain. The maximum creep strain is negligibly small and independent on number of cycles when the thickness is greater than or equal to 1.2 mm. FE simulation results show that the most optimizing thickness of FG-layer is among 1.2 - 4 mm.

Based on the above results and the former spraying experiences, 0.7 mm is proposed as the FG layer thickness in the first VPS batch since with respect to the adhesion between vacuum plasma sprayed layers and the substrate the thinner the better. The total thickness of the coating system including the FG-layer and the W coating is 1.2 mm. In addition, coating systems with 0.3 and 0.5 mm thick FG-layer, respectively, are chosen to be fabricated for comparison. Therefore, five samples with designed three FG-layer thicknesses and two stepwise linear gradients have been fabricated by VPS. Produced FG W/EUROFER coating systems have a proper nominal microstructure with the pancake-like structure, columnar grains as well as low porosity and sound seamless substrate interfaces. Nano- and micro-hardness measurements show a fine linear gradient and global homogeneity.

The interface toughnesses of 225 and 258 J/m² have been evaluated for sample 5-T(7) and 3-T(7), respectively by performing three- and four-point bending test at 550 °C. Since the calculated methods used in the work does not consider the vast plastic defor-

mation which are observed during the crack propagating along the interface. The real interface toughness should be even higher.

For assessing the coating system as FW application, ELMs-like thermal shock and thermal fatigue tests have been performed in JUDITH1 and in a vacuum furnace, respectively. The thermal shock crack thresholds at RT and 550 °C for five coating systems lie between 0.19 and 0.38 GW/m², which is comparable with bulk pure W and W-UHP in Ref. [42]. Good thermal shock resistance benefits from three reasons including low porosity, grain features and the reduction of residual stress in the coating system. Particularly when the FG-layer thickness is greater than or equal to 0.7 mm, the higher thermal shock resistance is observed on the loaded samples. The coating systems with different layer numbers show a comparable thermal shock resistance since only a slightly smoother gradient is observed for samples with five layers as FG-layer. In addition, no visible macro- neither micro-crack has been observed after 500 cycles thermal fatigue tests, for both samples with the FG-layer thickness 0.3 and 0.7 mm, respectively. FG W/EUROFER coating system shows a promising thermal fatigue resistance.

5.2. Outlook

Owing to the promising properties of FG W/EUROFER coating system fabricated by VPS, in particular the high interfacial strength, the coating system with total thickness equal to 2 mm will be fabricated and investigated as FW application in the future. The FG-layer thickness will be specified to be 1.2 mm.

In addition, based on systematical investigation, an optimization of spraying parameters for improving coating quality, particularly for reducing the thermal influence on the substrate from spraying process, still need be developed by introducing a coolant channel, adjusting spraying parameters or reducing the preheated temperature of the substrate. The preheating temperature should be in the range between ≈ 600 °C to 760 °C (< 760 °C) considering the transition temperature of pancake-like coating structure, experiences and tempering temperature of substrate.

It will be very interesting to perform FE simulation to evaluate interface toughness and phase angle of load mixed level as well as to optimize the calculation method of interface toughness by considering plasticity at the interface.

6 Reference

1. H. Imura, *Japanese policy on the science and technology research*. Journal of Nuclear Materials, 2004. 329-333: p. 1-4.
2. www.iter.org.
3. H. Bruhns, *Fusion at the crossroads towards ITER*. Czechoslovak Journal of Physics, 2006. 56: p. B36-B53.
4. Y. T. Song, D. A. Yao, S. Wu, and P. Weng, *Structural analysis and manufacture for the vacuum vessel of experimental advanced superconducting tokamak (EAST) device*. Fusion Engineering and Design, 2006. 81(8-14): p. 1117-1122.
5. L. A. El-Guebaly, *Fifty Years of Magnetic Fusion Research (1958-2008): Brief Historical Overview and Discussion of Future Trends*. Energies, 2010. 3(6): p. 1067-1086.
6. L. V. Boccaccini, *EU Designs and Efforts on ITER HCPB TBM*, "FZK-Nachrichten," 2004.
7. A. Kohyama, A. Hishinuma, D. S. Gelles, R. L. Klueh, W. Dietz, and K. Ehrlich, *Low-activation ferritic and martensitic steels for fusion application*. Journal of Nuclear Materials, 1996. 233-237: p. 138-147.
8. K. Ehrlich, *The development of structural materials for fusion reactors*. Philosophical Transactions of the Royal Society A: Mathematical, Physical and Engineering Sciences, 1999. 357(1752): p. 595-623.
9. H. Bolt, V. Barabash, G. Federici, J. Linke, A. Loarte, J. Roth, and K. Sato, *Plasma facing and high heat flux materials - needs for ITER and beyond*. Journal of Nuclear Materials, 2002. 307: p. 43-52.
10. W. W. Basuki and J. Aktaa, *Diffusion bonding between W and EUROFER97 using V interlayer*. Journal of Nuclear Materials, 2012. 429(1-3): p. 335-340.
11. Z. H. Zhong, T. Hinoki, T. Nozawa, Y. H. Park, and A. Kohyama, *Microstructure and mechanical properties of diffusion bonded joints between tungsten and F82H steel using a titanium interlayer*. Journal of Alloys and Compounds, 2010. 489(2): p. 545-551.
12. Y. I. Jung, J. Y. Park, B. K. Choi, D. W. Lee, and S. Cho, *Interfacial microstructures of HIP joined W and ferritic-martensitic steel with Ti interlayers*. Fusion Engineering and Design, 2013. 88(9-10): p. 2457-2460.
13. W. S. Liu, Q. S. Cai, Y. Z. Ma, Y. Y. Wang, H. Y. Liu, and D. X. Li, *Microstructure and mechanical properties of diffusion bonded W/steel joint using V/Ni composite interlayer*. Materials Characterization, 2013. 86: p. 212-220.
14. W. W. Basuki and J. Aktaa, *Investigation of tungsten/EUROFER97 diffusion bonding using Nb interlayer*. Fusion Engineering and Design, 2011. 86(9-11): p. 2585-2588.
15. J. Y. Park, Y. I. Jung, B. K. Choi, D. W. Lee, and S. Cho, *Joining of tungsten to ferritic/martensitic steels by hot isostatic pressing*. Journal of Nuclear Materials, 2013. 442(1-3): p. S541-S545.
16. T. Weber, M. Stüber, S. Ulrich, R. Vaßen, W. W. Basuki, J. Lohmiller, W. Sittel, and J. Aktaa, *Functionally graded vacuum plasma sprayed and magnetron sputtered tungsten/EUROFER97 interlayers for joints in helium-cooled divertor components*. Journal of Nuclear Materials, 2013. 436(1-3): p. 29-39.
17. W. W. Basuki and J. Aktaa, *Investigation on the diffusion bonding of tungsten and EUROFER97*. Journal of Nuclear Materials, 2011. 417(1-3): p. 524-527.
18. S. Y. Moon, C. H. Choi, H. S. Kim, P. Oh, B. G. Hong, S. K. Kim, and D. W. Lee, *Thick tungsten coating on ferritic-martensitic steel applied with a vacuum plasma spray coating method*. Surface and Coatings Technology, 2015. 280: p. 225-231.

19. K. Tokunaga, T. Hotta, K. Araki, Y. Miyamoto, T. Fujiwara, M. Hasegawa, K. Nakamura, K. Ezato, S. Suzuki, M. Enoda, M. Akiba, T. Nagasaka, R. Kasada, and A. Kimura, *High heat loading properties of vacuum plasma spray tungsten coatings on reduced activation ferritic/martensitic steel*. Journal of Nuclear Materials, 2013. 438: p. S905-S908.
20. G. Thomas, *Advanced materials for plasma facing components in fusion devices*. 2009.
21. B. van der Schaaf, D. S. Gelles, S. Jitsukawa, A. Kimura, R. L. Klueh, A. Moslang, and G. R. Odette, *Progress and critical issues of reduced activation ferritic/martensitic steel development*. Journal of Nuclear Materials, 2000. 283: p. 52-59.
22. F. W. Wiffen and R. T. Santoro, *CONTROL OF ACTIVATION LEVELS TO SIMPLIFY WASTE MANAGEMENT OF FUSION REACTOR FERRITIC STEEL COMPONENTS*. The Minerals, Metals & Materials Society (TMS), 1983.
23. A. A. F. Tavassoli, A. Alamo, L. Bedel, L. Forest, J. M. Gentzbittel, J. W. Rensman, E. Diegele, R. Lindau, M. Schirra, R. Schmitt, H. C. Schneider, C. Petersen, A. M. Lancha, P. Fernandez, G. Filacchioni, M. F. Maday, K. Mergia, N. Boukos, Baluc, P. Spatig, E. Alves, and E. Lucon, *Materials design data for reduced activation martensitic steel type EUROFER*. Journal of Nuclear Materials, 2004. 329: p. 257-262.
24. P. Fernandez, A. M. Lancha, J. Lapena, and M. Hernandez-Mayoral, *Metallurgical characterization of the reduced activation ferritic/martensitic steel Eurofer'97 on as-received condition*. Fusion Engineering and Design, 2001. 58-59: p. 787-792.
25. P. Fernandez, A. M. Lancha, J. Lapena, M. Serrano, and M. Hernandez-Mayoral, *Metallurgical properties of reduced activation martensitic steel Eurofer'97 in the as-received condition and after thermal ageing*. Journal of Nuclear Materials, 2002. 307: p. 495-499.
26. R. Schaublin, D. Gelles, and M. Victoria, *Microstructure of irradiated ferritic/martensitic steels in relation to mechanical properties*. Journal of Nuclear Materials, 2002. 307: p. 197-202.
27. B. van der Schaaf, F. Tavassoli, C. Fazio, E. Rigal, E. Diegele, R. Lindau, and G. LeMarois, *The development of EUROFER reduced activation steel*. Fusion Engineering and Design, 2003. 69(1-4): p. 197-203.
28. R. Lindau, A. Moslang, M. Rieth, M. Klimiankou, E. Materna-Morris, A. Alamo, A. A. F. Tavassoli, C. Cayron, A. M. Lancha, P. Fernandez, N. Baluc, R. Schaublin, E. Diegele, G. Filacchioni, J. W. Rensman, B. van der Schaaf, E. Lucon, and W. Dietz, *Present development status of EUROFER and ODS-EUROFER for application in blanket concepts*. Fusion Engineering and Design, 2005. 75-79: p. 989-996.
29. M. S. M. Rieth, A. Falkenstein, P. Graf, S. Heger, H. Kempe, R. Lindau, H. Zimmermann, *EUROFER 97, Tensile, Charpy, Creep and Structural Tests*. FZKA-6911, 2003.
30. J. Rensman, E. Lucon, J. Boskeljon, J. van Hoepen, R. den Boef, and P. ten Pierick, *Irradiation resistance of Eurofer97 at 300 °C up to 10 dpa*. Journal of Nuclear Materials, 2004. 329-333: p. 1113-1116.
31. E. Gaganidze and J. Aktaa, *Assessment of neutron irradiation effects on RAFM steels*. Fusion Engineering and Design, 2013. 88(3): p. 118-128.
32. M. Kolluri, P. D. Edmondson, N. V. Luzginova, and F. A. v. d. Berg, *Influence of irradiation temperature on microstructure of EU batch of ODS Eurofer97 steel irradiated with neutrons*. Materials Science and Technology, 2014. 30(13): p. 1697-1702.
33. M. Kolluri, P. D. Edmondson, N. V. Luzginova, and F. A. v. d. Berg, *A structure–property correlation study of neutron irradiation induced damage in EU batch of ODS Eurofer97 steel*. Materials Science and Engineering: A, 2014. 597: p. 111-116.
34. E. Materna-Morris, R. Lindau, H.-C. Schneider, and A. Möslang, *Tensile behavior of EUROFER ODS steel after neutron irradiation up to 16.3dpa between 250 and 450°C*. Fusion Engineering and Design, 2015. 98-99: p. 2038-2041.

-
35. L. V. Boccaccini, L. Giancarli, G. Janeschitz, S. Hermsmeyer, Y. Poitevin, A. Cardella, and E. Diegele, *Materials and design of the European DEMO blankets*. Journal of Nuclear Materials, 2004. 329: p. 148-155.
36. A. Aiello, I. Ricapito, G. Benamati, and R. Valentini, *Hydrogen isotopes permeability in Eurofer 97 martensitic steel*. Fusion Science and Technology, 2002. 41(3): p. 872-876.
37. M. Rieth, J. L. Boutard, S. L. Dudarev, T. Ahlgren, S. Antusch, N. Baluc, M. F. Barthe, C. S. Becquart, L. Ciupinski, J. B. Correia, C. Domain, J. Fikar, E. Fortuna, C. C. Fu, E. Gaganidze, T. L. Galan, C. Garcia-Rosales, B. Gludovatz, H. Greuner, K. Heinola, N. Holstein, N. Juslin, F. Koch, W. Krauss, K. J. Kurzydowski, J. Linke, C. Linsmeier, N. Luzginova, H. Maier, M. S. Martinez, J. M. Missiaen, M. Muhammed, A. Munoz, M. Muzyk, K. Nordlund, D. Nguyen-Manh, P. Norajitra, J. Opschoor, G. Pintsuk, R. Pippan, G. Ritz, L. Romaner, D. Rupp, R. Schaublin, J. Schlosser, I. Uytendhouwen, J. G. van der Laan, L. Veleva, L. Ventelon, S. Wahlberg, F. Willaime, S. Wurster, and M. A. Yar, *Review on the EFDA programme on tungsten materials technology and science*. Journal of Nuclear Materials, 2011. 417(1-3): p. 463-467.
38. M. Rieth, S. L. Dudarev, S. M. G. de Vicente, J. Aktaa, T. Ahlgren, S. Autusch, D. E. J. Armstrong, M. Balden, N. Baluc, M. F. Barthe, W. W. Basuki, M. Battabyal, C. S. Becquart, D. Blagoeva, H. Boldyryeva, J. Brinkmann, M. Celino, L. Ciupinski, J. B. Correia, A. De Backer, C. Domain, E. Gaganidze, C. Garcia-Rosales, J. Gibson, M. R. Gilbert, S. Giusepponi, B. Gludovatz, H. Greuner, K. Heinola, T. Hoschen, A. Hoffmann, N. Holstein, F. Koch, W. Krauss, H. Li, S. Lindig, J. Linke, C. Linsmeier, P. Lopez-Ruiz, H. Maier, J. Matejicek, T. P. Mishra, M. Muhammed, A. Munoz, M. Muzyk, K. Nordlund, D. Nguyen-Manh, J. Opschoor, N. Ordas, T. Palacios, G. Pintsuk, R. Pippan, J. Reiser, J. Riesch, S. G. Roberts, L. Romaner, M. Rosinski, M. Sanchez, W. Schulmeyer, H. Traxler, A. Urena, J. G. van der Laan, L. Veleva, S. Wahlberg, M. Walter, T. Weber, T. Weitkamp, S. Wurster, M. A. Yar, J. H. You, and A. Zivelonghi, *Recent progress in research on tungsten materials for nuclear fusion applications in Europe*. Journal of Nuclear Materials, 2013. 432(1-3): p. 482-500.
39. K. Wittlich, T. Hirai, J. Compan, N. Klimov, J. Linke, A. Loarte, M. Merola, G. Pintsuk, V. Podkovyrov, L. Singheiser, and A. Zhitlukhin, *Damage structure in divertor armor materials exposed to multiple ITER relevant ELM loads*. Fusion Engineering and Design, 2009. 84(7-11): p. 1982-1986.
40. M. Wirtz, G. Cempura, J. Linke, G. Pintsuk, and I. Uytendhouwen, *Thermal shock response of deformed and recrystallised tungsten*. Fusion Engineering and Design, 2013. 88(9-10): p. 1768-1772.
41. T. Loewenhoff, A. Buerger, J. Linke, G. Pintsuk, A. Schmidt, L. Singheiser, and C. Thomser, *Evolution of tungsten degradation under combined high cycle edge-localized mode and steady-state heat loads*. Physica Scripta, 2011. T145.
42. J. Linke, T. Loewenhoff, V. Massaut, G. Pintsuk, G. Ritz, M. Roedig, A. Schmidt, C. Thomser, I. Uytendhouwen, V. Vasechko, and M. Wirtz, *Performance of different tungsten grades under transient thermal loads*. Nuclear Fusion, 2011. 51(7).
43. J. Matejicek, Y. Koza, and V. Weinzettl, *Plasma sprayed tungsten-based coatings and their performance under fusion relevant conditions*. Fusion Engineering and Design, 2005. 75-79: p. 395-399.
44. F. L. Chong, J. L. Chen, and J. G. Li, *Evaluation of tungsten coatings on CuCrZr and W/Cu FGM under high heat flux and HT-7 limiter plasma irradiation*. Journal of Nuclear Materials, 2007. 363: p. 1201-1205.
45. Y. Y. Lian, X. Liu, Z. K. Cheng, J. Wang, J. P. Song, Y. Yu, and J. M. Chen, *Thermal shock performance of CVD tungsten coating at elevated temperatures*. Journal of Nuclear Materials, 2014. 455(1-3): p. 371-375.
46. Y. Yahiro, M. Mitsuhara, K. Tokunakga, N. Yoshida, T. Hirai, K. Ezato, S. Suzuki, M. Akiba, and H. Nakashima, *Characterization of thick plasma spray tungsten coating on ferritic/martensitic steel F82H for high heat flux armor*. Journal of Nuclear Materials, 2009. 386-88: p. 784-788.

47. H. Greuner, H. Bolt, B. Boswirth, S. Lindig, W. Kuhnlein, T. Huber, K. Sato, and S. Suzuki, *Vacuum plasma-sprayed tungsten on EUROFER and 316L: Results of characterisation and thermal loading tests*. Fusion Engineering and Design, 2005. 75-79: p. 333-338.
48. M. Koizumi, *FGM activities in Japan*. Composites Part B, 1997. 28B: p. 1-4.
49. S. Uemura, *The activities of FGM on new application*, in *Functionally Graded Materials VII*, W. Pan, J. Gong, L. Zhang, and L. Chen, Editors. 2003. p. 1-9.
50. M. M. Gasik, *Micromechanical modelling of functionally graded materials*. Computational Materials Science, 1998. 13(1-3): p. 42-55.
51. S. Ueda and M. Gasik, *Thermal-elasto-plastic analysis of W-Cu functionally graded materials subjected to a uniform heat flow by micromechanical model*. Journal of Thermal Stresses, 2000. 23(4): p. 395-409.
52. T. Weber and J. Aktaa, *Numerical assessment of functionally graded tungsten/steel joints for divertor applications*. Fusion Engineering and Design, 2011. 86(2-3): p. 220-226.
53. P. Norajitra, A. Gervash, R. Giniyatulin, T. Ihli, W. Krauss, R. Kruessmann, V. Kumetsov, A. Makhankov, I. Mazul, and I. Ovchinnikov, *He-cooled divertor for DEMO: Experimental verification of the conceptual modular design*. Fusion Engineering and Design, 2006. 81(1-7): p. 341-346.
54. T. Weber, *Entwicklung und Optimierung von gradierten Wolfram/EUROFER97-Verbindungen für Divertorkomponenten*. 2012.
55. Y. Itoh, M. Takahashi, and H. Takano, *Design of tungsten/copper graded composite for high heat flux components*. Fusion Engineering and Design, 1996. 31(4): p. 279-289.
56. Z.-J. Zhou, S.-X. Song, J. Du, Z.-H. Zhong, and C.-C. Ge, *Performance of W/Cu FGM based plasma facing components under high heat load test*. Journal of Nuclear Materials, 2007. 363: p. 1309-1314.
57. R. Jedamzik, A. Neubrand, and J. Rodel, *Functionally graded materials by electrochemical processing and infiltration: application to tungsten/copper composites*. Journal of Materials Science, 2000. 35(2): p. 477-486.
58. Z. J. Zhou and Y. S. Kwon, *Fabrication of W-Cu composite by resistance sintering under ultra-high pressure*. Journal of Materials Processing Technology, 2005. 168(1): p. 107-111.
59. Z. J. Zhou, J. Du, S. X. Song, Z. H. Zhong, and C. C. Ge, *Microstructural characterization of W/Cu functionally graded materials produced by a one-step resistance sintering method*. Journal of Alloys and Compounds, 2007. 428(1-2): p. 146-150.
60. Y. H. Ling, J. T. Li, Z. J. Zhou, and C. C. Ge, *Fabrication and microstructure of W/Cu functionally graded material*. Journal of University of Science and Technology Beijing, 2001. 8(3): p. 198-202.
61. C. C. Ge, Z. J. Zhou, and Y. H. Ling, *New progress of metal-based functionally graded plasma-facing materials in China*, in *Functionally Graded Materials VII*, W. Pan, J. Gong, L. Zhang, and L. Chen, Editors. 2003. p. 11-16.
62. D. Qu, Z. Zhou, J. Tan, and J. Aktaa, *Characterization of W/Fe functionally graded materials manufactured by resistance sintering under ultra-high pressure*. Fusion Engineering and Design, 2015. 91: p. 21-24.
63. *Preparation of Fe-W amorphous films by an electroplating method*.
64. N. Tsyntsaru, J. Bobanova, X. Ye, H. Cesiulis, A. Dikumar, I. Prosycevas, and J. P. Celis, *Iron-tungsten alloys electrodeposited under direct current from citrate-ammonia plating baths*. Surface and Coatings Technology, 2009. 203(20-21): p. 3136-3141.
65. C. Wang, P. Brault, C. Zaepffel, J. Thiault, A. Pineau, and T. Sauvage, *Deposition and structure of W-Cu multilayer coatings by magnetron sputtering*. Journal of Physics D-Applied Physics, 2003. 36(21): p. 2709-2713.
66. G. Pintsuk, S. E. Brunings, J. E. Doring, J. Linke, I. Smid, and L. Xue, *Development of W/Cu - functionally graded materials*. Fusion Engineering and Design, 2003. 66-68: p. 237-240.

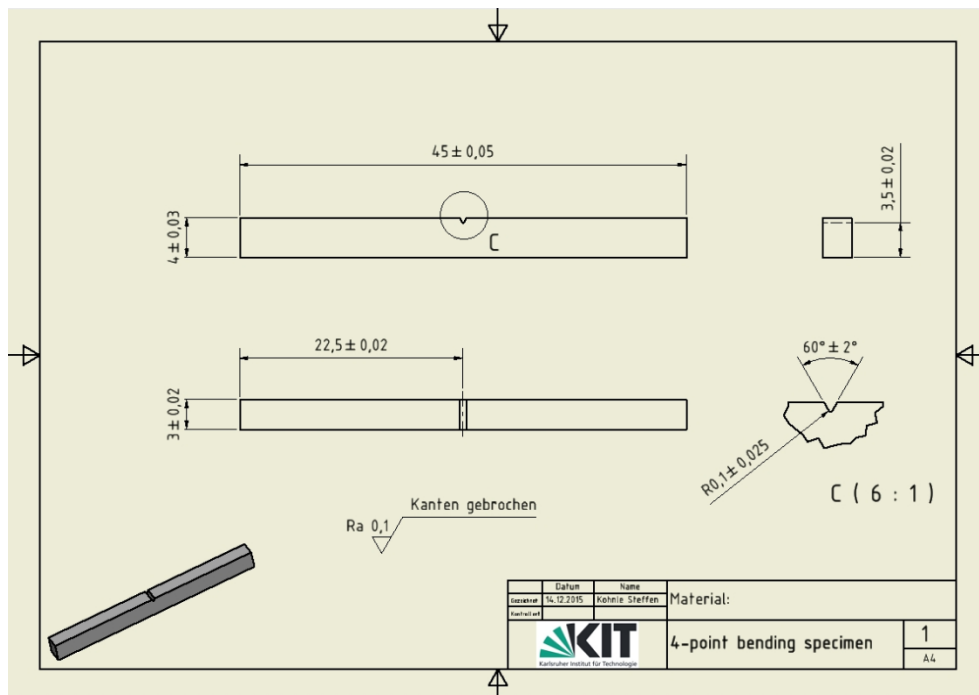
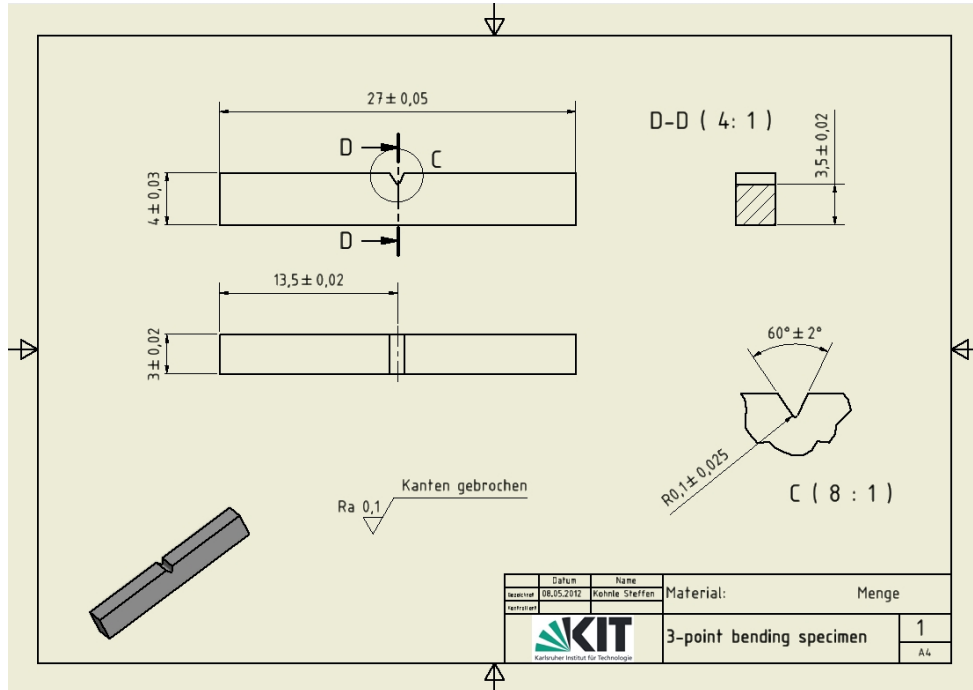
-
67. Z. J. Zhou, S. Q. Guo, S. X. Song, W. Z. Yao, and C. C. Ge, *The development and prospect of fabrication of W based plasma facing component by atmospheric plasma spraying*. Fusion Engineering and Design, 2011. 86(9-11): p. 1625-1629.
68. G. Pintsuk, I. Smid, J. E. Doring, W. Hohenauer, and J. Linke, *Fabrication and characterization of vacuum plasma sprayed W/Cu-composites for extreme thermal conditions*. Journal of Materials Science, 2007. 42(1): p. 30-39.
69. F. Hermanek, *Thermal spray terminology and company origins*. ASM International, 2001.
70. P. L. Fauchais, J. V.R. Heberlein, and M. I. Boulos, *Thermal spray fundamentals: From Powder to Part*. 2014: Springer.
71. R. G. Castro, A. H. Bartlett, K. J. Hollis, and R. D. Fields, *The effect of substrate temperature on the thermal diffusivity and bonding characteristics of plasma sprayed beryllium*. Fusion Engineering and Design, 1997. 37: p. 243-252.
72. P. Fauchais, G. Montavon, and G. Bertrand, *From Powders to Thermally Sprayed Coatings*. Journal of Thermal Spray Technology, 2010. 19(1-2): p. 56-80.
73. P. Fauchais, *Understanding plasma spraying*. Journal of Physics D: Applied Physics, 2004. 37(9): p. R86-R108.
74. P. Fauchais, M. Fukumoto, A. Vardelle, and M. Vardelle, *Knowledge concerning splat formation: An invited review*. Journal of Thermal Spray Technology, 2004. 13(3): p. 337-360.
75. L. Pawlowski, *The Science and Engineering of Thermal Spray Coatings*, 2008: Wiley, Chichester, UK
76. M. Pasandideh-Fard, V. Pershin, S. Chandra, and J. Mostaghimi, *Splat shapes in a thermal spray coating process: Simulations and experiments*. Journal of Thermal Spray Technology, 2002. 11(2): p. 206-217.
77. M. Fukumoto and Y. Huang, *Flattening Mechanism in Thermal Sprayed Nickel Particle Impinging on Flat Substrate Surface*. Journal of Thermal Spray Technology 1999. 8(3): p. 427-432.
78. T. Tokunaga, H. Watanabe, N. Yoshida, T. Nagasaka, R. Kasada, Y.-J. Lee, A. Kimura, M. Tokitani, M. Mitsuhashi, T. Hinoki, H. Nakashima, S. Masuzaki, T. Takabatake, N. Kuroki, K. Ezato, S. Suzuki, and M. Akiba, *Development of high-grade VPS-tungsten coatings on F82H reduced activation steel*. Journal of Nuclear Materials, 2013. 442(1-3): p. S287-S291.
79. O. Kovarik, P. Hausild, J. Siegl, T. Chraska, J. Matejcek, Z. Pala, and M. Boulos, *The influence of substrate temperature on properties of APS and VPS W coatings*. Surface & Coatings Technology, 2015. 268: p. 7-14.
80. A. Zivelonghi, F. Cernuschi, C. Peyrega, D. Jeulin, S. Lindig, and J. H. You, *Influence of the dual-scale random morphology on the heat conduction of plasma-sprayed tungsten via image-based FEM*. Computational Materials Science, 2013. 68: p. 5-17.
81. P. Fernandez, A. M. Lancha, J. Lapena, R. Lindau, M. Rieth, and M. Schirra, *Creep strength of reduced activation ferritic/martensitic steel Eurofer'97*. Fusion Engineering and Design, 2005. 75-79: p. 1003-1008.
82. S. M. Thurgate, *Auger Spectroscopy and Surface Analysis*. 1997.
83. www.knmf.kit.edu/AES.php.
84. F. J. HUMPHREYS, *Review: Grain and subgrain characterisation by electron backscatter diffraction*. JOURNAL OF MATERIALS SCIENCE, 2001. 36: p. 3833-3854.
85. G. M. Pharr, W. C. Oliver, and F. R. Brotzen, *ON THE GENERALITY OF THE RELATIONSHIP AMONG CONTACT STIFFNESS, CONTACT AREA, AND ELASTIC-MODULUS DURING INDENTATION*. Journal of Materials Research, 1992. 7(3): p. 613-617.
86. W. C. Oliver and G. M. Pharr, *Measurement of hardness and elastic modulus by instrumented indentation: Advances in understanding and refinements to methodology*. J. Mater. Res., 2004. 19: p. 3-20.

87. W. C. Oliver and G. M. Pharr, *An improved technique for determining hardness and elastic modulus using load and displacement sensing indentation experiments*. Journal of Materials Research, 1992. 7: p. 1564-1583.
88. O. M. Wirtz, *Thermal Shock Behaviour of Different Tungsten Grades under Varying Conditions*, 2013, Grafische Medien, Forschungszentrum Jülich GmbH.
89. J. Aktaa, S. Kecskes, and F. Cismondi, *Non-linear failure analysis of HCPB Test Blanket Module*. Fusion Engineering and Design, 2012. 87(7-8): p. 1085-1090.
90. G. R. Irwin. *Onset of Fast Crack Propagation in High Strength Steel and Aluminum Alloys*. in *Sagamore Research Conference Proceedings*. 1956.
91. J. R. Rice, *A Path Independent Integral and the Approximate Analysis of Strain Concentration by Notches and Cracks*. Journal of Applied Mechanics, 1968. 35: p. 379-386.
92. *ASTM E1820-13 Standard Test Method for Measurement of Fracture Toughness*.
93. P. G. Charalambides, J. Lund, A. G. Evans, and R. M. McMeeking, *A test specimen for determining the fracture resistarim of bimaterial interfaces*. Journal of Applied Mechanics-Transactions of the Asme, 1989. 56(1): p. 77-82.
94. A. J. Phillipps, W. J. Clegg, and T. W. Clyne, *FRACTURE-BEHAVIOR OF CERAMIC LAMINATES IN BENDING .1. MODELING OF CRACK-PROPAGATION*. Acta Metallurgica Et Materialia, 1993. 41(3): p. 805-817.
95. A. J. Phillipps, W. J. Clegg, and T. W. Clyne, *FRACTURE-BEHAVIOR OF CERAMIC LAMINATES IN BENDING .2. COMPARISON OF MODEL PREDICTIONS WITH EXPERIMENTAL-DATA*. Acta Metallurgica Et Materialia, 1993. 41(3): p. 819-827.
96. L. H. Zou, Y. Huang, R. F. Chen, C. A. Wang, and D. S. Park, *The measurement and characterization of the interfacial toughness of Si₃N₄/BN composites by a three-point bending test*. Journal of the European Ceramic Society, 2003. 23(11): p. 1987-1996.
97. F. Tavassoli, *Fusion Demo Interim Structural Design Criteria (DISDC)/Appendix A: Material Design Limit Data/A3.S18E Eurofer Steel*. DMN Technical Report, 2004. DMN/DIR/NT/2004-000/A (2004).
98. J. Aktaa, M. Weick, and M. Walter, *High Temperature creep-Fatigue structural Design Criteria for Fusion components Built from EUROFER97 FZKA 7309*, 2007.
99. D. D. Qu, W. W. Basuki, and J. Aktaa, *Numerical assessment of functionally graded tungsten/EUROFER coating system for first wall applications*. Fusion Engineering and Design, 2015. 98-99: p. 1389-1393.
100. T. Weber, M. Stueber, S. Ulrich, R. Vassen, W. W. Basuki, J. Lohmiller, W. Sittel, and J. Aktaa, *Functionally graded vacuum plasma sprayed and magnetron sputtered tungsten/EUROFER97 interlayers for joints in helium-cooled divertor components*. Journal of Nuclear Materials, 2013. 436(1-3): p. 29-39.
101. A. Kobayashi, S. Sharafat, and N. M. Ghoniem, *Formation of tungsten coatings by gas tunnel type plasma spraying*. Surface and Coatings Technology, 2006. 200(14-15): p. 4630-4635.
102. J. E. Doring, R. Vassen, G. Pintsuk, and D. Stover, *The processing of vacuum plasma-sprayed tungsten-copper composite coatings for high heat flux components*. Fusion Engineering and Design, 2003. 66-68: p. 259-263.
103. T. Nagasaka, R. Kasada, A. Kimura, Y. Ueda, and T. Muroga, *THERMOPHYSICAL PROPERTIES AND MICROSTRUCTURE OF PLASMA-SPRAYED TUNGSTEN COATING ON LOW ACTIVATION MATERIALS*. Fusion Science and Technology, 2009. 56(2): p. 1053-1057.
104. J. KOVACIK, *Correlation between Young's modulus and porosity in porous materials*. JOURNAL OF MATERIALS SCIENCE LETTERS 1999. 18: p. 1007 – 1010.
105. J. A. Choren, S. M. Heinrich, and M. B. Silver-Thorn, *Young's modulus and volume porosity relationships for additive manufacturing applications*. Journal of Materials Science, 2013. 48(15): p. 5103-5112.

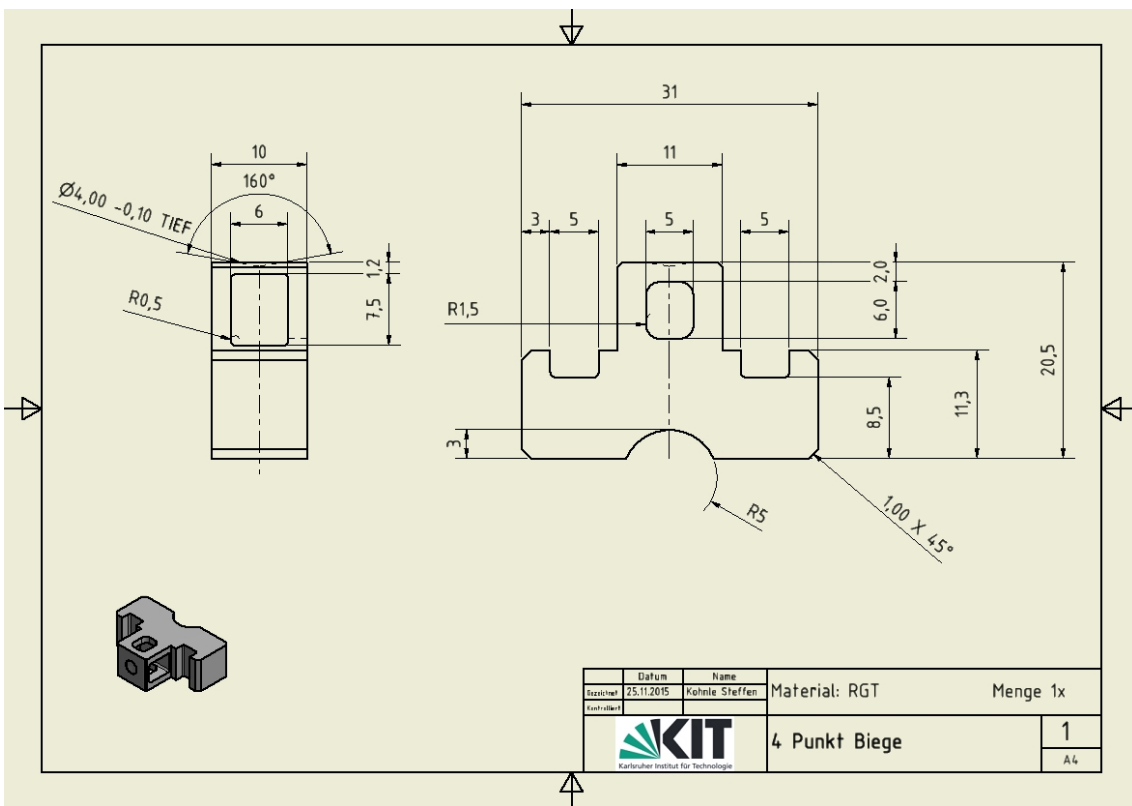
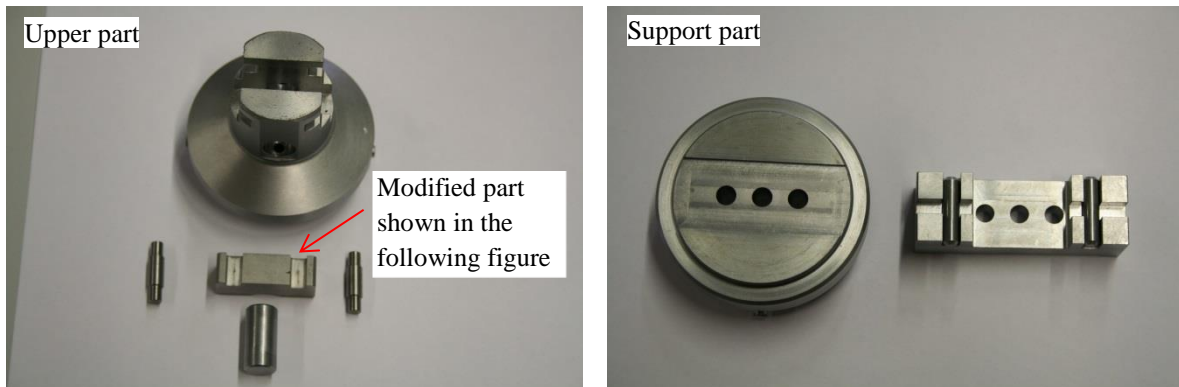
-
106. S. Noh, R. Kasada, A. Kimura, T. Nagasaka, M. A. Sokolov, and T. K. Kim, *Interfacial microstructures and hardness distributions of vacuum plasma spraying W-coated ODS ferritic steels for fusion plasma facing applications*. Fusion Engineering and Design, 2014. 89(4): p. 289-293.
107. P. G. Charalambides and A. G. Evans, *DEBONDING PROPERTIES OF RESIDUALLY STRESSED BRITTLE-MATRIX COMPOSITES*. Journal of the American Ceramic Society, 1989. 72(5): p. 746-753.
108. K. Bose, P. A. Mataga, and P. P. Castaneda, *Stable crack growth along a brittle:ductile interface-II. Small scale yielding solutions and interfacial toughness predictions*. International Journal of Solids and Structures, 1999. 36: p. 1-34.
109. S. Aoki and N. Ishii, *An interface crack under mixed-mode loading*. Modelling Simul. Mater. Sci Eng. , 1994. 2: p. 473-482.
110. S. J. HOWARD, Y. C. TSUI , and T. W. CLYNE, *THE EFFECT OF RESIDUAL STRESSES ON THE DEBONDING OF COATINGS--I. A MODEL FOR DELAMINATION AT A BIMATERIAL INTERFACE*. 1994.
111. Y. C. TSUI, S. J. HOWARD, and T. W. CLYNE, *THE EFFECT OF RESIDUAL STRESSES ON THE DEBONDING OF COATINGS-- II. AN EXPERIMENTAL STUDY OF A THERMALLY SPRAYED SYSTEM*. 1994.
112. J. Du, Y. Yuan, M. Wirtz, J. Linke, W. Liu, and H. Greuner, *FEM study of recrystallized tungsten under ELM-like heat loads*. Journal of Nuclear Materials, 2015. 463: p. 219-222.
113. M. Wirtz and J. Linke, *Thermal shock tests and observation of exposed surface microstructure, Private communication*. 2015.
114. Y. Yuan, J. Du, M. Wirtz, G. N. Luo, G. H. Lu, and W. Liu, *Surface damage and structure evolution of recrystallized tungsten exposed to ELM-like transient loads*. Nuclear Fusion, 2016. 56(3): p. 036021.
115. T. Hirai, N. Bekris, J. P. Coad, C. Grisolia, J. Linke, H. Maier, G. F. Matthews, V. Philipps, and E. Wessel, *Failure modes of vacuum plasma spray tungsten coating created on carbon fibre composites under thermal loads*. Journal of Nuclear Materials, 2009. 392(1): p. 40-44.
116. A. S. Arakcheev, A. Huber, M. Wirtz, G. Sergienko, I. Steudel, A. V. Burdakov, J. W. Coenen, A. Kreter, J. Linke, P. Mertens, A. A. Shoshin, B. Unterberg, and A. A. Vasilyev, *Theoretical investigation of crack formation in tungsten after heat loads*. Journal of Nuclear Materials, 2015. 463: p. 246-249.
117. I. Smid, M. Akiba, G. Vieider, and L. Plochl, *Development of tungsten armor and bonding to copper for plasma-interactive components*. Journal of Nuclear Materials, 1998. 258: p. 160-172.
118. L. Xu, Wu Xiaochun, Shao Guangjie, Min Yongan, *Effect of the tempering temperature on thermal fatigue behavior of 4Cr5MoSiV1 and 8407 steels*. Materials engineering (in Chinese), 2001. 2: p. 3-7.
119. D. Mellouli, N. Haddar, A. Koster, and H. F. Ayedi, *Hardness effect on thermal fatigue damage of hot-working tool steel*. Engineering Failure Analysis, 2014. 45: p. 85-95.
120. F. Tang and J. M. Schoenung, *Evolution of Young's modulus of air plasma sprayed yttria-stabilized zirconia in thermally cycled thermal barrier coatings*. Scripta Materialia, 2006. 54(9): p. 1587-1592.

Appendix

A. Specimen dimensions of three- and four-point bending tests



B. Set-up of four-point bending



C. Interface toughness calculated based on three-point bending

For $0 < x < L - x$

$$\frac{d^2y_1}{dx^2} = -\frac{Px}{2E_c} \quad (C1)$$

For $L - x < x < L$

$$\frac{d^2y_2}{dx^2} = -\frac{Px}{2E_{sub}} \quad (C2)$$

After the first integration,

$$\frac{dy_1}{dx} = -\frac{Px^2}{4E_c} + A_1 \quad (C1.1)$$

$$\frac{dy_2}{dx} = -\frac{Px^2}{4E_{sub}} + B_1 \quad (C2.1)$$

After the second integration,

$$y_1 = -\frac{Px^3}{12E_c} + A_1x + A_2 \quad (C1.2)$$

$$y_2 = -\frac{Px^3}{12E_{sub}} + B_1x + B_2 \quad (C2.2)$$

where A_1 , A_2 , B_1 and B_2 are constant value.

The boundary conditions:

$$y_1|_{x=0} = 0 \quad (C3)$$

$$\frac{dy_1}{dx}|_{x=(L-a)} = \frac{dy_2}{dx}|_{x=(L-a)} \quad (C4)$$

$$y_1|_{x=(L-a)} = y_2|_{x=(L-a)} \quad (C5)$$

$$\frac{dy_2}{dx}|_{x=L} = 0 \quad (C6)$$

When substituting the boundary conditions, the constant value can be abtained:

$$A_2 = 0$$

$$A_1 = \frac{P(L-a)^2}{4E_c} - \frac{P(L-a)^2}{4E_{sub}} + \frac{PL^2}{4E_{sub}}$$

$$B_1 = \frac{PL^2}{4E_{sub}}$$

$$B_2 = \frac{P(L-a)^3}{6} \left(\frac{1}{E_c} - \frac{1}{E_{sub}} \right)$$

Then the deflection at the central point can be expressed:

$$y = \frac{PL^3}{6E_{sub}} + \frac{P(L-a)^3}{6} \left(\frac{1}{E_c} - \frac{1}{E_{sub}} \right) \quad (C7)$$

Acknowledgments

This work was conducted in Institute of Applied material – Materials and Biomechanics (IAM-WBM) at Karlsruhe Institute of Technology (KIT). I gratefully acknowledge the financial support from both China Scholarship Council (CSC) and KIT. I would like to express my appreciation to all the people who have provided contributions to this research, many of who are not mentioned here.

I appreciate great help and guidance from my supervisor Priv.-Doz. Dr. Jarir Aktaa. This work would never be possible without his support. He was always willing to discuss with me on difficulties of my research and provided me scientific guidance and support. I would like to thank Prof. Dr. Anton Möslang for reviewing my dissertation and providing valuable suggestions. I want to thank Prof. Dr. Robert Stieglitz for being the chair of the committee and his valuable discussion.

I would like to thank Dr. Widodo Widjaja Basuki and Dr. Ermile Gaganidze for their inspirable suggestions and fruitful discussions. Specifically Dr. Basuki standardized my experimental skill and improving my scientific thought at the first two years of my study, Dr. Gaganidze helps me a lot on the determination of the interface toughness. Many thanks to Dr. Dimitri Litvinov for coaching me in SEM and EBSD. I would like to thank Dr. Ruth Schwaiger for her kind guidance on nanoindentation. I want to thank Daniela Exner and Ewald Ernst for their helps on metallurgical microscope and sample preparation, respectively. Steffen Kohnle and Ralf Dahm offer me great help for operating vacuum furnace, cutting samples and machining molds, and solving all kinds of problems during my experiments.

I would specially appreciate Prof. Dr. Robert Vaßen from IEK-1, Forschungszentrum Jülich (FZ Jülich) for fabricating samples for me. I want to thank Dr. Jochen Linke and Dr. Marius Wirtz from IEK-2, FZ Jülich for performing thermal shock tests and fruitful discussions. I would like to thank Dr. Jens Gibmeier and Hyoung Chul Back from IAM-WK for providing residual stress measurement and significant discussions.

I would like to thank my colleagues for warm and inspiring working atmosphere, as well as their wonderful friendship. Many thanks to Luis Straßberger for his nice discussion during my research and daily help on software and drawing, as well as great sharing of his travelling and sports experiences. I would like to thank Michael Mahler for helping me install software ABAQUS, use the resonating test machine and translate the abstract of this thesis into German. I want to thank Ulrich Führer, Marco Conte and Ankur Chauhan for their nice discussion and insightful suggestions during my research.

Christian Dethloff offers me great help for improving the English writing of my thesis. Julian Bredl provides kind assistance on Vickers hardness measurement.

I want to thank my friends, Yiming Wang, Pei He and Kuo Zhang for their help and encouragements. I would like to thank my friends Xiangna Cong, Meng He, Di. Chen, Zhi Chen, Ping Gao, Wenqian Feng, Jie Ye and Zhaoping Luo for their warm friendship that made my stay in Karlsruhe pleasant.

Finally, I would like to appreciate my husband Shangzhou Zhang for his continuous love, understand, support and encouragement. He is always there to grow with me, he is my sunshine since always. I want to thank my sister Feifei Qu and my parents: Qinggang Qu and Haiju Hu, for their endless love and support in the last four years. I could not live in Germany alone without their love.

List of publications

Journal papers

[1] D.D. Qu, W.W. Basuki, J. Aktaa. Numerical Assessment of Functionally Graded Tungsten/Steel Coating System for First Wall Applications [J]. *Fusion Engineering and Design* 2015. 98-99: p. 1389-1393.

[3] D.D. Qu, W.W. Basuki, J. Gibmeier, R. Vaßen, J. Aktaa, DEVELOPMENT OF FUNCTIONALLY GRADED TUNGSTEN/EUROFER COATING SYSTEM FOR FIRST WALL APPLICATION, *Fusion Science and Technology*, 68 (2015): 578-581

[2] D.D. Qu, Z.J. Zhou, J. Tan, J. Aktaa. Characterization of W/Fe functionally graded materials manufactured by Resistance Sintering under Ultra-High Pressure [J], *Fusion Engineering and Design* 91 (2015) 21–24

[4] D.D. Qu, Z.J. Zhou, Y. Yum, J. Tan. Mechanical characterization and modelling of brazed tungsten and Cu-Cr-Zr alloy using stress relief interlayers [J], *Journal of Nuclear Materials*, 455 (2014): 130–133

Conference presentations

[1] D.D. Qu, W.W. Basuki, M. Wirtz, J. Linke, R. Vaßen and J. Aktaa, *Development and optimization of functionally graded tungsten/EUROFER coating for first wall application*, 17th ICFRM, 12-16.10.2015, Germany (poster)

[2] D.D. Qu, M. Wirtz, J. Linke, R. Vaßen and J. Aktaa *Functionally graded tungsten/EUROFER coating for first wall application*, 12th ISFNT, 14-18.09.2015, Korea (oral talk)

[3] D.D. Qu, M. Wirtz, J. Linke, R. Vaßen and J. Aktaa, *Functionally Graded Tungsten/EUROFER Coating System and Its Response to ELMs-like Thermal Shock Loading*, 5th PFMC, 18-22.05.2015, France (poster)

[4] D. D. QU, W.W. BASUKI, J. GIBMEIER, R. VABEN, J. AKTAA, *Mechanical and microstructural characterization of functionally graded tungsten/EUROFER coating systems*, 12th ICM, 10-14.05.2015, Germany (oral talk)

[5] D.D. Qu, W.W. Basuki, J. Aktaa, *Numerical Assessment of Functionally Graded Tungsten/EUROFER Coating System for First Wall Applications*, 28th SOFT, 28.09-03.10.2014, Spain (poster)

Curriculum Vitae

Personal information:

Name: Dandan Qu
Date of birth: 04.11.1986
Place of birth: Heilongjiang, China
Nationality: Chinese
Email: dandan.qu@kit.edu or xiaoqukaixin124@126.com

Education background:

10.2012 – 10.2016 Karlsruhe Institute of Technology (KIT)
Degree: Doctor Major: Material Science
09.2009 - 01.2012 University of Science and Technology Beijing
Degree: Master Major: Materials Science and Engineering
09.2005 - 06.2009 China University of Geosciences (Beijing)
Degree: Bachelor Major: Materials Science and Engineering